Time-resolved spectroscopic studies of lanthanides doped inorganic, hybrid and organic systems

Lu, Haizhou

Time-resolved spectroscopic studies of lanthanides doped inorganic, hybrid and organic systems

Haizhou Lu

Supervised by Prof. William P. Gillin & Dr. Ignacio Hernández

School of Physics and Astronomy

Queen Mary University of London

Submitted for the degree of Doctor of Philosophy

2015

Statement of originality

I, HAIZHOU LU, confirm that the research included within this thesis is my own work or that where it has been carried out in collaboration with, or supported by others, that this is duly acknowledged below and my contribution indicated. Previously published materials is also acknowledged below.

I attest that I have exercised reasonable are to ensure that the work is original, and does not to the best of my knowledge break any UK law, infringe any third party's copyright or other Intellectual Property Right, or contain any confidential material.

I accept that the college has the right to use plagiarism detection software to check the electronic version of the thesis.

I confirm that this thesis has not been previously submitted for the award of a degree by this or any other university.

Signature: HAIZHOU LU

Date: 21 July, 2015

Acknowledgements

Firstly, I would like to thank my primary supervisor, Prof. W. P. Gillin, who gave me excellent guidance for all the experiments and discussions during my PhD period. His rich experience and constructive ideas made my PhD run smoothly. This thesis would have been impossible to complete without his hard work. Of course, I also appreciate his careful reading of and comments on this thesis.

Secondly, I want to show my sincere gratitude to my co-supervisor, Dr. I. Hernández, with whom I had many useful discussions about experimental settings and data analysis. He helped me develop a good understanding of lanthanide systems. All the experiments could not have been done so quickly without his careful instructions and clever ideas.

Then, I would like to express my special thanks to Mr. G. Gannaway and Dr. K. Scott for showing me the lab rules and how to use the equipment during my first year. In addition, I would like to thank Mr. G. Nevill for supplying the glass substrates. All these people were necessary for my research.

Also, I would like to thank all my previous and current colleges including Dr. X. Cui, Dr. Z. Li, Dr. Y. Peng, Dr. H. Ye, Dr. H. Zhang, Dr. H. Gu and those who are going to be Doctors: M. Song, J. Hu and S. Chang. A special thank you is given to Dr. Y. Peng and Dr. X. Cui as my collaborators. All these people made my life in London easy and colourful.

In addition, I acknowledge the contribution of Dr. R. Wilson and Dr. Z. Luklinska for running XRD measurements and EDX measurements for my Er^{3+}-doped Y_2O_3 samples. Acknowledgements also go to Dr. X. Cui for training me in the production of $NaYF_4$ nanoparticles and taking TEM images. Special thanks to the Chinese Scholarship Council (CSC) and Queen Mary University of London (QMUL) for their financial support.

Finally, I would like to thank my parents, Mr. D. Lu and Mrs. P. Zhou, and my grandparents, Mr. Z. Lu and Mrs. Y. Huang for giving me continuous support for self-development.

List of publications

1: "Concentration dependent of the up- and down-conversion emission colours of Er^{3+}-doped Y_2O_3: a time-resolved spectroscopy analysis", **H. Lu**, W. P. Gillin and I. Herández, *Physical Chemistry Chemical Physics*, **16** (2014) 20957-20963.

2: "Annealing and doping-dependent magnetoresistance in single layer poly (3-hexyl-thiophene) organic semiconductor device", H. Gu, S. Chang, D. Holford, T. Zhang, **H. Lu**, T. Kreouzis and W. P. Gillin, *Organic Electronics*, **17** (2015) 51-56.

3: "Synthesis, characterization and applications of core-shell $Co_{0.16}Fe_{2.84}O_4$@$NaYF_4$(Yb, Er) and Fe_3O_4@$NaYF_4$(Yb, Tm) nanoparticles as tri-modal (MRI, PET/SPECT and Optical) imaging agents", X. Cui, D. Mathe, N. Kovács, I. Horvath, M. Jauregui-osoro, R. T. M. de Rosales, G. Edgar David Mullen, W. Song, Y. Yan, D. Krueger, A. N. Khlobystov, M. Gimenez-Lopez, M. Semjeni, K. Szigeti, D. Veres, **H. Lu**, I. Herández, W. P. Gillin, A. Protti, K. Petik, M. A. Green, P. J. Blower, *Bioconjugate Chemistry*, just accepted manuscript.

4: "Sensitisation, energy transfer processes and lifetime modulation in sub 10 nm Yb^{3+}-doped $NaYF_4$ nanoparticles with visible light through a perfluoroanthraquinone chromophore", **H. Lu**, Y. Peng, H. Ye, X. Cui, M. A. Green, P. J. Blower, P. B. Wyatt, W. P. Gillin and I. Herández, *submitted to Nanoscale*.

Abstract

In this thesis, three main chapters are discussed, including an Er^{3+}-doped Y_2O_3 system, a Yb^{3+}-doped $NaYF_4$ nanoparticle system and a $Yb(F\text{-}TPIP)_3$ co-evaporated with a $Zn(F\text{-}BTZ)_2$ organic system. The main discussion is about the underlying physics of lanthanides, sensitisation of lanthanide ions by using the time resolved spectroscopy method.

The up- and down-conversion processes between Er^{3+} ion pairs in the Y_2O_3 system was systematically investigated using the time resolved spectroscopy method regarding different Er^{3+} doping concentrations. The measured lifetime gives direct evidence for differentiating the excited state absorption (ESA) and energy transfer (ET) mechanisms during up-conversion processes. Also, the looping mechanism is found by measuring the NIR luminescence lifetime. Most importantly, the red to green emission ratio change during up-conversion processes with doping concentration is explained by a combination of up-conversion route change and concentration quenching effect.

A novel sensitisation of Yb^{3+}-doped $NaYF_4$ nanoparticles is demonstrated by capping a 1,2,3,4,5,6,7-heptafluoro-8-hydroxyanthracene-9,10-dione (HL) ligand to the nanoparticle surface. The HL ligand acts as an antenna which can absorb visible light (400 nm to 600 nm) and then transfers the excited energy to Yb^{3+} ions encapsulated in the $NaYF_4$ host. Interestingly, the energy transfers from the HL ligand to Yb^{3+} ions near the surface and then migrates to the Yb^{3+} ions inside the core of nanoparticles and is proved by a systematic time resolved spectroscopy study. The integrated organic chromophore based-excitation is almost 300 times higher compared with the Yb^{3+} intrinsic absorption band based-excitation.

The last main discussion is given to the sensitisation of Yb^{3+} ions in a co-evaporated organic system as the co-evaporated organic system is more optically desirable than either the Y_2O_3 or the nanoparticle system. Compared with the intrinsic sensitisation, two orders of magnitude times sensitisation of Yb^{3+} ions is demonstrated by co-evaporating $Yb(F\text{-}TPIP)_3$ and the $Zn(F\text{-}BTZ)_2$ chromophore, making it a suitable material for a waveguide amplifier.

In summary, an Er^{3+}-doped Y_2O_3 system is investigated as the fundamental study to understand the underlying physics, and then HL ligand and $Zn(F\text{-}BTZ)_2$ chromophore are investigated as potential sensitisers for Yb^{3+}-doped nanoparticles and organic systems separately. The study in this thesis should be useful not only for fundamental physics but also as a reference for the applications of lanthanides.

Contents

Chapter 1: Introduction

1.1. Background and organisation

With the development of modern techniques, there has been a great demand and development of luminescent materials and optoelectronic devices, in which the lanthanide elements have played a vitally important role. Due to their large Stokes shifts and long emission lifetimes, lanthanide ions have been widely used in products relevant to our daily life, including light emitting diodes (LED), televisions, computer displays, optical fibres, optical amplifiers, lasers and medical diagnosis, and cell imaging [1]. Especially, the use of lanthanides in the field of doped-fibre amplifiers and lasers. For example, Er^{3+}/Yb^{3+}-doped amplifiers are significant devices for telecommunication applications [2, 3], and Nd^{3+}-doped yttrium aluminium garnet (Nd: YAG) is a commonly used as a lasing medium for solid-state lasers [4].

Nowadays, lots of attention has been focused on several of the following potential applications [1]: (1) the continuing use in the lighting industry, (2) functional complexes for biological assays [5], medical imaging [6] and solar cell [7], (3) electroluminescent materials for organic light emitting diode [8] and optical fibre for telecommunications [2]. I have been motivated in understanding and developing materials in the field of the second and third main applications.

As described above, the main applications of lanthanides are all relevant to light emission, which is basically due to the electronic state transitions inside the $4f^n$

energy manifolds of lanthanide ions. The doping concentration effect of the up- and down-conversion processes of Er^{3+} ions has been a common interest. In order to be clear of the underlying physics, Er^{3+}-doped with the Y_2O_3 system is analysed as fundamental research using two important tools: time resolved spectroscopy and lifetime measurements. Further details are given in chapter 3.

Then, it was found that the energy transfer between lanthanide ions is not efficient even under the best doping conditions as the absorption cross section of lanthanide is small. Take the Er^{3+} ion for example, for the majority of the Er^{3+} doped inorganic and organic matrix, the absorption cross section is only 10^{-22} to 10^{-20} cm^2 for a given wavelength [9]. Therefore, it is expected that a new kind chromophore, which has a strong and broad absorption during visible light region can be used as an 'antenna' to harvest energy and transfer it to the lanthanide ions. So, in the second step of the research, organic ligand capped Yb^{3+}-doped nanoparticles are studied for applications like medical imaging. Details of the ligand capped nanoparticles are given in chapter 4.

The last part of the research is focused on the field of co-evaporated organo-lanthanide systems as a thermally deposited film, which is desirable for obtaining optical quality waveguide. In detail, by co-evaporating ytterbium(III) tetrakis(pentafluorophenyl) imidodiphosphinate, $Yb(F\text{-}TPIP)_3$ with a perfluorinated zinc-based organic chromophore, the zinc(II) salt of 2-(3,4,5,6-tetrafluoro-2-hydroxyphenyl)-4,5,6,7-tetrafluorobenzothiazole, $Zn(F\text{-}BTZ)_2$, Yb^{3+} can be largely sensitised through $Zn(F\text{-}BTZ)_2$ chromophore. Details of the co-evaporated organo-lanthanide system can be found in chapter 5.

1.2. Lanthanides

Lanthanides (Ln) are a group of elements in the periodic table from atomic number 57 to 71 (La, Ce, Pr, Nd, Pm, Sm, Eu, Gd, Tb, Dy, Ho, Er, Tm, Yb, Lu). It should be noted, the chemically similar Yttrium (Z = 39) and Scandium (Z = 21) together with the lanthanide ions are also known as rare earth (RE) ions. The neutral lanthanide atom has a Xe core, with a number of 4f electrons varying from 0 (La) to 14 (Lu) shielded by the outer 6s or 5d6s orbitals [10]. For La, Ce, Gd and Lu, the outer shell is 5d6s; and for all the rest, the outer shell is 6s. All lanthanide elements can form stable trivalent cations (Ln^{3+}) by losing two 6s electrons and another f or d electron. It should be mentioned that several lanthanide elements such as Ce, Sm, Eu and Yb can form other oxidation states as well. However, in this thesis, all discussions are about the trivalent lanthanide ions.

The chemical properties of lanthanide ions are similar, but, there are also some variations due to the different ionic radius [11]. However, their optical properties are quite different, and are mainly determined by the transitions within the 4f energy manifolds. The 4f electrons are shielded by the outer orbitals, making the optical properties almost independent of the host material and environment. The emission of the trivalent lanthanides is normally discrete narrow bands [12], long lifetime [13] due to the parity-forbidden 4f absorption coefficients.

It has been a challenge to rigorously describe the electronic configuration of a free lanthanide ion due to a number of complicated interactions, including the nuclear

attraction, inter-electronic repulsion and weak spin-orbital coupling [14]. Therefore, a simple coupling scheme was proposed by Russell-Saunders considering at the level of total angular momenta by using total spin quantum number S, total orbital angular quantum number L and total angular momentum number J. L can be the integer numbers 0, 1, 2, 3, 4, 5 and 6, which are represented as letters S, P, D, F, G, H and I. The value of J is determined and restricted to $|L - S| \leq J \leq |L + S|$ [15]. The energy level of the ground state of the trivalent lanthanide ion can be described in atomic spectroscopic terms $^{2S+1}L_J$ [16], where 2S+1 is the multiplicity of the term. In the ground level, if the 4f orbital is less half filled, J = L – S, otherwise J = L + S. Take the Er^{3+} ion for example, according to the Hund's rule, S = 3/2, L = 6 (I), and J = 15/2, the symbol is $^4I_{15/2}$. A full list of the electronic configurations of trivalent lanthanide ions in their ground state is given in table 1.1 below [16].

Table 1.1. *Electronic configuration of the trivalent lanthanide ions in their ground states.*

Ion	Number of 4f electrons	$\vec{S}$	$\vec{L}$	$\vec{J} = \vec{L} + \vec{S}$
La^{3+}	0	0	0	0
Ce^{3+}	1	1/2	3	5/2
Pr^{3+}	2	1	5	4
Nd^{3+}	3	3/2	6	9/2
Pm^{3+}	4	2	6	4
Sm^{3+}	5	5/2	5	5/2
Eu^{3+}	6	3	3	0
Gd^{3+}	7	7/2	0	7/2
Tb^{3+}	8	3	3	6
Dy^{3+}	9	5/2	5	15/2
Ho^{3+}	10	2	6	8
Er^{3+}	11	3/2	6	15/2
Tm^{3+}	12	1	5	6
Yb^{3+}	13	1/2	3	7/2
Lu^{3+}	14	0	0	0

1.3. 4f-4f transitions

The absorption and emission spectral bands of the lanthanide ions are due to the electronic transitions between two $^{2S+1}L_J$ energy manifolds. There are mainly three kinds of excitation transitions of the lanthanide ions: 4f-5d transitions, charge-transfer state transitions and 4f-4f transitions. In 4f-5d transitions, one of the 4f electrons is excited to the 5d orbital, which is typically observed with the Ce^{3+} ions. In the charge-transfer state transitions, the sp electrons of the neighbouring anions are transferred to the 4f orbital, which typically happens with the Eu^{3+} ions. [16] In this thesis, all the transitions discussed later relating to the Er^{3+} and Yb^{3+} ions are due to the third maain excitation transition: 4f-4f transitions, which involve the movements of electrons between different energy levels of the 4f orbitals within the same lanthanide ion. There are three main mechanisms of the 4f-4f transitions: (1) the magnetic dipole transition; (2) induced electric dipole transition and (3) electric quadrupole transition [17].

1.3.1. Magnetic dipole transition

The magnetic dipole transition is due to the interaction between the active ion (lanthanide) and magnetic field component of the light through a magnetic dipole. Intensity of the magnetic dipole transition is proportional to the square of the transition dipole moment. Considering the small size of an ion, the curvature displacement will be small, thus the intensity of magnetic dipole transition is normally very weak for the most of lanthanide ions. However, it is of interest and used as intensity standards for various doping hosts, because it is independent of

the environment. Magnetic dipole can be considered as a rotational displacement of charge: the sense of rotation cannot be reversed under point reversion, thus magnetic dipole transition has even parity [17].

1.3.2. Induced electric dipole transition

The induced electric dipole transition is the main observed optical transition in lanthanide ions, which is due to the interaction of the active lanthanide ion and the electric field vector through an electric dipole. The electric dipole operator has odd parity as it supposes a linear movement of charge. The intra-configurational electric dipole transition is forbidden due to the Laporte parity rules. But in reality, weak and narrow emissions are observed [18], which are mainly due to the mixing of the 4f wave functions with the opposite-parity wave functions of the crystal field such as the 5d states, charge transfer states and so on [19]. Thus, they are often called induced electric dipole transitions.

1.3.3. Electric quadrupole transition

The electric quadrupole transitions arise from a displacement of charge that has a quadrupole nature. It can be considered as two electric dipoles aligned in different directions. Electrical quadrupole transition is much weaker compared with the magnetic dipole transition and induced electrical dipole transition. And it should be mentioned that no experimental evidence exists for the occurrence of quadrupole transition in lanthanide ions [17].

1.4. The Dieke diagram

The Dieke diagram was firstly built by Dieke et al. in the 1960's and was based on the measurements of the lanthanide doped $LaCl_3$, after which it was extended by Ogasawara [20, 21]. Since then, the Dieke diagram has been commonly used as a reference for estimating the absorption and emission spectra of the trivalent lanthanide ions embedded in any host matrix, as the optical characteristics are not affected much by the crystal environment. A typical Dieke diagram is illustrated in figure 1.1 below.

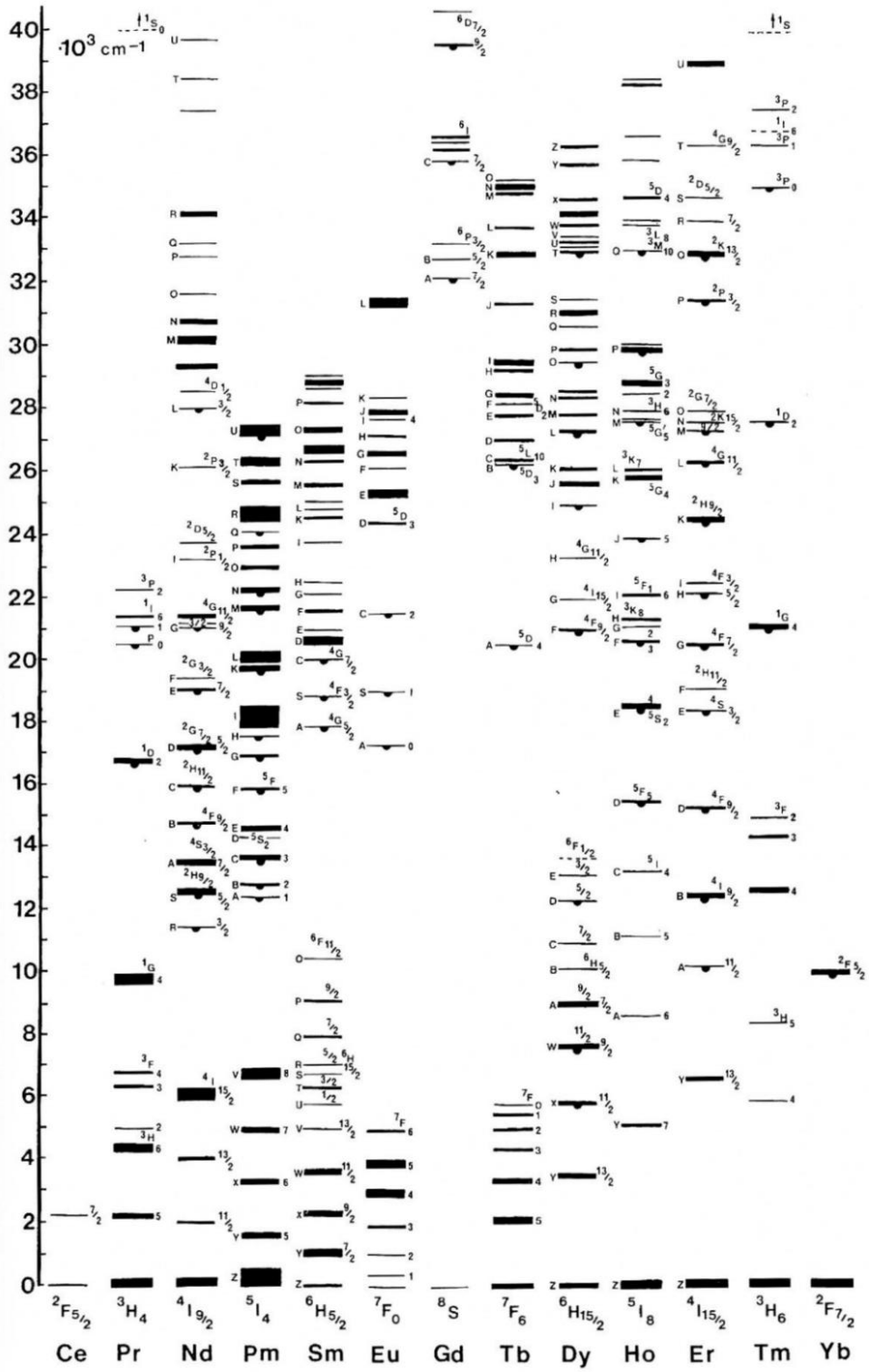

Figure 1.1. *The Dieke diagram: energy levels of the $^{2S+1}L_J$ multiplet manifolds of trivalent lanthanide ions. It is taken from the reference [20].*

1.5. Radiative and non-radiative decay

Once the lanthanide ions are excited, there will be luminescence, which corresponds to the radiative decay from the excited states. And the energy of the emitted light is equal to the energy gap between the excited and ground states. In addition to that, there is a possibility of non-radiative decay, a process where the excited lanthanide ion decays to the ground state without the emission of photons. Both the radiative and non-radiative decay processes are illustrated in figure 1.2 below:

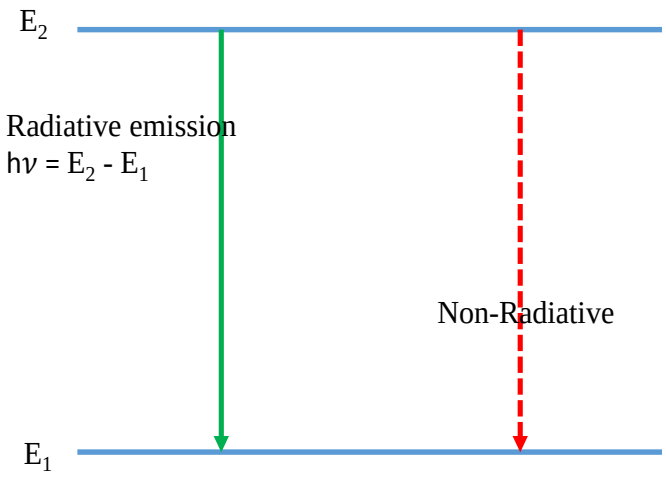

Figure 1.2. *Trivalent lanthanide de-excitation process: the green line represents the radiative emission while the dashed red line represents the non-radiative process.*

In the simple two-level system of a trivalent lanthanide shown above, when the electrons are de-excited from high-lying energy level E_2 to energy level E_1 by spontaneous emission of photons and non-radiative processes, the differential dynamic equation of the energy level E_2's population n_2 is given by:

$$\frac{\mathrm{d}n_2(t)}{\mathrm{d}t} = -An_2(t) = -(A_r + A_{nr})n_2(t) \tag{1.1}$$

where A is the total decay rate, which is a summary of the radiative decay rate (A_r) and non-radiative decay rate (A_{nr}). Similarly, the experimentally measured lifetime τ is defined as the inverse of the decay rate A:

$$\tau = \frac{1}{A} = \frac{1}{A_r + A_{nr}} \tag{1.2}$$

and the radiative quantum efficiency can be expressed by the following equation:

$$\eta_r = \frac{A_r}{A} = \frac{A_r}{A_r + A_{nr}} \tag{1.3}$$

As can be seen from equation 1.3, the quantum efficiency cannot be 100% as a result of the non-radiative processes, which are due to quenching by a variety of processes such as hydroxyl, hydro-carbons and hydro-nitrates groups (A_H), multiphonon relaxations (A_{MP}) and the interactions between the lanthanide ions (A_{ET}) [22-24]. In addition, the measured lifetime τ of the organo-lanthanide complex is extremely sensitive to the O–H and C–H bonds [25], which is due to the small energy difference between the excited states of lanthanides and the vibrational energy of the chemical bonds (see subsection 1.5.1). In chapter 5, there is a detailed discussion about the lifetime of Yb^{3+} complex regarding different synthesis environments.

1.5.1. Vibrational oscillator quenching

Lifetime of Er^{3+} and Yb^{3+} is sensitive to high energy vibrational oscillators, such as O–H and C–H chemical bonds. For example, the measured lifetimes of erbium and ytterbium complexes are much shorter compared with their intrinsic lifetimes. Figure 1.3 below shows the energy gaps of Er^{3+}, Yb^{3+} in comparison with the vibrational chemical bonds such as O–H, C–H and C–F. The high energy O–H (3450 cm^{-1}) and C–H (2950 cm^{-1}) bonds can effectively quench the NIR luminescence of Er^{3+} ($^4I_{11/2}$) and Yb^{3+} ($^4F_{5/2}$) ions. Yb^{3+} is less sensitive to the oscillators than Er^{3+} as there is a bigger energy gap mismatch between $^4F_{5/2}$ and the vibrational excited states of the chemical bonds. This does explain the high quantum yield (79%) of $Yb(F\text{-}TPIP)_3$ we get (details are given in chapter 5), while the quantum yield of $Er(F\text{-}TPIP)_3$ is less than 10% [2]. Interestingly, the vibrational energy of C–F bond (1250 cm^{-1}) is much lower than the C–H bond, which suppresses the quenching process of lanthanide ions. Therefore, fluorination is our strategy to reduce the vibrational oscillator quenching effect in our co-doped organic lanthanide complexes.

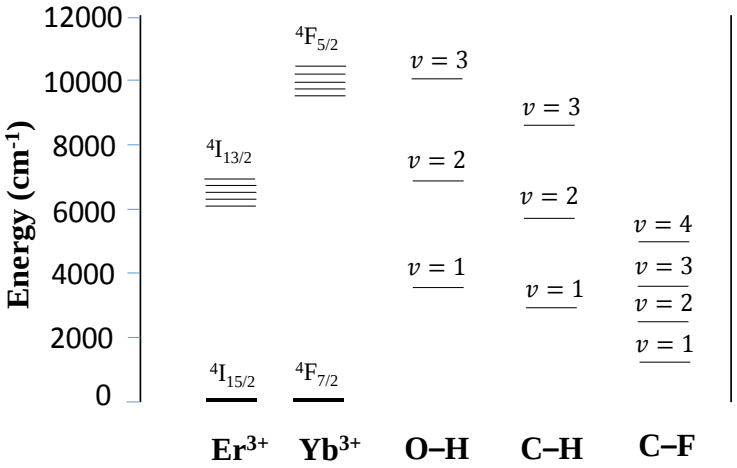

Figure 1.3. *Energy gap of Er^{3+}, Yb^{3+} compared with the O–H, C–H and C–F chemical bonds.*

1.5.2. Multiphonon relaxation

Multiphonon relaxation is another important non-radiative process. It competes with the radiative de-excitation by transferring the energy of the excited ions to the lattice and then the energy is released by means of phonon emission. Multiphonon relaxation rate A_{MP} varies exponentially with the decrease of the energy gap, and is temperature dependent:

$$A_{MP}(T) = A_{MP}(0)e^{-\alpha\Delta E} \tag{1.4}$$

$A_{MP}(0)$ is the multiphonon relaxation rate at $T = 0$ K, α is the host-dependent positive constants, and ΔE is the energy gap between the excited energy level and the next lying level.

1.5.3. Concentration quenching

Emitted light intensity normally increases with the concentration of luminescent centres to a critical concentration. Above this concentration, intensity starts to decrease. This process is called concentration quenching. The origin of the concentration quenching is due to the efficient energy transfer among the excited lanthanide ions when the distance between them is small enough. The more efficient the energy transfers, the higher the probability that energy can be quenched by defect centres, therefore, there are more chances for the non-radiative processes happen. Thus, the decay time of the emitting energy level is reduced consequently. Experimentally, the easiest way to detect concentration quenching is to measure the lifetime of the excited lanthanide ions as a function of concentration rather than measuring the quantum efficiency [26].

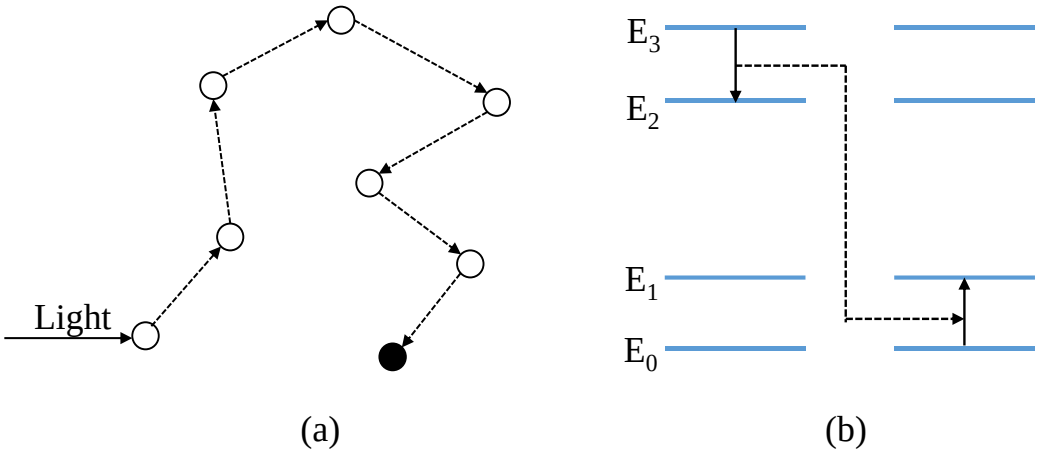

Figure 1.4 (a). *Concentration quench due to the quenching traps. Circles represent the donors and the black circle represents the quenching trap;* ***(b).*** *Cross relaxation between pairs of lanthanide ions [26].*

Concentration quenching is one of the most important quenching pathways. It is due to the interaction between a pair of lanthanide ions, therefore, the non-radiative decay rate varies with the square of dopant concentration. The higher the dopant concentration, the more probable it is that energy transfer can happen. There are two kinds of main concentration quenching mechanisms. One is quenching traps: the excitation energy can migrate among lots of ions (donors) until it reaches the quenching traps (such as defects), as illustrated in figure 1.4 (a). And the other is cross relaxation: part of the absorbed energy of one luminescent ion is transferred to another identical ion by resonant energy transfer, as shown in figure 1.4 (b) above. These two kinds of concentration quenching are discussed in chapter 3.

According to the Förster-Dexter theory [27, 28], the non-radiative decay rate (A_{ET}) due to concentration quench can be expressed as follows [29]:

$$A_{ET} = A_r \sum_{s=6,8,10} \left[\frac{R_0}{R_{ij}}\right]^s \tag{1.5}$$

where A_r is the radiative decay rate, which can be predicted with the Judd-Ofelt theory discussed in the subsection 1.6, R_{ij} is the inter-ionic separation, R_0 is the critical separation. Also of the note are the expressions: $A_r \left[\frac{R_0}{R_{ij}}\right]^6$, $A_r \left[\frac{R_0}{R_{ij}}\right]^8$ and $A_r \left[\frac{R_0}{R_{ij}}\right]^{10}$, which are the transition probabilities of dipole-dipole interactions, dipole-quadrupole interactions, quadrupole-quadrupole interactions respectively. Dipole-dipole transfers are the main operating mechanisms for concentration quenching (metal to metal energy transfer processes). Therefore,

$$A_{ET} = A_r \left[\frac{R_0}{R_{ij}}\right]^6 \quad (1.6)$$

1.6. Judd-Ofelt theory

The Judd-Ofelt theory was built independently by Judd and Ofelt in 1962 [30, 31]. The idea that an admixture of the opposite parity can relax the $4f^n$ dipole transitions is the basis of the Judd-Ofelt theory. Judd-Ofelt has been commonly used to predict the 4f-4f optical transition properties of the lanthanide ions within a crystal structure for branching ratios, especially for the spontaneous radiative emission rates and lifetimes.

The radiative decay rate A_r of the electronic transition from an initial state $^{2S+1}L_J$ to final state $^{2S'+1}L'_{J'}$ can be calculated according to the Judd-Ofelt theory as [26]:

$$A_r = A_{ED} + A_{MD} = \frac{8\pi^2 e^2}{mc\lambda^2} f_{ED} + \frac{8\pi^2 e^2}{mc\lambda^2} f_{MD} \quad (1.7)$$

where the A_{ED} and A_{MD} are the spontaneous transition probability for electric dipole (ED) transitions and magnetic dipole (MD) transitions, and are determined by the oscillator strength f_{ED} and f_{MD} separately, m is the mass of the electron, c is the speed of light in vacuum, λ is the average transition wavelength, e is electronic charge.

It should be mentioned that the strength of the magnetic dipole transition (f_{MD}) is only 10^{-6} of that of an electric dipole transition (f_{ED}). Thus, f_{MD} is excluded from

the discussion below. For the electric dipole transitions, f_{ED} is related to the dipole strength D by

$$f_{ED} = \frac{8\pi^2 mc}{3he^2\lambda} D \tag{1.8}$$

And the dipole strength D is defined by

$$D = \left|\langle \psi_i | \hat{o} | \psi_f \rangle\right|^2 \tag{1.9}$$

where ψ_i and ψ_f are the initial and final wave functions, and $\hat{o}$ is the electric dipole operator.

In order to compare the calculated dipole strength with the experimental one, the correction factor for the dielectric medium and the degeneracy of the initial levels have to be considered:

$$D_{exp} = \frac{1}{2J+1} \chi_{ED} D \tag{1.10}$$

where $2J+1$ is the degeneracy, and for the medium with the refractive index n, the correction factor χ_{ED} is

$$\chi_{ED} = \frac{n(n^2+2)^2}{9} \tag{1.11}$$

In summary, the spontaneous radiative decay rate A_r can be calculated using:

$$A_r = \frac{64\pi^4}{3h\lambda^3(2J+1)}\chi_{ED}\left|\langle\psi_i|\hat{o}|\psi_f\rangle\right|^2 \quad (1.12)$$

The radiative lifetime τ of an emitting state $^{2S'+1}L'_{J'}$ is related to the spontaneous emission probabilities of all transition from this state to the under-lying states $^{2S+1}L_J$ [13]:

$$\tau = \frac{1}{\sum_J A_r(J'-J)} \quad (1.13)$$

1.7. Up-conversion (UC) mechanism

The history of up-conversion (UC) can be traced back to 1959. Bloemgergen proposed an idea that infrared (IR) photons could be detected and counted through sequential absorption (ESA) within the levels of a given ion [32]. But the role of energy transfer in UC was first recognised by Auzel in 1966. And since the discovery in the 1960s, lanthanide doped UC materials, which can convert infrared radiation into visible luminescence via a variety of processes, including excited state absorption (ESA) and energy transfer (ET) [18, 33], have been widely investigated. Most of the UC work is based on the lanthanide doped halide [34-39], oxide [40-43] and glasses [44-47]. And a few works have been done with the organo-lanthanide materials [2, 48].

This variety of UC works are mainly observed and investigated through lifetime, excitation and emission spectra measurements [49]. Especially, time-resolved spectroscopy plays an important role in understanding the dominant mechanisms of the UC processes [13], and has been the main research tool used throughout the PhD period. The time-resolved spectroscopy technique is described in detail in chapter 2.

The main UC mechanisms are believed to be excited state absorption (ESA), sensitised energy transfer (ETU), cooperative up-conversion and photon avalanche [18, 49], all of which are explained in the subsections below (1.7.1 – 1.7.4).

1.7.1. Excited state absorption (ESA)

In the simplest UC process of the Er^{3+} ion doped matrix shown in figure 1.5, absorbing one 980 nm photon by ground state absorption (GSA) populates the $^4I_{11/2}$ state. Provided that the lifetime of the $^4I_{11/2}$ state is long enough (in the order of ms), there is a possibility of absorbing the second 980 nm photon. The successful absorption of the second 980 nm photon further excites the Er^{3+} ion from the intermediate $^4I_{11/2}$ state to the high-lying $^4F_{7/2}$ state ($^4I_{11/2} + h\nu \rightarrow {}^4F_{7/2}$), and the 490 nm photon emission from the exited high-lying $^4F_{7/2}$ state to the ground state ($^4F_{7/2} \rightarrow {}^4I_{15/2}$) is called UC emission.

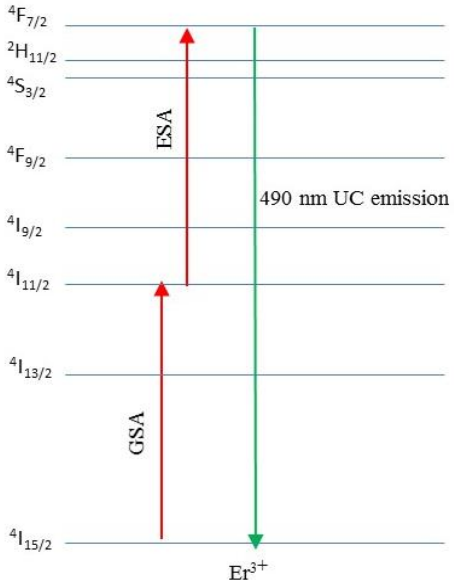

Figure 1.5. *ESA UC mechanism in the simplest Er^{3+} system.*

1.7.2. Sensitised energy transfer up-conversion (ETU)

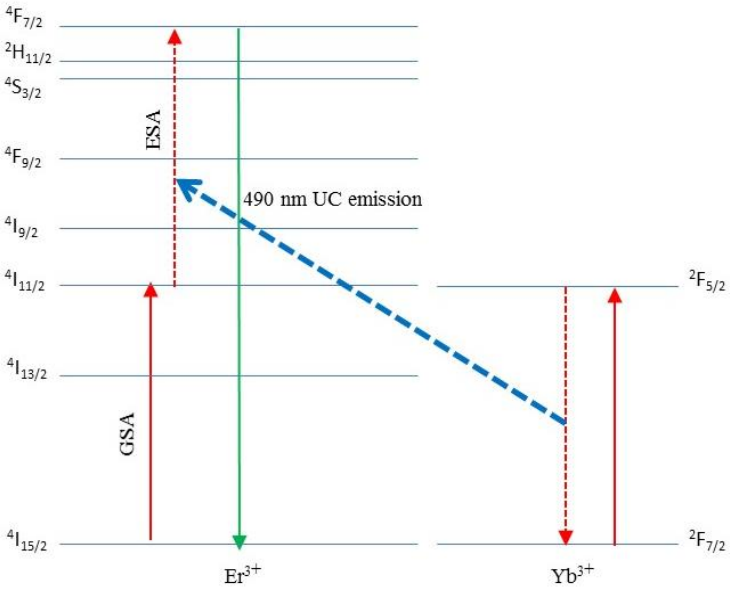

Figure 1.6. *ETU mechanism in the Er^{3+}-Yb^{3+} system.*

Compared with ESA, ETU is at least two orders of magnitude more efficient [18], and involves non-radiative energy transfer between two neighbouring ions. In the commonly investigated Er^{3+}-Yb^{3+} system illustrated above, Yb^{3+} is called the sensitiser and Er^{3+} is called the activator. Usually, the sensitiser has a large absorption cross section at a typical excitation wavelength. In this case, once Yb^{3+} is excited at a 980 nm wavelength, it passes the energy to the neighbouring Er^{3+} activator ion to promote it from the excited state $^4I_{11/2}$ to the upper state $^4F_{7/2}$ by relaxing itself to a lower state $^2F_{7/2}$ (ground state in figure 1.6). The ETU process happens between neighbouring ions, thus it is concentration dependent, as discussed above in the concentration quench section.

1.7.3. Cooperative luminescence and sensitisation up-conversion

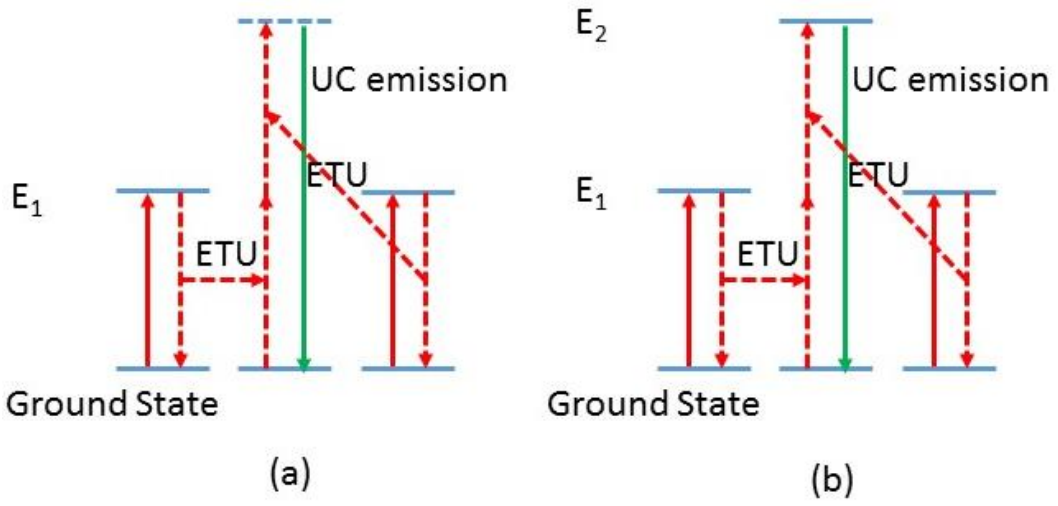

Figure 1.7 (a). *Mechanism of the cooperative luminescence UC;* ***(b).*** *Mechanism of the cooperative sensitisation UC.*

Cooperative UC is less efficient then ESA UC or ETU discussed above. There are two kinds of cooperative UC: cooperative luminescence UC and cooperative sensitisation UC. These two processes are quite similar, as shown in figure 1.7 (a) and 1.7 (b) above. In the cooperative UC process, two excited ions decay simultaneously to the ground state, with emission of a single phonon which combines the energy of these two ions. The difference between cooperative luminescence and cooperative sensitisation UC is that cooperative luminescence comes from a virtual level, thus the emission probability is extremely low, while the luminescence due to cooperative sensitisation is from the real high-lying energy state E_2 of a third ion.

1.7.4. Avalanche up-conversion

Avalanche UC happens due to the multi-interactions between several absorption and energy transfer processes [50]. A schematic diagram of avalanche UC is given in figure 1.8. E_1 has to be populated with non-resonant GSA, while E_2 is populated by the subsequent resonant ESA. And there must be a strong cross relaxation process between the excited ion and the neighbouring ground state ion (see the dashed red line). Thus, the population of E_2 is initially through cross relaxation and then ESA. It should be noted that there is a certain high threshold value for this kind of avalanche UC, making it impractical for real applications.

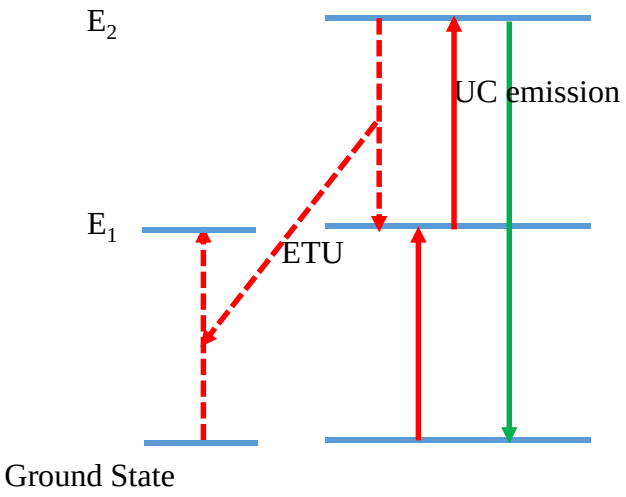

Figure 1.8. *Mechanism of the avalanche UC in the simple three level system.*

1.8. UC rate equations in a simplified Er^{3+}-doped system

It is still hard to use the dynamic differential rate equations to accurately model the UC processes in the practical systems. One reason is that there are too many processes involved, including the GSA/ESA, energy transfer, radiative and non-radiative decays, cross relaxation and concentration quenches. This will be discussed in detail in chapter 3, regarding the Er^{3+}-doped Y_2O_3 system. And the other reason is that different dopants incorporated in the host lattice have different energy levels, which makes the whole discussion more complicated. However, according to the UC rate equations, lots of general conclusions can be made, with the necessary assumptions and limitations [51, 52], that the ground state population density n_0 is constant and the whole system is continuously pumped into the intermediated state by GSA.

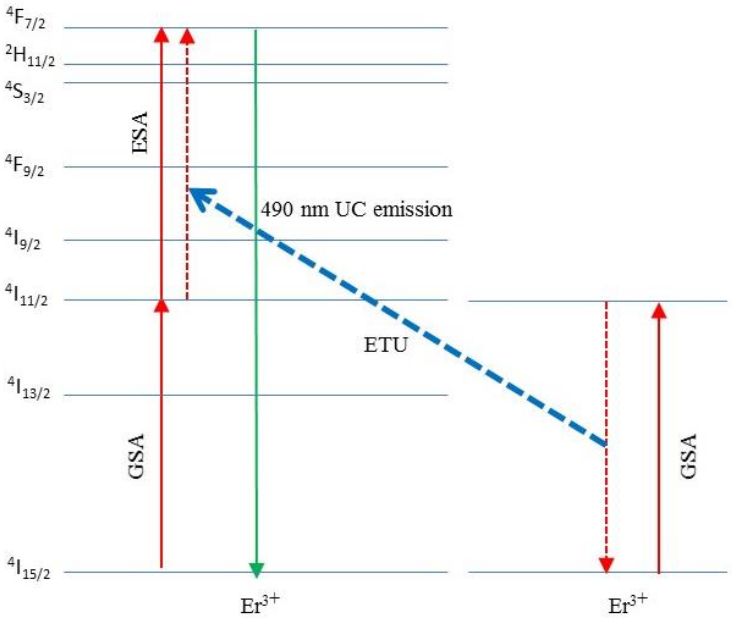

Figure 1.9. *The UC mechanism involves GSA, ESA and ETU processes in the simplest single Er^{3+}-doped system.*

In the simplified single Er^{3+}-doped system (figure 1.9), the three levels considered are $^4I_{15/2}$ (ground state), $^4I_{11/2}$ (intermediate state) and $^4F_{7/2}$ (up-conversion emitting state) [53]. And it is assumed that all levels between the $^4I_{11/2}$ and $^4F_{7/2}$ states will quickly non-radiatively decay to the $^4I_{11/2}$ state. n_0, n_1 and n_2 are the population densities of the ground state, $^4I_{11/2}$ state and $^4F_{7/2}$ state, respectively. We have:

$$\frac{\mathrm{d}n_1}{\mathrm{d}t} = A_0 n_0 - A_1 n_1 - \frac{n_1}{\tau_{r1}} - 2W_1 {n_1}^2 \tag{1.14}$$

$$\frac{\mathrm{d}n_2}{\mathrm{d}t} = A_1 n_1 - \frac{n_2}{\tau_{r2}} + W_1 {n_1}^2 \tag{1.15}$$

where A_0 and A_1 are the absorption of the pump rates in ground state and intermediate state $^4I_{11/2}$ respectively, τ_{r1} and τ_{r2} are the radiative decay time of the intermediate state $^4I_{11/2}$, and up-conversion emitting state $^4F_{7/2}$ and W_1 is the energy transfer up-conversion rate.

1.8.1. UC rate equation discussion when ETU is dominant

When the ETU is dominant during the UC process, $A_1 n_1$ part can be neglected. Thus, the new UC rate equations are as follows:

$$\frac{dn_1}{dt} = A_0 n_0 - \frac{n_1}{\tau_{r1}} - 2W_1 {n_1}^2 \tag{1.16}$$

$$\frac{dn_2}{dt} = -\frac{n_2}{\tau_{r2}} + W_1 {n_1}^2 \tag{1.17}$$

If $\frac{n_1}{\tau_{r1}} \ll 2W_1 {n_1}^2$, one gets $n_2 \propto A_0 \propto p$; otherwise, one gets $n_2 \propto p^2$, where p is the pumping power.

1.8.2. UC rate equation discussion when ESA is dominant

When ESA is dominant during the UC process, $W_1 {n_1}^2$ can be neglected. The new UC rate equations become:

$$\frac{\mathrm{d}n_1}{\mathrm{d}t} = A_0 n_0 - A_1 n_1 - \frac{n_1}{\tau_{r1}} \tag{1.18}$$

$$\frac{\mathrm{d}n_2}{\mathrm{d}t} = A_1 n_1 - \frac{n_2}{\tau_{r2}} \tag{1.19}$$

If $A_1 n_1 \ll \frac{n_1}{\tau_{r1}}$, then $n_2 \propto p$; otherwise, one gets $n_2 \propto p^2$.

1.9. Summary

In this introductory chapter, the general background of lanthanide ions, the potential applications, and the research motivations are discussed in detail. In addition, the detailed optical and physical properties of the lanthanide ions, including electronic configuration, 4f-4f transitions, Dieke diagram and Judd-Ofelt theory, are explained. Lastly, different types of UC processes are identified and general dynamic equations are discussed within the simplest Er^{3+}-doped three level system.

1.10. Aims of the research

The first goal of the PhD was to gain an in-depth understanding of the Up- and Down-conversion mechanisms, which are commonly used in the applications mentioned in chapter 1.1. In addition to the basic understanding, the second goal was to demonstrate novel energy transfer within organic ligand capped Yb^{3+}-doped $NaYF_4$ nanoparticles system, and co-evaporated organo-lanthanide system.

1.11. Reference

[1] J. -C. G. Bünzli, C. Piguet, Taking advantage of luminescent lanthanide ions, *Chemical Society Reviews*, **34** (2005) 1048-1077.

[2] H. Ye, Z. Li, Y. Peng, C. Wang, T. Li, Y. Zheng, A. Sapelkin, G. Adamopoulos, I. Hernández, P. B. Wyatt, W. P. Gillin, Organo-erbium systems for optical amplification at telecommunications wavelengths, *Nature Materials*, **13** (2014) 382-386.

[3] R. Paschotta, J. Nilsson, A. C. Tropper, D. C. Hanna, Ytterbium-doped fibre amplifiers, *IEEE Journal of Quantum Electronics*, **33** (1997) 1049-1056.

[4] A. Ikesue, T. Kinoshita, K. Kamata, K. Yoshida, Fabrication and optical properties of high-performance polycrystalline Nd:YAG ceramics for solid-state lasers, *Journal of the American Ceramic Society*, **78** (1995) 1033-1040.

[5] V. W. -W. Yam, K. K. -W. Lo, Recent advances in utilization of transition metal complexes and lanthanides as diagnostic tools, *Coordination Chemistry Reviews*, **184** (1999) 157-240.

[6] S. Faulkner, S. J. A. Pope, B. P. Burton-Pye, Lanthanide complexes for luminescence imaging applications, *Applied Spectroscopy Reviews*, **40** (2005) 1-31.

[7] M. Kong, W. Hu, F. Cheng, Z. Huang, J. Zhang, Z. Han, N. Shi, Q. Fan, S. Chen, W. Huang, Efficiency enhancement in P3HT-based polymer solar cells with a $NaYF_4$:2% Er^{3+}, 18% Yb^{3+} up-converter, *Journal of Materials Chemistry C*, **1** (2013) 5872-5878.

[8] Z. Li, A. Dellali, J. Malik, M. Motevalli, R. M. Nix, T. Olukoya, Y. Peng, H. Ye, W. P. Gillin, I. Hernández, P. B. Wyatt, Luminescent zinc (II) complexes of fluorinated benzothiazol-2-yl substituted phenoxide and enolate ligands, *Inorganic Chemistry*, **52** (2013) 1379-1387.

[9] J. -C. G. Bünzli, S. V. Eliseeva, Lanthanide NIR luminescence for telecommunications, bioanalyses and solar energy conversion, *Journal of Rare Earths*, **28** (2010) 824-842.

[10] B. Henderson, G. F. Imbusch, Optical spectroscopy of inorganic solids, **44**, *Oxford University Press*, 2006.

[11] F. Wang, Y. Han, C. S. Lim, Y. Lu, J. Wang, J. Xu, H. Chen, C. Zhang, M. Hong, X. Liu, Simultaneous phase and size control of upconversion nanocrystals through lanthanide doping, *Nature*, **463** (2010) 1061-1065.

[12] H. Lu, W. P. Gillin, I. Hernández, Concentration dependence of the up- and down-conversion emission colours of Er^{3+}-doped Y_2O_3: a time-resolved spectroscopy analysis, *Physical Chemistry Chemical Physics*, **16** (2014) 20957-20963.

[13] I. Etchart, Metal oxides for efficient infrared to visible upconversion, Materials Science and Metallurgy, University of Cambridge, Cambridge, 2010.

[14] J.-C. G. Bünzli, S. V. Eliseeva, Basics of lanthanide photophysics, Lanthanide luminescence, *Springer*, **7** (2011) 1-45.

[15] M. Fox, Optical properties of solids, *Oxford University Press Inc*, New York, 2001.

[16] G. I. Hatakoshi, Phosphor handbook, 2nd ed., *CRC Press*, New York, 2006.

[17] C. Görller-Walrand, K. Binnermans, K. Gschneidner Jr, L. Eyring, Handbook on the physics and chemistry of rare earths, 1998.

[18] F. Auzel, Upconversion and anti-stokes processes with f and d ions in solids, *Chemical Reviews*, **104** (2004) 139-174.

[19] J. H. V. Vleck, The puzzle of rare-earth spectra in solids, the *Journal of Physical Chemistry*, **41** (1937) 67-80.

[20] G. H. Dieke, Spectra and energy levels of rare earth ions in crystals, *Wiley Interscience*, New York, 1968.

[21] G. H. Dieke, H. Crosswhite, The spectra of the doubly and triply ionized rare earths, *Applied Optics*, **2** (1963) 675-686.

[22] Y. Yan, A. J. Faber, H. De Waal, Luminescence quenching by OH groups in highly Er-doped phosphate glasses, *Journal of Non-Crystalline Solids*, **181** (1995) 283-290.

[23] E. Okamoto, M. Sekita, H. Masui, Energy transfer between Er^{3+} ions in LaF_3, *Physical Review B*, **11** (1975) 5103-5111.

[24] M. J. Weber, Multiphonon relaxation of rare-earth ions in yttrium orthoaluminate, *Physical Review B*, **8** (1973) 54-64.

[25] G. Mancino, A. J. Ferguson, A. Beeby, N. J. Long, T. S. Jones, Dramatic increases in the lifetime of the Er^{3+} ion in a molecular complex using a perfluorinated imidodiphosphinate sensitizing ligand, *Journal of the American Chemical Society*, **127** (2005) 524-525.

[26] J. G. Solé, L. E. Bausá, D. Jaque, An introduction to the optical spectroscopy of inorganic solids, Wiley, 2005.

[27] D. L. Dexter, A theory of sensitized luminescence in solids, *The Journal of Chemical Physics*, **21** (1953) 836-850.

[28] V. T. Förster, Zwischenmolekulare energiewanderung und fluoreszenz, *Annalen Der Physik*, **437** (1948) 55-75.

[29] G. A Kumar, C. W. Chen, R. E. Riman, Optical spectroscopy and confocal fluorescence imaging of upconverting Er^{3+}-doped CaF_2 nanocrystals, *Applied Physics Letters*, **90** (2007) 093123.

[30] B. R. Judd, Optical absorption intensities of rare-earth ions, *Physical Review*, **127** (1962) 750-761.

[31] G. S. Ofelt, Intensities of crystal spectra of rare-earth ions, *The Journal of Chemical Physics*, **37** (1962) 511-520.

[32] N. Bloembergen, Solid state infrared quantum counters, *Physical Review Letters*, **2** (1959) 84-85.

[33] F. Vetrone, J. C. Boyer, J. A. Capobianco, Yttrium oxide nanocrystals: luminescent properties and applications, *The Encyclopedia of Nanoscience and Nanotechnology*, **10** (2004) 725-765.

[34] J. -C. Boyer, F. Vetrone, L. A. Cuccia, J. A. Capobianco, Synthesis of colloidal upconverting $NaYF_4$ nanocrystals doped with Er^{3+}, Yb^{3+} and Tm^{3+}, Yb^{3+} via thermal decomposition of lanthanide trifluoroacetate precursors, *Journal of the American Chemical Society*, **128** (2006) 7444-7445.

[35] A. Aebischer, S. Heer, D. Biner, K. Krämer, M. Haase, H. U. Güdel, Visible light emission upon near-infrared excitation in a transparent solution of nanocrystalline β-$NaGdF_4$: Yb^{3+}, Er^{3+}, *Chemical Physics Letters*, **407** (2005) 124-128.

[36] S. Heer, K. Kömpe, H. U. Güdel, M. Haase, Highly efficient multicolour upconversion emission in transparent colloids of lanthanide-doped $NaYF_4$ nanocrystals, *Advanced Materials*, **16** (2004) 2102-2105.

[37] M. Pollnau, D. R. Gamelin, S. R. Lüthi, H. U. Güdel, M. P. Hehlen, Power dependence of upconversion luminescence in lanthanide and transition-metal-ion systems, *Physical Review B*, **61** (2000) 3337-3346.

[38] J. J. Owen, A. K. Cheetham, R. A. McFarlane, Orientation-dependent fluorescence studies and spectroscopic analysis of doped barium yttrium fluoride upconversion laser crystals ($BaY_{2-x-y}Yb_xTm_yF_8$), *Journal of the Optical Society of America B*, **15** (1998) 684-693.

[39] J. J. Owen, A. K. Cheetham, N. A. Nighman, R. H. Jarman, R. J. Thrash, Modified bridgman growth of oriented Er-doped and Tm-doped $BaY_{2-x}Yb_xF_8$ crystals for upconversion visible laser operation, *Journal of the Optical Society of America B*, **11** (1994) 919-922.

[40] A. M. Pires, O. A. Serra, S. Heer, H. U. Güdel, Low-temperature upconversion spectroscopy of nanosized Y_2O_3:Er, Yb phosphor, *Journal of Applied Physics*, **98** (2005) 063527-063529.

[41] A. Patra, C. S. Friend, R. Kapoor, P. N. Prasad, Fluorescence upconversion properties of Er^{3+}-doped TiO_2 and $BaTiO_3$ nanocrystallites, *Chemistry of Materials*, **15** (2003) 3650-3655.

[42] A. Patra, C. S. Friend, R. Kapoor, P. N. Prasad, Upconversion in Er^{3+}:ZrO_2 nanocrystals, *The Journal of Physical Chemistry B*, **106** (2002) 1909-1912.

[43] J. A. Capobianco, F. Vetrone, J. C. Boyer, A. Speghini, M. Bettinelli, Visible upconversion of Er^{3+} doped nanocrystalline and bulk Lu_2O_3, *Optical Materials*, **19** (2002) 259-268.

[44] M. P. Hehlen, N. J. Cockroft, T. R. Gosnell, A. J. Bruce, Spectroscopic properties of Er^{3+}-and Yb^{3+}-doped soda-lime silicate and aluminosilicate glasses, *Physical Review B*, **56** (1997) 9302-9318.

[45] X. Zou, T. Izumitani, Spectroscopic properties and mechanisms of excited state absorption and energy transfer upconversion for Er^{3+}-doped glasses, *Journal of Non-Crystalline Solids*, **162** (1993) 68-80.

[46] Y. Wang, J. Ohwaki, New transparent vitroceramics codoped with Er^{3+} and Yb^{3+} for efficient frequency upconversion, *Applied Physics Letters*, **63** (1993) 3268-3270.

[47] S. Tanabe, S. Yoshii, K. Hirao, N. Soga, Upconversion properties, multiphonon relaxation, and local environment of rare-earth ions in fluorophosphate glasses, *Physical Review B*, **45** (1992) 4620-4625.

[48] I. Hernández, N. Pathumakanthar, P. B. Wyatt, W. P. Gillin, Cooperative infrared to visible up conversion in Tb^{3+}, Eu^{3+}, and Yb^{3+} containing polymers, *Advanced Materials*, **22** (2010) 5356-5360.

[49] D. R. Gamelin, H. U. Güdel, Upconversion processes in transition metal and rare earth metal systems, Springer, 2001, 1-56.

[50] M. -F. Joubert, Photon avalanche upconversion in rare earth laser materials, *Optical Materials*, **11** (1999) 181-203.

[51] J. Zhao, Z. Lu, Y. Yin, C. McRae, J. A. Piper, J. M. Dawes, D. Jin, E. M. Goldys, Upconversion luminescence with tunable lifetime in $NaYF_4$:Yb, Er nanocrystals: role of nanocrystal size, *Nanoscale*, **5** (2013) 944-952.

[52] P. S. Golding, S. D. Jackson, T. A. King, M. Pollnau, Energy transfer processes in Er^{3+}-doped and Er^{3+}, Pr^{3+}-codoped ZBLAN glasses, *Physical Review B*, **62** (2000) 856-864.

[53] J. Zhao, D. Jin, E. P. Schartner, Y. Lu, Y. Liu, A. V. Zvyagin, L. Zhang, J. M. Dawes, P. Xi, J. A. Piper, E. M. Goldys, T. M. Monro, Single-nanocrystal sensitivity achieved by enhanced upconversion luminescence, *Nature Nanotechnology*, **8** (2013) 729-734.

Chapter 2: Experimentation and methodology

2.1. Introduction

This chapter will present in detail the following: the synthesis and characterisation of Er^{3+}-doped Y_2O_3, the HL ligand capped Yb^{3+}-doped $NaYF_4$ nanoparticles, the co-evaporation of $Yb(F\text{-}TPIP)_3$ and $Zn(F\text{-}BTZ)_2$ thin films, experimental optical instruments, measurements and set up.

Er^{3+}-doped Y_2O_3 was synthesised through a conventional spray pyrolysis method, which is shown in subsection 2.2. Ligand capped Yb^{3+}-doped $NaYF_4$ nanoparticles were synthesised using a two-step method. Firstly, the $NaYF_4$ nanoparticles were produced through a commonly known hydrothermal method. Secondly, the ligand capped $NaYF_4$ nanoparticles were prepared under a straight forward chemical reaction using the synthesised nanoparticles and pre-prepared HL ligand. This is shown in subsection 2.3. $Yb(F\text{-}TPIP)_3$ was chemically produced though $YbCl_3 \cdot 6H_2O$ and HF-TPIP. Then, it was co-evaporated with $Zn(F\text{-}BTZ)_2$ in order to get an efficient sensitization of Yb^{3+} ions, as described in subsection 2.4.

Material characterisation techniques are described in subsection 2.5, including structure characterisation which was performed using the X-ray diffraction (XRD) method, doping concentration, which was confirmed with energy-dispersive X-ray spectroscopy (EDS), and the nanoparticle size, which was confirmed with transmission electron microscopy (TEM).

The optical measurement instruments, including an optical parametric oscillator (OPO), Apex Arc lamp, continuous wave (CW) lasers, spectrometer, photomultiplier, oscilloscope, lock-in amplifier, U-3000 spectrophotometer are all described in subsection 2.6, along with the experimental set up.

2.2. Synthesis of Er^{3+}-doped Y_2O_3

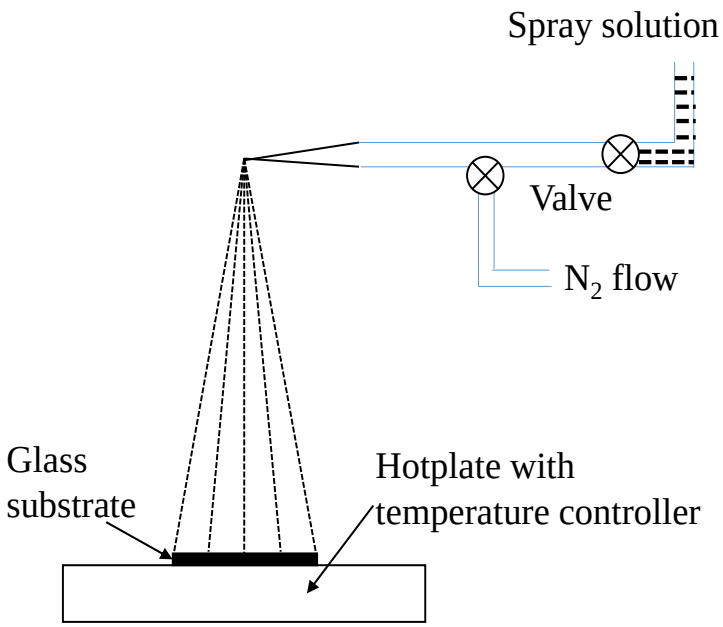

Figure 2.1. *Simple diagram of Spray Pyrolysis system [1].*

Er^{3+}-doped Y_2O_3 was synthesised through a conventional spray pyrolysis technique, which is an inexpensive, convenient and widely used technique for film deposition [1]. The whole system is very simple, as illustrated in figure 2.1 above. It includes a spraying system as well as a hotplate with temperature controller. The vertical distance between the spray gun and the hotplate surface is around 40 cm, which is a suitable distance to get fine solution drops. Typically, a mixture of

$Y(NO_3)_3 \cdot 6H_2O$ and $Er(NO_3)_3 \cdot 6H_2O$ was dissolved in 50 ml de-ionised water. The solution was sprayed, using a conventional spray gun, using N_2 gas onto a piece of cleaned Corning glass, which was pre-heated to 450 °C on the hotplate surface, creating a uniformly distributed white powder film of Er^{3+}-doped Y_2O_3. The specific precursor concentration for making the series of Er^{3+}-doped Y_2O_3 is given in table 2.1 below. The spraying rate was controlled at 20 ml/min by adjusting the N_2 gas pressure to 4 mbar. During the spraying process, the spraying time was 10 seconds followed by a minute break in order to make good quality Y_2O_3 [2]. The pause in the spraying is necessary to stop the spraying from cooling the glass substrate. The hotplate surface temperature maintained 450 °C during the whole spraying process. And the final yield of the Y_2O_3 is around 20%.

Table 2.1. *Precursor solution concentrations for spray pyrolysis.*

Doping concentration	$Y(NO_3)_3 \cdot 6H_2O$	$Er(NO_3)_3 \cdot 6H_2O$
0.2%	1 g/50 ml	0.0024 g/ 50 ml
0.5%	1 g/50 ml	0.006 g/ 50 ml
1%	1 g/50 ml	0.012 g/ 50 ml
2%	1 g/50 ml	0.024 g/ 50 ml
5%	1 g/50 ml	0.06 g/ 50 ml
10%	1 g/50 ml	0.12 g/ 50 ml

After the spraying process, the white film powder was removed and annealed under different temperatures (500 °C to 1000 °C) and time periods (2 hours to 24 hours)

in the ambient air. The details of the annealing conditions are described in chapter 3. All samples annealed at different temperatures were measured in order to get an idea of the optimum annealing condition.

2.3. Synthesis of HL ligand capped sub 10 nm 10% Yb^{3+}-doped $NaYF_4$ nanoparticles

2.3.1. Synthesis of $RE(CF_3COO)_3$

$Y(CF_3COO)_3$ and $Yb(CF_3COO)_3$ are the raw materials for producing Yb^{3+}-doped $NaYF_4$ nanoparticles in this experiment. They were prepared according to method reported in the literature [3]. In detail, 2 mmol Y_2O_3/ Yb_2O_3 were dissolved in a solvent containing 10 ml trifluoroacetic acid (TFA) and 20 ml deionised water. The reaction was refluxed under 80 °C stirring for 24 hours until forming a completely transparent solution. The resultant solution was then evaporated in a rotary evaporator for 1 hour at 90 °C to get the dried $Y(CF_3COO)_3$/ $Yb(CF_3COO)_3$ white powder. Y_2O_3, Yb_2O_3 and trifluoroacetic acid (TFA) precursors were all purchased from Sigma-Aldrich without any further purification.

2.3.2. Synthesis of HL ligand capped 10% Yb^{3+}-doped $NaYF_4$ nanoparticles

The synthesis of sub 10 nm 10% Yb^{3+}-doped $NaYF_4$ nanoparticles was done according to a modified literature-based method [4]. The detailed synthesis procedure can be described as follows. Firstly, 0.9 mmol $Y(CF_3COO)_3$, 0.1 mmol $Yb(CF_3COO)_3$ and 2 mmol $Na(CF_3COO)$ together with 4 ml oleic acid, 4 ml

oleyamine and 8 ml 1-octadecene were added to a dried round bottom flask and well mixed. Secondly, the uniformly mixed product was heated under vacuum (10^{-2} mbar) at 130 °C for 45 minutes to form a transparent yellowish solution. Then the flask was flushed with N_2 slowly for 5 minutes and then in order to balance the inner side pressure with the ambient air, a syringe needle was added to the top of the flask. In the meantime, a salt bath (0.5 kg $NaNO_3$ together with 0.5 kg KNO_3) was heated to 290 °C by a temperature controlled hotplate. After that, the reaction flask was heated in the salt bath under stirring for 40 minutes and the temperature of the reaction solution was set to 280 °C with a temperature feedback monitor to the hotplate. During the whole process, slow N_2 flow was used as a protective atmosphere. The general experimental system setup is shown in figure 2.2 below. 1-Octadecene (ODE; technical grade, 90%), oleic acid (OA; technical grade, 90%), Oleyamine (technical grade, 70%) and $Na(CF_3COO)$ were all purchased from Sigma-Aldrich without further purification.

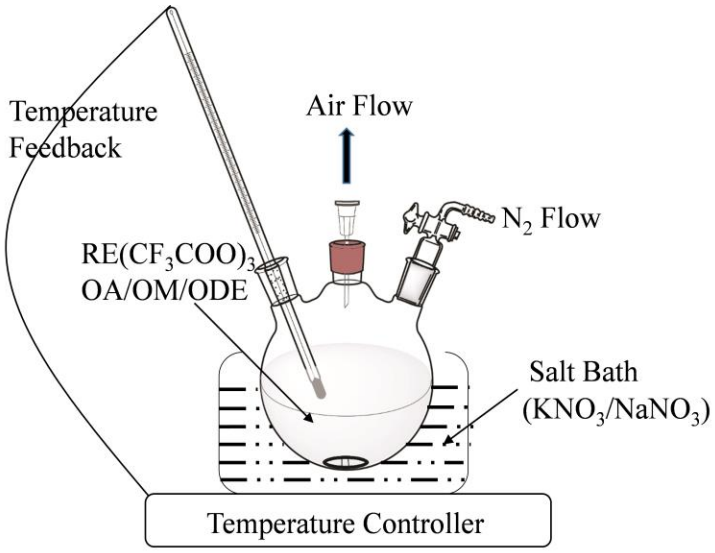

Figure 2.2. *Experimental setup for Yb^{3+}-doped $NaYF_4$ nanoparticles.*

When the reaction was finished, the solution was cooled under N_2 flow to minimise the effect of ambient air. The final products were isolated by adding ethanol and using centrifugation. The centrifugation speed was set to 3800 r/min. After being washed with ethanol and centrifuged two more times, the nanoparticles were dispersed into chloroform solvent.

1,2,3,4,5,6,7-heptafluoro-8-hydroxyanthracene-9,10-dione (HL) ligand capped sub 10 nm Yb^{3+}-doped $NaYF_4$ nanoparticle was synthesised through a simple chemical reaction. Firstly, 10 mg HL ligand was dissolved in 50 ml of chloroform to form a uniform light yellowish solvent. Then, 1 ml HL ligand solution was added to a 0.5 ml Yb^{3+}-doped $NaYF_4$ nanoparticle dispersed chloroform solution in which the nanoparticle concentration is 10 mg/ ml. Immediately, the colour of the mixed solution changed from yellowish to pink. For a comparison, dilution experiments and different ligand to nanoparticle ratios were tried, as described in chapter 4. The

chemical molecular of HL ligand is given in figure 2.3 below. Synthesis and characteristics of HL ligand were fully described in Y. Peng's paper [5].

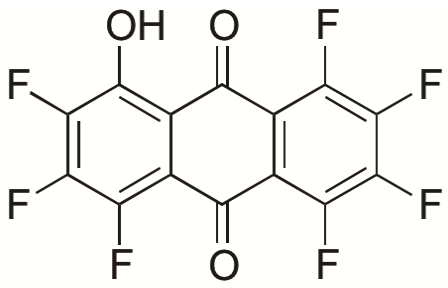

Figure 2.3. *Chemical molecular of HL ligand.*

2.4. Synthesis of $Yb(F\text{-}TPIP)_3$ and $Zn(F\text{-}BTZ)_2$ co-evaporated film

2.4.1. Synthesis of $Yb(F\text{-}TPIP)_3$ and $Zn(F\text{-}BTZ)_2$

The $Yb(F\text{-}TPIP)_3$ was synthesised through a chemical reaction between the HF-TPIP ligand and $YbCl_3{\cdot}6H_2O$ (99.98%). The HF-TPIP ligand was supplied by Dr. Z. Li from the School of Biological and Chemical Science, Queen Mary University of London, and the $YbCl_3{\cdot}6H_2O$ was purchased from Sigma-Aldrich without further purification. Typically, 1 g HF-TPIP ligand and 167 mg $YbCl_3{\cdot}6H_2O$ (HF-TPIP : $YbCl_3{\cdot}6H_2O$ = 3 : 1) were dissolved into 10 ml and 1 ml boiling ethanol solution under stirring to form two separate transparent solutions. Then, the $YbCl_3{\cdot}6H_2O$ solution was slowly added to the HF-TPIP ligand solution using a pipette. A large amount of white precipitate was produced immediately. The mixture was refluxed under boiling ethanol solvent for an hour. And then, once the precipitate had cooled down to room temperature under ambient air, it was isolated by centrifugation at a

rate of 4000 r/min and washed with methanol one more time. The final product was dried under vacuum (10^{-2} mabr) at a temperature of 150 °C for 24 hours. The final chemical yield was as high as 95%.

Even dried under vacuum for 24 hours, the material was still not 'dry' enough, as the measured 980 nm emission lifetime was low compared to the calculated ytterbium ions' intrinsic lifetime (1.31 ms [6]). This is discussed in detail in chapter 5. Thus, sublimation (purification) is a crucial step in our strategy to get rid of the potential impurities and molecules, such as unreacted ligand, ethanol, methanol or water, which can act as trapping centres, for making moisture free $Yb(F\text{-}TPIP)_3$ material. After sublimation, the 980 nm emission lifetime of the $Yb(F\text{-}TPIP)_3$ can be increased up to 1 ms, reaching 76% quantum yield. The $Yb(F\text{-}TPIP)_3$ was purified by using train sublimation in a glass tube under vacuum, as shown in figure 2.4 below.

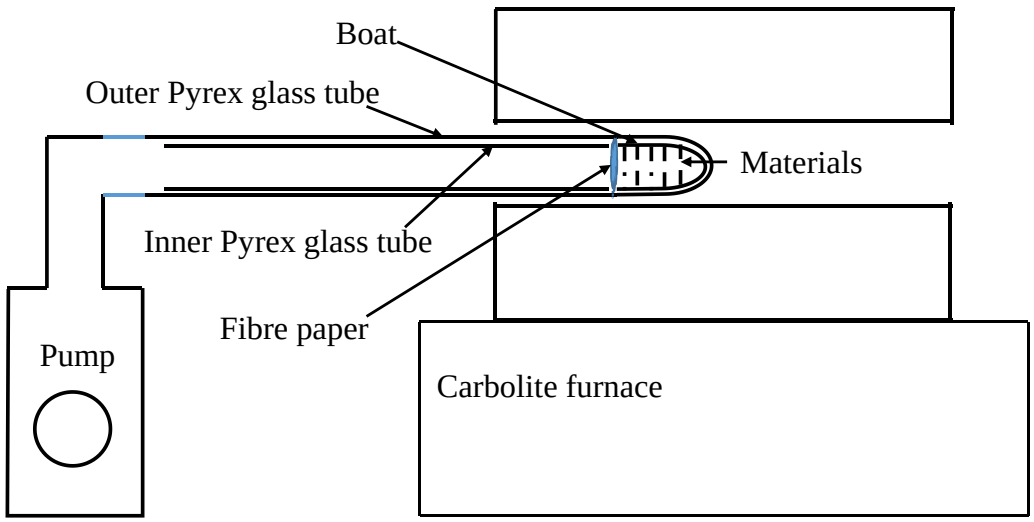

Figure 2.4. *Experimental setup for the sublimation of $Yb(F\text{-}TPIP)_3$ and $Zn(F\text{-}BTZ)_2$.*

The whole purification system is simply composed of a purification column, a Carbolite furnace and a pump. The purification column includes a glass boat and a set of outer and inner Pyrex glass tubes. Before the sublimation experiment, the boat and Pyrex glass tubes were cleaned using the standard cleaning method [7]. For the sublimation, typically, 1 g dried $Yb(F\text{-}TPIP)_3$ material was placed inside the glass boat and a piece of fibre paper was placed on top of the boat, which is used to stop the powder spilling out of the end. The glass boat filled with materials, together with the inner Pyrex tube, were put into the outer glass tube. The inner Pyrex glass tube was used to collect the pure sublimated material. The outer Pyrex glass tube was used as vacuum housing for the purification column. The closed end of the purification column was inserted into the centre of the Carbolite furnace and the open end was connected to a pump system containing a Turbotronik NT 10 turbo pump and a Trivac rotary pump. The vacuum of the system was below 10^{-6} mbar during the whole purification process.

In the first stage of purification, the $Yb(F\text{-}TPIP)_3$ material was heated to 120 °C at a relatively fast rate of around 5 °C/min when the vacuum of the purification column was below 10^{-6} mbar. Then, in order to get rid of the potential impurity molecules, as mentioned above, the system was left at the same temperature for 10 hours for out gassing. Thereafter, the temperature was increased by 20 °C every 3 hours until it reached 270 °C, which is the critical temperature for $Yb(F\text{-}TPIP)_3$ sublimation. Finally, the system was then left for several days for a complete sublimation. During this process, the temperature could be increased 10 to 20 °C according to the evaporation rate. When the sublimation was completely finished, there was a small

quantity of black powder (impurities) left in the boat, and the pure sublimated Yb(F-TPIP)$_3$ material was uniformly distributed around the inner Pyrex glass tube. After the sublimation process, the pure Yb(F-TPIP)$_3$ material was moved and kept under vacuum before film deposition.

Zn(F-BTZ)$_2$ was again supplied by Dr. Z. Li. The synthesis, physical and optical properties have been studied in the previous literature [8]. The chemical molecular is given in figure 2.5. And the sublimation of Zn(F-BTZ)$_2$ is also a crucial step for the same reason that the existing chemical molecules (impurities) can be trapping centres. The sublimation process of Zn(F-BTZ)$_2$ is similar to that described above for the Yb(F-TPIP)$_3$ material, except that the critical temperature of Zn(F-BTZ)$_2$ sublimation is 240 °C.

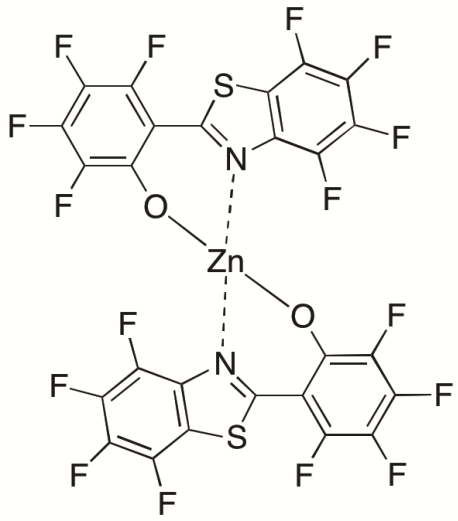

Figure 2.5. *Chemical molecular of Zn(F-BTZ)$_2$.*

2.4.2. Co-evaporation of $Yb(F\text{-}TPIP)_3$ and $Zn(F\text{-}BTZ)_2$

Before the co-evaporation of $Yb(F\text{-}TPIP)_3$ and $Zn(F\text{-}BTZ)_2$, these two materials were transferred from the vacuum box into two organic crucibles separately inside the evaporation system, as illustrated in figure 2.6 below. And 6 aluminium pellets (0.5 g) were added to the metal crucibles in order to form a 100 nm thick aluminium protective layer on top of the deposited organic film. It has to be noted here, even small amounts of impurities, such as water, inside the bulk materials could have a big effect in our lifetime measurement experiments. So, all the organic and metal materials have to be baked for at least one hour, at a temperature of 100 °C under a vacuum of 10^{-6} mbar, for out gassing.

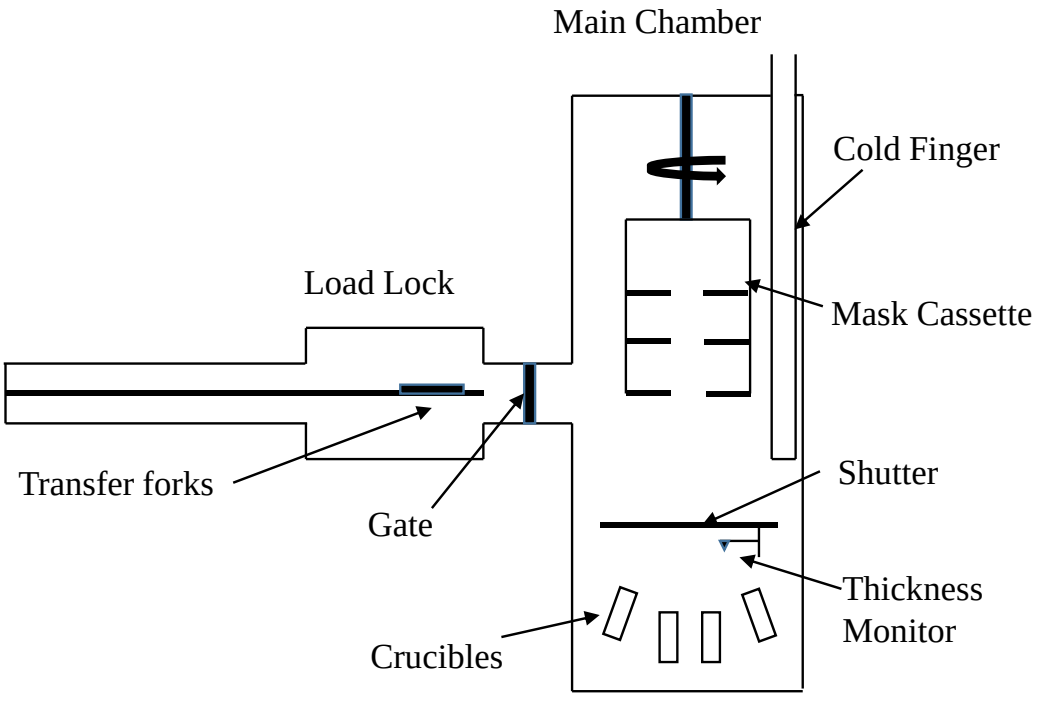

Figure 2.6. *Diagram of the co-evaporation system.*

The co-evaporation system includes two vacuum chambers, one is called the main chamber and the other is called the load lock, and it is used to transfer the substrate holder into the main chamber through a transfer fork. Both the load lock and main chamber are connected to a scroll pump and a turbo-molecular pump, thus the vacuum can normally go down to 10^{-6} mbar.

In a typical co-evaporation process, a piece of cleaned 2 cm^2 glass substrate was pre-loaded onto the transfer fork inside the load lock. Once the vacuum of the load lock was down to 10^{-5} mbar, the gate valve could be opened, allowing the substrate to be transferred onto the mask cassette in the main chamber. The main chamber is connected with the cold finger, which acts to freeze H_2O and hydrocarbons to the surface by adding liquid N_2. By doing this, the vacuum of the main chamber can go down to 5×10^{-7} mbar to minimise the amount of water or other organic impurity molecules. In order to see the effect of the cold finger, a residual gas analyser (RGA) is connected to the main chamber. The results are discussed in chapter 5. As water molecules play a vital important role as the quenching traps, as discussed in chapter 1, all the $Yb(F\text{-}TPIP)_3$ and $Zn(F\text{-}BTZ)_2$ co-evaporation processes were done under this 5×10^{-7} mbar vacuum condition in order to maximise the lifetime of Yb^{3+} ions.

During the deposition process, $Zn(F\text{-}BTZ)_2$ and the $Yb(F\text{-}TPIP)_3$ materials were heated slowly to a temperature of 140 °C and 170 °C respectively at the same time by adjusting the power supplier. At this critical temperature, the deposition rate of both the materials was 0.1 Å/s. After that, the standard deposition rate was adjusted

to be 1 Å/s (the deposition rate can be adjusted according to the required doping ratio). Then, the shutter was open and the deposition process began. The deposition film thickness was monitored by a quartz crystal monitor. In order to calibrate the deposition rate, the deposited film thickness was double confirmed with Dektak. After calibration, the deposited film thickness has an averaged experimental accuracy of 10 % compared to the thickness measured by Dektak.

After the deposition of the co-doped $Zn(F\text{-}BTZ)_2$ and the $Yb(F\text{-}TPIP)_3$ film, an extra layer of 100 nm aluminium film needed to be deposited onto the top of the organic film to prevent possible degradation in the ambient air. During this process, the vacuum of the main chamber was normally around 10^{-6} mbar due to the large amount of heat released by the aluminium evaporation. Finally, the film was kept in the load-lock under vacuum until it was taken for optical measurements.

2.5. Material characterisation techniques

2.5.1. X-ray diffraction

X-ray diffraction (XRD) is a commonly used technique for material structure characterisation. The diffraction peak is unique for each crystalline material according to the Bragg Law [9] as the constructive interference of the radiation occurs when the path phase difference is an integral number n of wavelength λ, so that:

$$2d \sin\theta = n\lambda \tag{2.1}$$

where d is the space of crystal planes and θ is the angle of diffraction peaks. The relative intensity of the different orders of diffraction is determined by the lattice basis according to the structure factor $F(hkl)$ [10]:

$$F(hkl) = \sum_{n=1}^{N} f_n exp[2\pi i(hx_n + ky_n + lz_n)] \quad (2.2)$$

Where hkl are the Miller indices, f_n is the atomic scattering factor, and x_n, y_n, z_n are the coordinates of the n^{th} atom in the unit cell containing N atoms.

In my experiments, the XRD patterns were recorded using Cu Kα radiation (λ = 1.5418 Å). And the collected XRD data was compared with the known crystallographic information framework file.

2.5.2. Energy dispersive X-ray spectroscopy

As demonstrated in chapter 3, the doping concentration effect is discussed in detail. Therefore, it is necessary to compare the real doping concentration with the chemically prepared precursor doping concentrations. Energy-dispersive X-ray spectroscopy (EDS) is a commonly used elemental analysis technique, which is based on the principle that each atom has a unique set of peaks on its X-ray emission spectrum [11]. In the EDS experiment, a high energy beam of electron (20 kV) was used. And as the Er^{3+}-doped Y_2O_3 is a poor conductor, a thin carbon film was deposited under vacuum onto the top of the Y_2O_3 in order to get the emission from the specimen. The doping ratio data was calculated for both the spot and large sample areas.

2.5.3. Transmission electron microscopy

Transmission electron microscopy (TEM) is a microscopy technique used to form an image from interactions of electrons passing through the specimen. The image is then magnified and focused onto a CCD camera.

Preparation of the sample is as follows: chloroform solution containing Yb^{3+}-doped $NaYF_4$ nanoparticles was diluted to a concentration of 0.1 mg/ml. And a drop of this solution was coated onto a 200-mesh carbon copper grid using a pipette. When the carbon copper was dried, the sample was moved in to the FEI Tecnai G2 T20 machine operated at 200 KeV. The images were randomly selected from TEM micrographs.

2.6. Optical instruments and set up

Fluorescence measurements can be generally classified into two kinds of measurements: steady-state measurements and time-resolved measurements. Steady-state measurements is a relatively easy way, and is performed with a continuous beam of light, with the intensity of the luminescence measured as a function of wavelength λ. [12] While time-resolved measurements are mainly used for measuring the intensity decays as a function of time from nano-second to tens of second region, it requires rather complicated and expensive instruments such as high speed detection systems (the response time should be in the nano-second or smaller region). However, the precise shape of the luminescence intensity decay curve is very important as it contains all the information of rise time, radiative and

non-radiative lifetimes by fitting the rise and decay intensity curve parts, which is fundamental information for studying the energy transfer processes as well as the quantum yield.

The major part of the optical measurements in this thesis is about the time-resolved spectroscopic measurements due to the benefits discussed above. For the time-resolved spectroscopic measurements, a pulsed or modulated excitation light source is used and the luminescence is monitored as a function of time following the pulse emission. Tunable optical parametric oscillators (OPO), electrically modulated CW lasers (375 nm, 405 nm and 980 nm CW lasers), as well as the xenon lamp, were used as excitation sources for time-resolved spectroscopic measurements depending on the experimental requirements. The reason for using the OPO or CW lasers is that they can be precisely modulated and they can provide enough power density for luminescence measurements. For the xenon lamp, it has a full range of light (350 nm to 1000 nm was used in the experiment) and is useful for low power density measurements. A Hamamatsu R5509-72 nitrogen-cooled photomultiplier tube (PMT), which has a short response time (less than 1 ns), is suitable and used for transient luminescence detection together with an oscilloscope.

A typical experimental set up for the time-resolved spectroscopy measurements is shown in figure 2.7 below. Figure 2.7 demonstrates a typical time-resolved spectroscopy lifetime measurements set up with OPO excitations. The OPO excitation light was shined onto the sample of interest. And the directly reflected excitation light (black line) from the sample should be removed by turning the angle of the sample holder. Only the scattered light (blue line) emitted from the sample

was collected through the monochromator and detected by PMT. An oscilloscope, which is connected to a computer, is used to record the emission intensity decay curves as a function of time. It should be mentioned that suitable long-pass (for Down-conversion measurements) or short-pass (for Up-conversion measurements) filters should be used in order to minimise the background during all measurements.

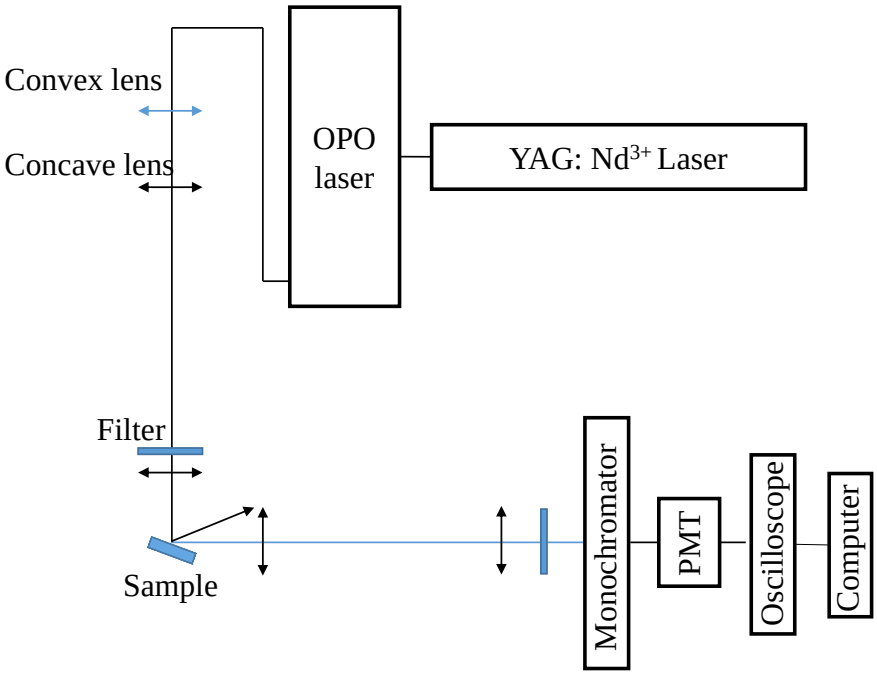

Figure 2.7. *Schematic of the standard time-resolved spectroscopy set up.*

The OPO excitation source can also be replaced with the precisely electrically modulated CW lasers or Xenon lamp, for lifetime measurements or excitation measurements respectively. In addition, the oscilloscope can be replaced with a lock-in amplifier for recording the emission or excitation spectra. The main optical instruments, including the OPO, solid state lasers, Apex Arc lamp, spectrometer,

PMT and oscilloscope, and spectrophotometer are described in detail in the subsections below.

2.6.1. Tunable optical parametric oscillators

The tunable optical parametric oscillator (OPO) has a fast pulse (~ 7 ns, 10 Hz), which is pumped by a third harmonic ($\lambda = 355$ nm) of Q-switched YAG: Nd^{3+} laser, and the excitation wavelength is tunable from 410 nm to 1700 nm by converting the YAG: Nd^{3+} laser frequency into two output frequencies:

$$\omega_p = \omega_s + \omega_i \tag{2.3}$$

where ω_p is the frequency of the input YAG: Nd^{3+} laser, ω_s is the frequency of the output signal and ω_i is the frequency of the output idler.

2.6.2. Apex Arc lamp

The Apex Arc lamp, which has a stable Xenon lamp source of 150 W white light output, was used in our excitation spectra measurements for the ligand capped $NaYF_4$ nano-particles as well as $Yb(F\text{-}TPIP)_3$ co-evaporated with $Zn(F\text{-}BTZ)_2$ thin films. The Xenon lamp is a gas discharged lamp, which generates light by passing electricity through ionised xenon gas at high pressure. As far as the experimental set up, the light from the Xenon lamp was passed through a spectrometer before being used as the excitation source. Grating of the spectrometer is 1200 lines/mm.

And the maximum wavelength region used was from 350 nm to 1000 nm in all experiments.

2.6.3. Solid-state lasers: 375 nm, 405 nm and 978 nm

The 375 nm and 405 nm continuous wavelength (CW) lasers used in the optical experiments were Stradus^{TM} diode lasers. The maximum output power of the 378 nm and 405 nm CW lasers is 16 mW and 100 mW respectively. The output power can be simply adjusted from 1 mW to the maximum using the user interface software installed on the computer. And of course, the output power can be adjusted down to μW region using the ND filters as well.

A MLR-III-978 nm infrared diode laser was also used for the up- and down-conversion measurements. The maximum output power is 500 mW and the output power can be adjusted through the power controller.

All these three lasers were modulated with a square wave within the frequency range from 10 Hz to ~200 Hz using a function generator, which has a relatively fast rise and fall time (25 ns).

2.6.4. Spectrometer

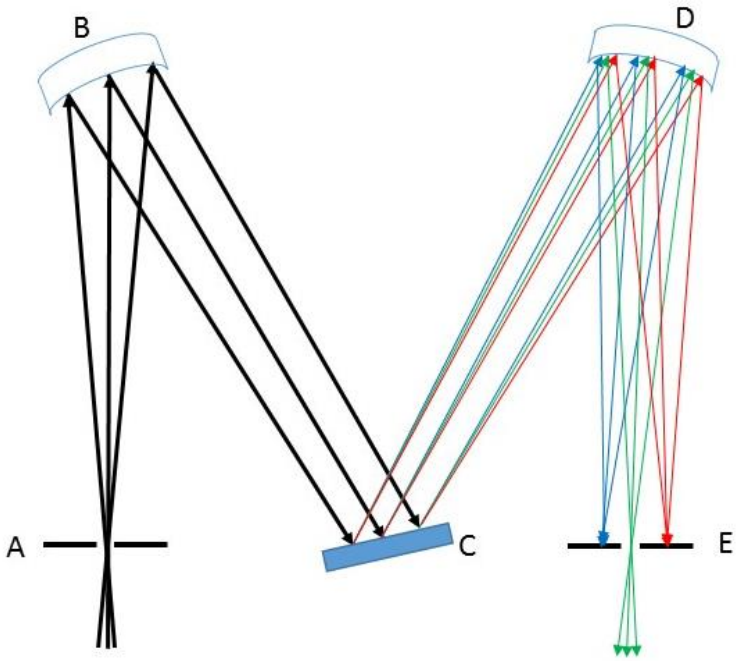

Figure 2.8. *Schematic of the spectrometer.*

A spectrometer is used to disperse the luminescence. It consists of an entrance slit (A), a collimator (B), the diffraction grating (C), focusing mirror (D) and an exit slit (E), as illustrated in figure 2.8 above. Luminescence was focused on the collimator (B) through the entrance slit (A) and then was reflected onto the diffraction grating (C) in parallel. After the diffraction, the luminescence was refocused by the collimator (D) to the exit slit (E). Due to the diffraction, the luminescence of different wavelengths was separated. Thus, the intensity of the luminescence spectra can be adjusted by rotating the grating.

The Jobin Yvon Horiba Triax 550 spectrometer was used in the emission and time-resolved spectroscopy measurements. There were two commonly used gratings during the measurements. One grating is 600 lines per mm, which is blazed at 1 μm wavelength. This is typically used for IR region measurements. The other grating is 1200 lines per mm, which is blazed at 550 nm wavelength. This is used for the UV/Visible regions instead.

2.6.5. Photomultiplier Tubes

A photomultiplier is used to detect the dispersed luminescence in the ultra violet, visible and near infrared regions by multiplying the electrical signals. It contains a photocathode, several dynodes and an anode inside a vacuum glass envelope. When the photons strike the photocathode, electrons are generated as a sequence of photoelectric effect and then accelerated by the electric fields between the dynodes until they reach the anode.

The typical photomultiplier used in my experiment is a Hamamatsu R5509-72 nitrogen cooled detector. The working temperature is -80 °C and the detecting signal range is from 350 to 1650 nm wavelength. The output resistance was set to either 50Ω or 1KΩ depending on the measuring conditions. It should be mentioned, another Hamamatsu 9113B PMT was used for spectral measurements of the visible light (300-800 nm). The output resistance is 10MΩ.

2.6.6. Oscilloscope

The oscilloscope, shown in the figure 2.7, is for recording the time-resolved spectroscopy. By using the "Trigger" function, the luminescent signal can be observed and recorded onto the screen. The typical oscilloscope used is the LeCroy Waverunner LT372 with a 500 MHz maximum frequency.

2.6.7. Lock-in amplifier

The multiplied electrical signal from the photomultiplier is measured by the lock-in amplifier. A lock-in amplifier relies on the orthogonality of sinusoidal functions, therefore, it can recover the signal from an extremely noisy background and enhance the resolution of a clean signal with a known carrier wave frequency. In essence, a lock-in amplifier takes the input signal, multiplies it by the external reference signal, and integrates it over a few seconds. The resulting signal is the DC signal, where any signal that is not the same frequency as the reference signal will be decreased to zero by the low pass filter. This is also called the phase-sensitive detection (PSD) technique. A typical lock-in amplifier diagram is shown in figure 2.9. There are two inputs: signal and reference, and there is a low pass filter after the output from the PSD.

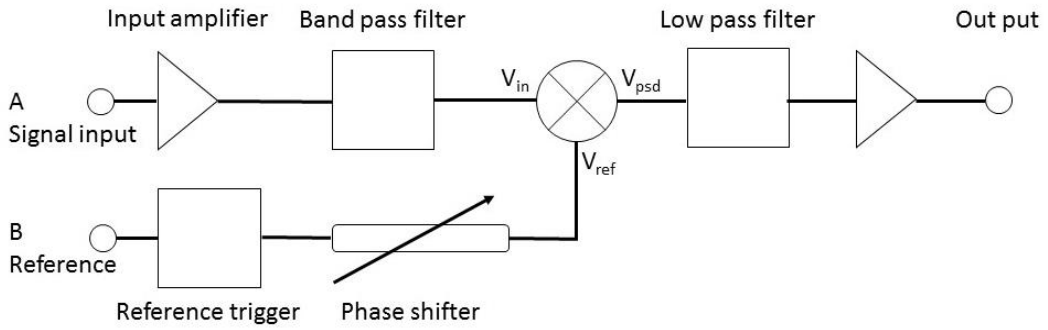

Figure 2.9. *Diagram of a typical lock-in amplifier.*

Specifically, if the input signal is a sinusoidal function $V_{sig}\sin(\omega_{sig}t+\theta_{sig})$ modulated by an external reference signal $V_{ref}\sin(\omega_{ref}t+\theta_{ref})$, the output of the PSD is the product of input and reference signals:

$$v_{sig}v_{ref}\sin(\omega_{sig}t+\theta_{sig})\sin(\omega_{ref}t+\theta_{ref})$$
$$=\frac{1}{2}v_{sig}v_{ref}\cos[(\omega_{sig}-\omega_{ref})t+(\theta_{sig}-\theta_{ref})]-\frac{1}{2}v_{sig}v_{ref}\cos[(\omega_{sig}+\omega_{ref})t+(\theta_{sig}+\theta_{ref})] \quad (2.4)$$

where V_{sig} and V_{ref} are the amplitudes, ω_{sig} and ω_{ref} are the frequencies, θ_{sig} and θ_{ref} are the phases of the input and reference signals respectively. As can be seen, when ω_{sig} is equal to ω_{ref}, the output of the PSD is an AC signal $\frac{1}{2}V_{sig}V_{ref}\cos(\theta_{sig}-\theta_{ref})$ plus a high frequency signal $\frac{1}{2}V_{sig}V_{ref}\cos[(\omega_{sig}+\omega_{sig})t+(\theta_{sig}+\theta_{ref})]$. The high frequency signal will be filtered out by the low pass filter, so only the DC signal can pass through.

2.6.8. U-3000 spectrophotometer

The Hitachi U-3000 spectrophotometer, which is a quantitative measurement of transmission of a material as a function of wavelength (250 nm to 800 nm), was used to do the absorption spectroscopy measurement. It is a single beam spectrophotometer, which measures the relative intensity before and after the sample.

2.7. Reference

[1] E. Shanthi, V. Dutta, A. Banerjee, K. L. Chopra, Electrical and optical properties of undoped and antimony-doped tin oxide films, *Journal of Applied Physics*, **51** (1980) 6243-6251.

[2] G. Adamopoulos, A. Bashir, W. P. Gillin, S. Georgakopoulos, M. Shkunov, M. A. Baklar, N. Stingelin, D. D. C. Bradley, T. D. Anthopoulos, Structural and electrical characterization of ZnO films grown by spray pyrolysis and their application in thin-film transistors, *Advanced Functional Materials*, **21** (2011) 525-531.

[3] J. E. Roberts, Lanthanum and neodymium salts of trifluoroacetic acid, *Journal of the American Chemical Society*, **83** (1961) 1087-1088.

[4] X. Ye, J. E. Collins, Y. Kang, J. Chen, D. T. N. Chen, A. G. Yodh, C. B. Murray, Morphologically controlled synthesis of colloidal upconversion nanophosphors and their shape-directed self-assembly, *Proceedings of the National Academy of Sciencesof the United Satets of America*, **107** (2010) 22430-22435.

[5] Y. Peng, H. Ye, Z. Li, M. Motevalli, I. Hernandez, W. P. Gillin, P. B. Wyatt, Visible-range sensitization of Er^{3+}-based infrared emission from perfluorinated 2-acylphenoxide complexes, *The Journal of Physical Chemistry Letters*, **5** (2014) 1560-1563.

[6] A. Aebischer, F. Gumy, J. -C. G. Bünzli, Intrinsic quantum yields and radiative lifetimes of lanthanide tris (dipicolinates), *Physical Chemistry Chemical Physics*, **11** (2009) 1346-1353.

[7] S. Zhang, Modelling of organic magnetoresitance in aluminium tris light emitting diodes, School of Physics and Astronomy, Queen Mary Univerity of London, London, 2011.

[8] Z. Li, A. Dellali, J. Malik, M. Motevalli, R. M. Nix, T. Olukoya, Y. Peng, H. Ye, W. P. Gillin, I. Hernández, P. B. Wyatt, Luminescent zinc (II) complexes of fluorinated benzothiazol-2-yl substituted phenoxide and enolate ligands, *Inorganic Chemistry*, **52** (2013) 1379-1387.

[9] C. Kittel, Introduction to solid state physics, John Wiley & Sons, Inc, USA, 2005.

[10] I. Etchart, Metal oxides for efficient infrared to visible upconversion, Materials Science and Metallurgy, University of Cambridge, Cambridge, 2010.

[11] J. I. Goldstein, D. E. Newbury, P. Echlin, D. C. Joy, C. Fiori, E. Lifshin, Scanning electron microscopy and X-ray microanalysis. A text for biologists, materials scientists, and geologists, *Plenum Publishing Corporation*, 1981.

[12] J. R. Lakowicz, Principles of fluorescence spectroscopy, *Springer*, USA, 2006.

Chapter 3: Concentration dependence of the up- and down-conversion emission colour of Er^{3+}-doped Y_2O_3; a time-resolved spectroscopy analysis

3.1. Introduction

As discussed in chapter 1, one of the fundamental objectives of this thesis is to gain a basic understanding of the interactions between lanthanide ions. Er^{3+} is one of the lanthanide ions that have been investigated for the underlying physics and various potential applications [1]. Er^{3+}-doped up-conversion (UC) materials, which can convert the infrared light into visible luminescence via excited state absorption (ESA) or energy transfer (ET), can be used for applications ranging from biology to solar conversion. For example, the narrow visible emission excited by low energy can be employed in biomedicine [2], solid state laser [3] and illumination [4]. Especially, the materials can be employed in a functional phosphor layer to improve the efficiency of solar cells by means of converting infrared light, which cannot be absorbed by solar cell, into absorbable visible light [5, 6]. The commonly used host systems are halides [2, 4, 5, 7-14], glasses [15-17] and oxides [6, 18-32]. During all these research in the literature, β-$NaYF_4$ is one of the most studied host materials [2, 4, 5, 7-11, 13, 14] as it yields one of the highest UC efficiencies [33], which is due to the unique crystal structure and low phonon energy. However, it requires a complicated synthesis method to make pure (thermally stable) β-$NaYF_4$, which makes it less practical for industrial applications [26]. On the contrary, Y_2O_3 has an

excellent chemical stability [34] and the synthesis is simple. Furthermore, Y_2O_3 has a low phonon energy (430-550 cm^{-1}), which makes it a practical prototype UC material [32]. Based on all the above considerations, Er^{3+}-doped Y_2O_3 was chosen as our starting system.

Er^{3+}-doped Y_2O_3 systems have been previously investigated for potential UC applications [19-21, 31]. These studies were underpinned by a two-fold objective: to understand the UC mechanisms and the changes in light emission colour upon changes in the erbium doping concentration (1% to 10%) or excitation wavelengths (excited at 815 nm and 980 nm). Particularly, the UC emission colour (the ratio between the different emission bands) as a function of composition is a phenomenon of high interest, as it should allow the material to be used for multicolour applications. There are two main kinds of UC routes (ESA and ETU) for single Er^{3+}-doped systems (see chapter 1). The UC route (ESA or ETU) depends on the Er^{3+} doping concentrations. J. A. Capobianco *et al.* reported that the green ($^4S_{3/2} \rightarrow {}^4I_{15/2}$) to red ($^4F_{9/2} \rightarrow {}^4I_{15/2}$) ratio decreases via UC at an excitation wavelength of 815 nm with increasing erbium concentration in the Er^{3+}-doped Y_2O_3 system [20]. The change was explained by the occurrence of cross relaxation (CR) via: $[{}^4I_{9/2}, {}^4I_{11/2}] \rightarrow [{}^4I_{13/2}, {}^4F_{9/2}]$ (CR1 in figure 3.1 below). However, the difference of emission spectra under short excitation wavelength (488 nm) and UC pumping (815 nm) cannot be explained by this mechanism only. The same group postulated that the CR process: $[{}^4F_{7/2}, {}^4I_{11/2}] \rightarrow [{}^4F_{9/2}, {}^4F_{9/2}]$ (CR2 in figure 3.1 below) populates the red-emitting state by depopulating the green one with UC pumping (980 nm) causing a systematic difference of emission spectra under 488 nm and 980 nm

excitations [31]. However, this CR process happens under both 488 nm and 980 nm excitations, thus the theory is not good enough to explain the spectral differences. The current understanding therefore still involves an ambiguous combination of CR processes and UC routes. In order to differentiate the CR processes and UC routes, it is necessary to know the population and de-population dynamics under certain excitation wavelengths.

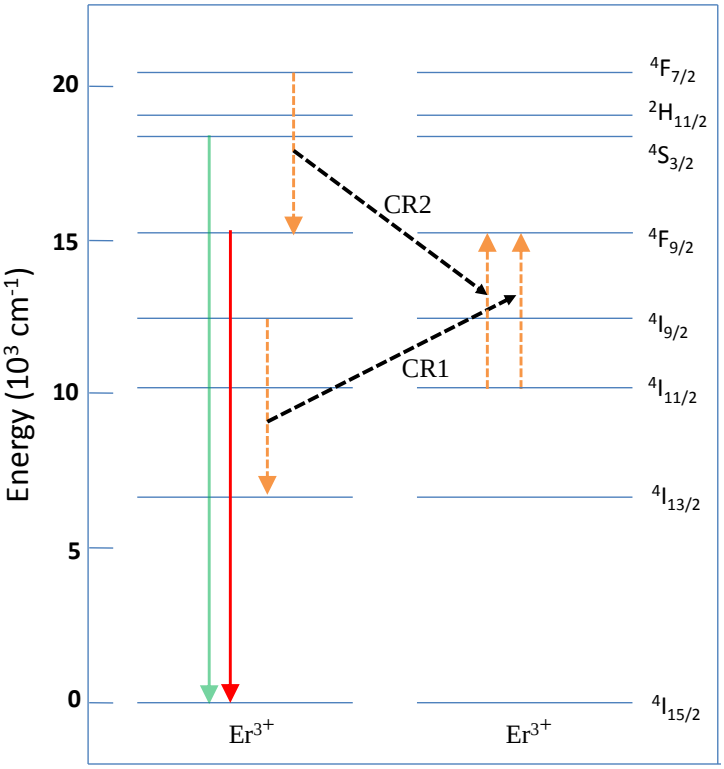

Figure 3.1. *Cross relaxation processes of* $[^4I_{9/2}, {}^4I_{11/2}] \rightarrow [^4I_{13/2}, {}^4F_{9/2}]$ *and* $[^4F_{7/2}, {}^4I_{11/2}] \rightarrow [^4F_{9/2}, {}^4F_{9/2}]$ *in single* Er^{3+}*-doped systems.*

It is also worth noting that despite the great activity and interest in co-doped systems with ytterbium as the sensitiser and erbium as the emitter, the green to red ratio changes observed with varying erbium and ytterbium concentrations are still the

subject of major revisions: there was no clear explanation given for the ratio change with doping concentration in Mai's paper [12]. Recently, R. B. Anderson *et al.* reported that the red emission is due to a three photon process in the Yb/Er co-doped β-$NaYF_4$ system under 943 nm excitation, involving CR within Er^{3+} ions from higher-lying $^4G_{11/2}$, $^2K_{15/2}$ states [13]. The need for accounting for all the processes and the existing non-definition of those that are important is in part due to the lack of dynamic data and the difficulty in modelling so many states and ions. We believe these incomplete models need further testing, clarification and refinement.

In order to fully understand the UC mechanism and emission colour change with doping concentrations, and give some fundamental information for Yb/Er co-doped systems, we have performed a study of the Er^{3+}-doped Y_2O_3 system using the time resolved spectroscopy method, which is used to understand the character of the emitting states by recording each emitting state's time decay profile. The time decay profile of the emitting states offers the possibility of quantifying not only the probability of radiative processes but, importantly, that for non-radiative processes such as CR, which are critical to determine the dynamical processes and colour properties of optical materials. Moreover, information can be obtained on the populating mechanisms by measuring the rise time. To the best of our knowledge, there has been no such systematic study of the $^4I_{11/2}$ and $^4I_{13/2}$ state lifetimes in Y_2O_3 under both 488 nm and 980 nm excitations, which are vital to understanding UC processes in this material and in co-doped systems. Therefore, we would expect our

work in the simple Er^{3+}-doped Y_2O_3 system to contribute to an understanding of more practical systems, such as the Yb/Er co-doped system.

3.2. Experimental and material characterisation

3.2.1. Synthesis of Er^{3+}-doped Y_2O_3 materials

Details of the synthesis of Er^{3+}-doped Y_2O_3 powders are given in chapter 2. As the Y_2O_3 powder was made with water solvent, there is a possibility that Y_2O_3 still contains some water molecules even under 450 °C high synthesis temperature. In order to reduce the water molecules, annealing at higher temperature was used. Given the fact that the near-infrared (NIR) luminescence lifetime of Er^{3+} is very sensitive to the O–H chemical bond, as discussed in chapter 1, lifetime measurement was chosen as a way to determine whether the material is water molecule free under a different annealing temperature and time. Lifetime measurements of $^4I_{13/2}$ (1535 nm), $^4I_{11/2}$ (980 nm), $^4F_{9/2}$ (660 nm) and $^4S_{3/2}$ (560 nm) states under 488 nm OPO excitation were done for the 5% Er^{3+}-doped Y_2O_3 powder sample. A systematic down-conversion (DC) lifetime study under different annealing temperatures and time is given in figure 3.2. It shows that 2 hours annealing at 1000 °C is the optimum annealing condition (longest lifetime), which was used in this work. It should be noted that the lifetime used in this work is based on the double exponential fitting of the decay curves. The details of the lifetime fitting is given in subsection 3.3.

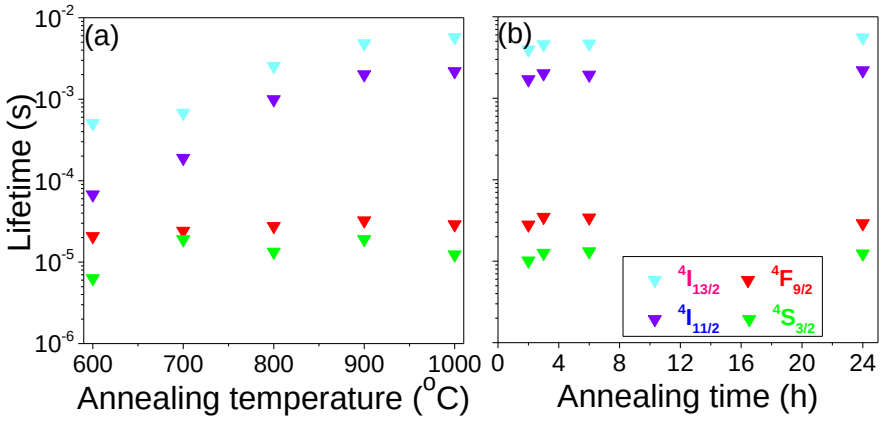

Figure 3.2 (a). *Measured DC lifetimes of $^4I_{13/2}$, $^4I_{11/2}$, $^4F_{9/2}$ and $^4S_{3/2}$ states of 5% Er^{3+}-doped Y_2O_3 annealed for 24 hours at different temperatures with 488 nm OPO laser;* ***(b).*** *Measured DC lifetimes of $^4I_{13/2}$, $^4I_{11/2}$, $^4F_{9/2}$ and $^4S_{3/2}$ states of 5% Er^{3+}-doped Y_2O_3 annealed at 1000 °C for different times with 488 nm OPO laser (power density is 3×10^6 Wcm^{-2}).*

3.2.2. Instrumentation

Powder X-ray diffraction (XRD) patterns of the dried Er^{3+}-doped Y_2O_3 were recorded using Cu Kα radiation (λ = 1.5418Å). The erbium doping concentration was confirmed by energy dispersive X-ray spectroscopy (EDX) at an accelerating voltage of 20 kV.

For the down-conversion (DC) lifetime and spectral measurements, a Continuum Panther optical parametric oscillator (OPO) was used to provide ~7 ns pulse with a typical power density of 3×10^6 Wcm^{-2} at a wavelength of 488 nm. Also, a 385 nm and 405 nm CW laser with a typical power density of 16 Wcm^{-2}, which were modulated by a digital pulse wave generator, were used to investigate the effect of pulse length and the excitation energy level. The fluorescence was dispersed in a

Triax 550 spectrometer (gratings: 1200 and 600 lines per mm) and detected by a Hamamatsu R5509-72 photomultiplier.

For the UC lifetime and spectra measurements, a 980 nm CW diode laser with a maximum power density of 50 Wcm^{-2} was used, which is modulated by a digital square wave generator at a frequency of 11 Hz. The excitation laser was removed from the fluorescence using a short pass filter (10SWF-950-B) that was dispersed and collected using the same system as for the DC measurements.

3.2.3. Structural characterisation

The synthesised Er^{3+}-doped Y_2O_3 is a pure single cubic phase [29]. The XRD data of all Er^{3+}-doped Y_2O_3 materials are shown in figure 3.3, which confirms the cubic structure of the Y_2O_3 material.

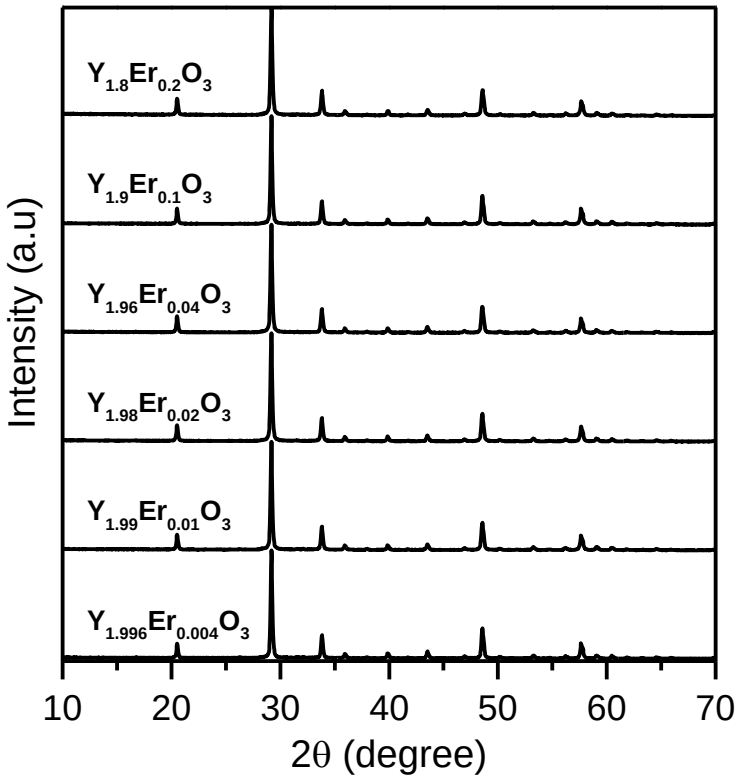

Figure 3.3. *Powder XRD patterns of Er^{3+}-doped Y_2O_3 with various doping concentrations (0.2% to 10%) after annealing at 1000 °C for 2 hours.*

EDX spectra were taken for three selected samples (0.2%, 5% and 10% Er^{3+}-doped Y_2O_3) and the concentrations of erbium and yttrium were measured to be those of the nominal values as shown in figure 3.4, below. EDX spectra is a measurement of the number and energy of electrons released by the specimen after the interaction with high energy electrons by an energy-dispersive spectrometer. The released energy of electrons is the difference in energy between two shells of the atomic structure, which is unique for a certain element. EDX spectra shows that the composition of the material is oxygen, erbium and yttrium, and the ratio of erbium to yttrium can be calculated afterwards (see figure 3.4 (b)).

(a)

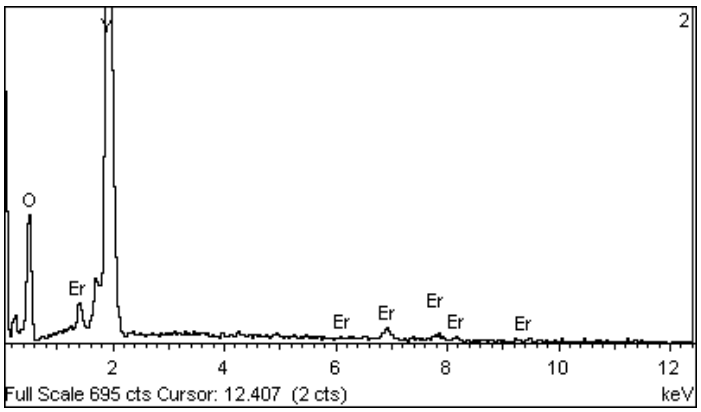

(b)

	0.2% Er^{3+}:Y_2O_3	5% Er^{3+}:Y_2O_3	10% Er^{3+}:Y_2O_3
Er/Y	0.243%	5.97%	9.94%

Figure 3.4 (a). *Energy dispersed X-ray spectroscopy of the 5% Er^{3+}-doped Y_2O_3;* ***(b).*** *Measured elemental ratio of Er/Y of the selected 0.2%, 5% and 10% Er^{3+}-doped Y_2O_3 samples.*

3.3. Lifetime difference between UC and DC processes

3.3.1. Lifetime measurements

As we have stated in the introduction, spectral information is not, by itself, sufficient to understand the difference between UC and DC processes, as it only provides a partial picture. In order to fully understand the occurring processes, it is necessary to obtain the details of the decay curves of all intervening states, showing how each state is populated and depopulated. To quantify the decay constants, all the decay curves, I(t), were fitted with a double exponential equation,

$$I(t) = A_0 + A_1 * \exp\left(-\frac{t}{\tau_1}\right) + A_2 * \exp\left(-\frac{t}{\tau_2}\right) \qquad 3.1$$

Where I(t) is the time decay intensity at the maximum of the emission band, A_0 is the background, A_1, A_2 are the exponential pre-factors and τ_1 and τ_2 are the fitted decay times. This model is usually employed to account for the decay of erbium ions in an inhomogeneous environment, for example where ions are either in the bulk or near the surface (see the example of Yb^{3+}-doped $NaYF_4$ nanoparticles in chapter 5) and undergoing different quenching or energy transfer routes, or when a population of the ions is close to the presence of impurities. Hence, it is widely phenomenologically employed without associated hypotheses on the nature of the parameters. The average decay time constant τ_{av} can be determined using [12],

$$\tau_{av} = \frac{A_1\tau_1{}^2 + A_2\tau_2{}^2}{A_1\tau_1 + A_2\tau_2} \qquad 3.2$$

When the decay curve is well fitted (and thus all processes are correctly phenomenologically accounted for), this is equivalent to taking a non-fitted average decay constant, calculated directly from the time dependence of the decaying intensity [35],

$$\tau_{av} = \frac{\int_0^\infty tI(t)dt}{\int_0^\infty I(t)dt} \qquad 3.3$$

3.3.2. Lifetime summary during UC and DC processes

Er^{3+}-doped Y_2O_3 powder yields a wide range of light emission, as shown in figure 3.5 below, with discrete bands ranging from the visible (~520 nm) to the infrared

(~1535 nm), following excitation at 488 nm at room temperature. In addition, continuous wavelength diode laser illumination at 980 nm is able to excite the visible bands (~520 nm and ~660 nm) through UC processes as shown in figure 3.6 below. The bands, as shown in figure 3.5 and 3.6 for 0.2% Er^{3+}-doped Y_2O_3, can be assigned to the corresponding emissions from the $^4S_{3/2}$, $^4F_{9/2}$, $^4I_{11/2}$ and $^4I_{13/2}$ states to the ground $^4I_{15/2}$ state of the Er^{3+} ion.

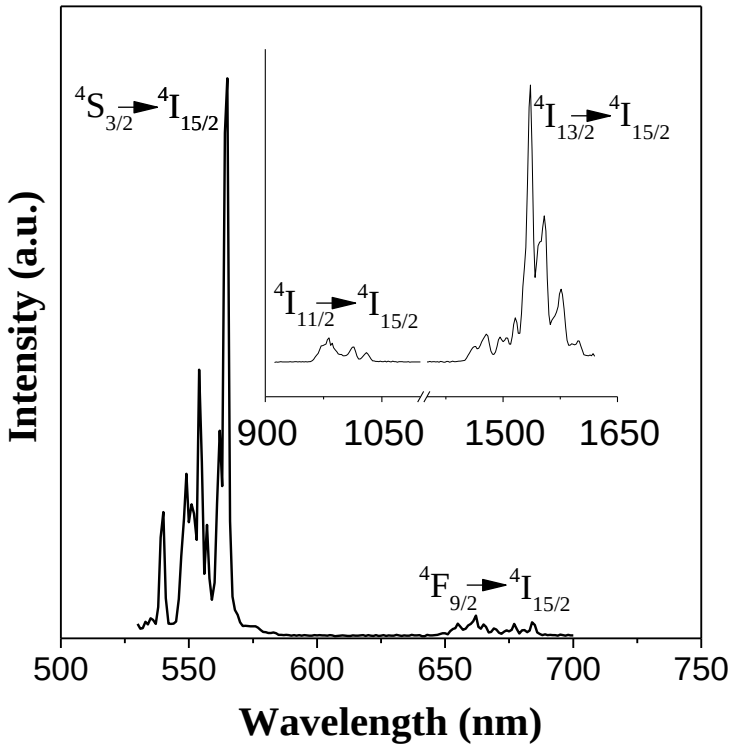

Figure 3.5. *Spectra of 0.2% Er^{3+}-doped Y_2O_3 under 488 nm OPO excitation.*

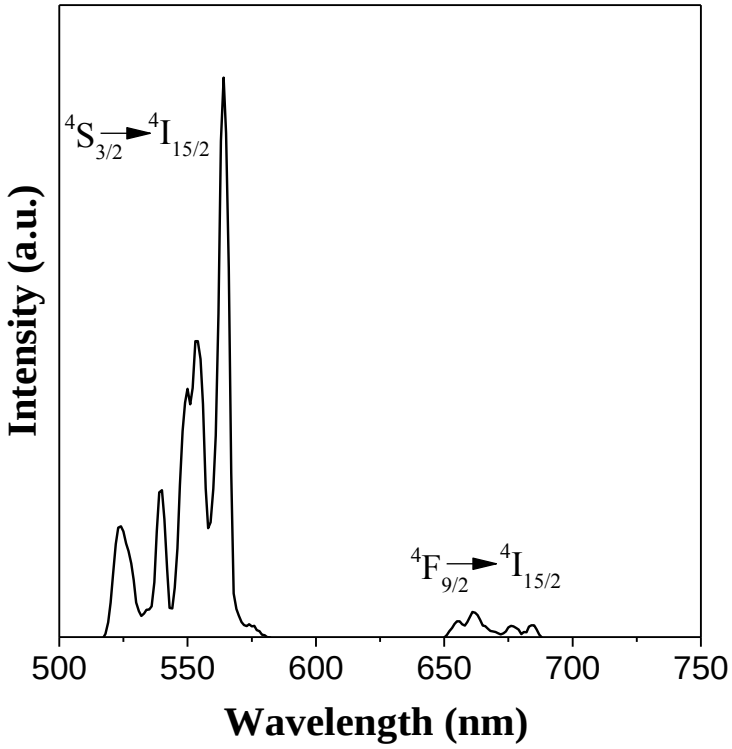

Figure 3.6. *Emission Spectrum of 0.2% Er^{3+}-doped Y_2O_3 under modulated 980 nm CW excitation.*

Figure 3.7 below shows the recorded intensity decay curves and corresponding fits of the $^4S_{3/2}$ (green), $^4F_{9/2}$ (red), $^4I_{11/2}$ (980 nm) and $^4I_{13/2}$ (1535 nm) states for the 0.2% Er^{3+}-doped Y_2O_3 sample under 488 nm OPO excitation (DC process). The $^4S_{3/2}$ (green) and $^4F_{9/2}$ (red) emitting states show short average DC lifetimes, τ_{av} < 120 µs, while the IR emitting states, $^4I_{11/2}$ and $^4I_{13/2}$, present lifetimes more than ten times longer, in the order of milliseconds. These long-lived $^4I_{11/2}$ and $^4I_{13/2}$ states can, in principle, act as intermediate states for further excitation under modulated 980 nm excitation or participate in energy transfer processes between close erbium ions, causing the visible UC, as shown in figure 3.6 above. Figure 3.8 below shows the recorded intensity decay curves and corresponding fits of the $^4S_{3/2}$ (green), $^4F_{9/2}$ (red) states for the 0.2% Er^{3+}-doped Y_2O_3 sample under modulated 980 nm CW

excitation (UC). Interestingly, the fitted lifetime of the excited $^4S_{3/2}$ (green), $^4F_{9/2}$ (red) states during the UC process is similar to that under the DC process. However, given the fact that the UC process is based on the long-lived $^4I_{11/2}$ and $^4I_{13/2}$ states, the lifetime of the excited $^4S_{3/2}$ (green), $^4F_{9/2}$ (red) states during the UC process could be much longer compared with that under the DC process. One possible reason for the similar lifetime under both UC and DC processes is that the long-lived $^4I_{11/2}$ and $^4I_{13/2}$ states do not participate in the energy transfer process but just act as intermediate states for the excited state up-conversion process.

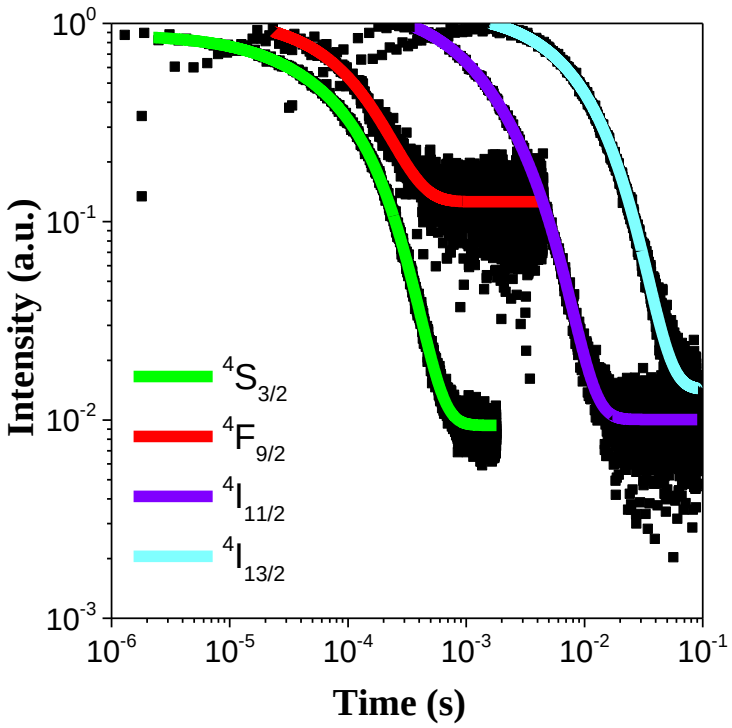

Figure 3.7. *I(t) decay curves of all emitting states of 0.2% Er^{3+}-doped Y_2O_3 under 488 nm OPO excitation.*

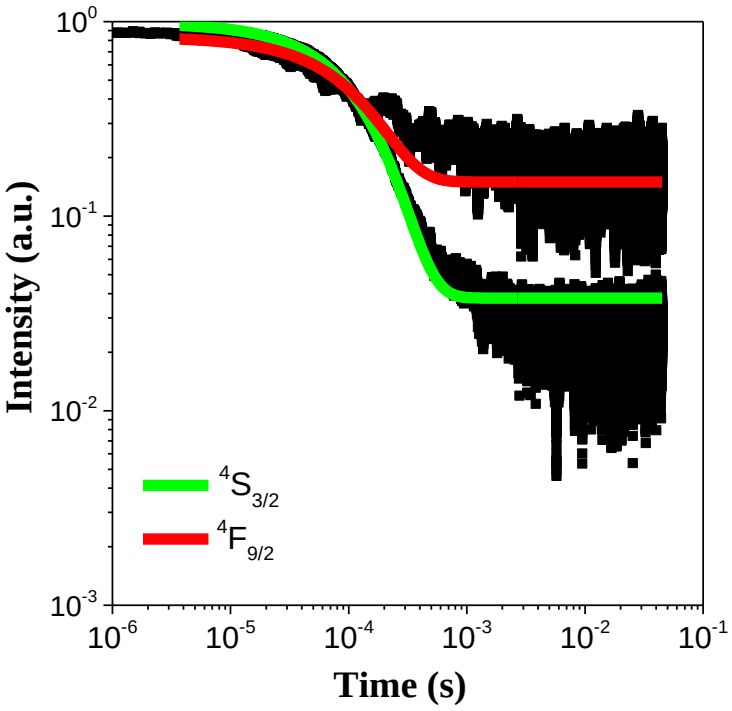

Figure 3.8. *I(t) decay curves of all visible emitting states of 0.2% Er^{3+}-doped Y_2O_3 under modulated 980 nm CW excitation.*

Under the given excitation conditions (power density is $3\times10^6\ Wcm^{-2}$), 0.2% Er^{3+}-doped Y_2O_3 shows the longest DC lifetimes along the $Y_{2-x}Er_xO_3$ series for all the emitting states (shown in figure 3.9 below); this is caused by the reduced non-radiative mechanisms for this dilution [12] and particularly the small contribution of concentration-derived quenching such as CR [12, 36]. The fact that the average UC decay time (~ 150 µs in figure 3.8) is similar to the DC average lifetime (~ 120 µs in figure 3.7) is due to very restricted energy transfer UC, as the averaged distance between erbium ions is the largest in the most diluted sample (0.2% Er^{3+}-doped Y_2O_3). In the general case, if the UC process involves ET through the long-lived $^4I_{11/2}$ or $^4I_{13/2}$ energy states, the lifetime of the UC visible states ($^4S_{3/2}$ or $^4F_{9/2}$) will have a much longer lifetime than the intrinsic lifetime. But, if the UC is only

due to ESA, the $^4F_{7/2}$ emitting level is populated through the energy resonant $^4I_{11/2} + h\upsilon \rightarrow {}^4F_{7/2}$ process and the subsequent rapid relaxation to the green emitting levels ($^2H_{11/2}$ and $^4S_{3/2}$); therefore, the emission processes (lifetimes of the excited states) are exactly the same as under direct 488 nm excitation [26]. Figure 3.9 below summarises the average lifetimes for the Er^{3+}-doped Y_2O_3 series when varying the doping concentration from 0.2, to 10 % for both the UC (excitation at 980 nm) and DC (pulsed excitation at 488 nm). It shows a much more significant difference between UC and DC average decay times for Er^{3+} concentrations higher than 0.2%. This result does confirm that the lifetime difference between up- and down-conversion processes is concentration dependent, and UC lifetime is relevant to the long-lived $^4I_{11/2}$ or $^4I_{13/2}$ energy states for high Er^{3+} doping concentration samples. The corresponding lifetime fittings of the $Y_{2-x}Er_xO_3$ series during both UC and DC processes are given in figure 3.10 (a) to 3.10 (f), figure 3.11(a) to 3.11 (f) separately, and τ_{av} numbers are summarised in table 3.1.

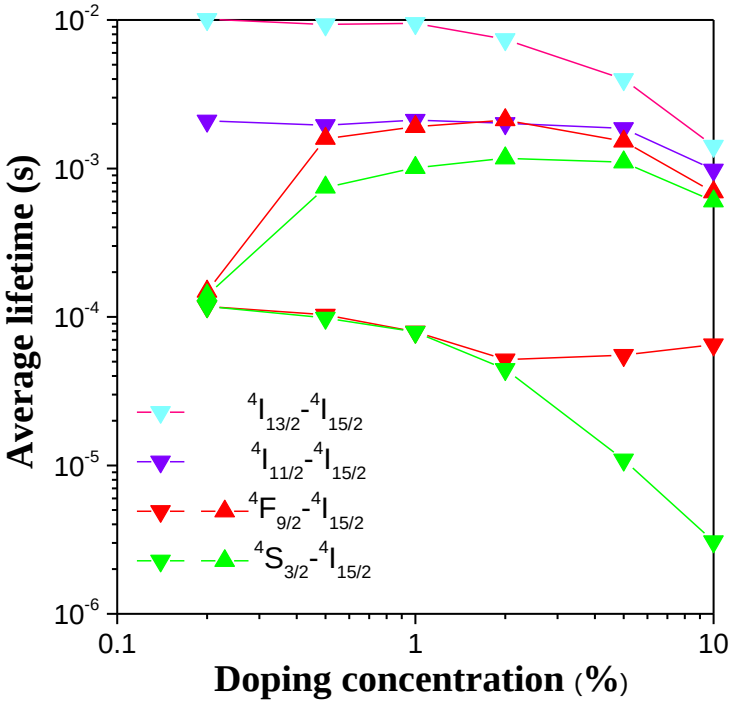

Figure 3.9. *Average decay lifetime of all emitting states of the Er^{3+}-doped Y_2O_3 studied samples for DC and UC processes (see text for excitation conditions). Up-triangles: UC, down-triangles: DC, cyan symbols: emission from $^4I_{13/2}$, violet symbols: emission from $^4I_{11/2}$, red colour symbols: emission from $^4F_{9/2}$, green colour symbols: emission from thermalized $^4S_{3/2}$.*

For all these concentrations, the average lifetimes of $^4S_{3/2}$ and $^4F_{9/2}$ emitting states under 980 nm excitation are in the order of hundreds of microseconds, while the DC lifetimes are considerably shorter (figure 3.9). These much higher values and differences constitute a direct evidence that the dominant UC mechanism under 980 nm excitation for high erbium concentrations is ETU involving the long-lived $^4I_{11/2}$ and/or $^4I_{13/2}$ states as excitation reservoirs. ETU processes imply a modulation of the emission lifetime by the long-lived states acting as a reservoir, as will be discussed in detail in the subsection 3.3.5. Importantly, the occurrence of ETU means that erbium-erbium interactions are present even at 0.5% Er^{3+} content.

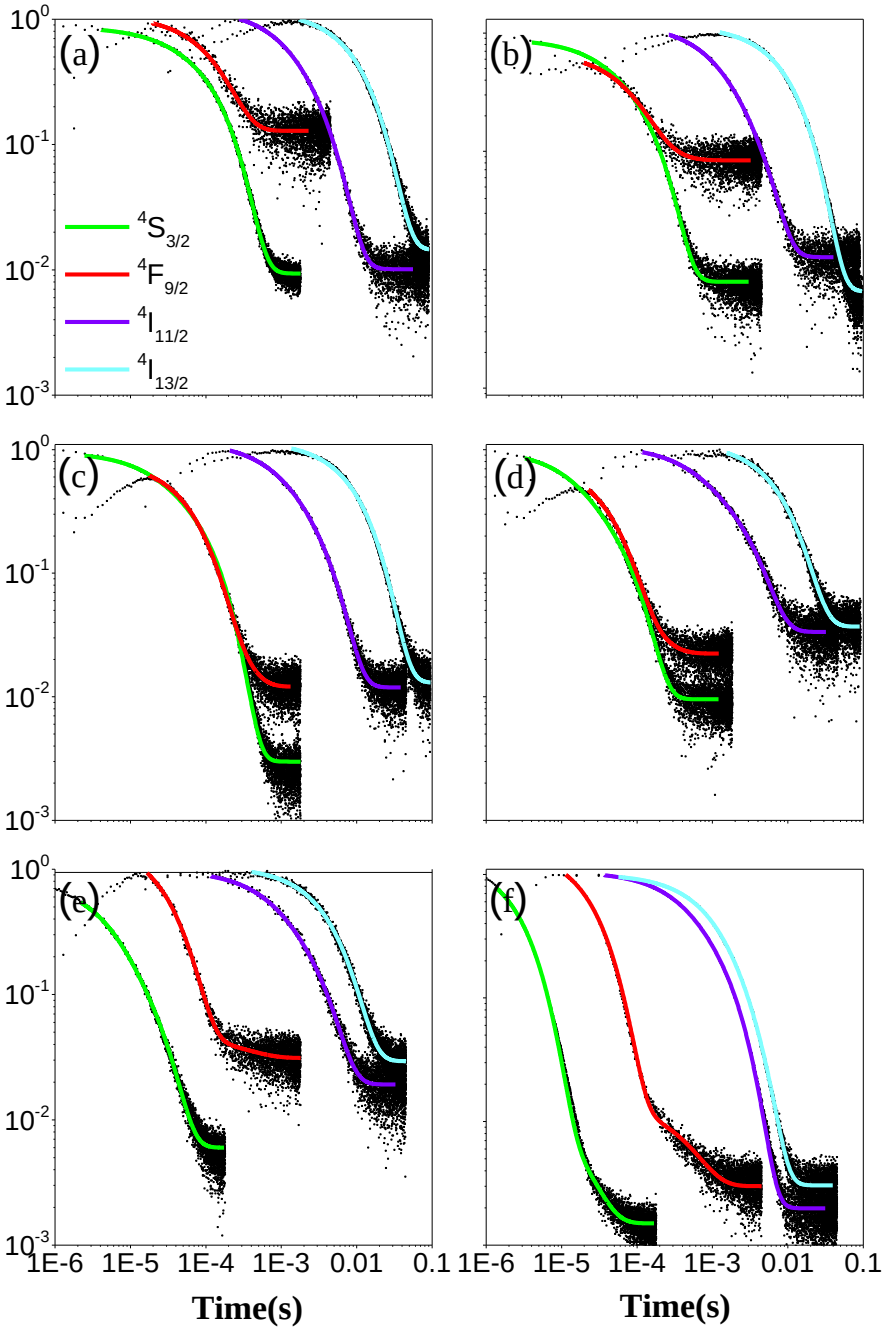

Figure 3.10 *Intensity decay curves of all emitting states of different concentration doped Er^{3+}-doped Y_2O_3 under 488 nm OPO laser:* ***(a).*** *0.2%,* ***(b).*** *0.5%,* ***(c).*** *1%,* ***(d).*** *2%,* ***(e).*** *5%,* ***(f).*** *10% (power density is 3×10^6 Wcm^{-2}).*

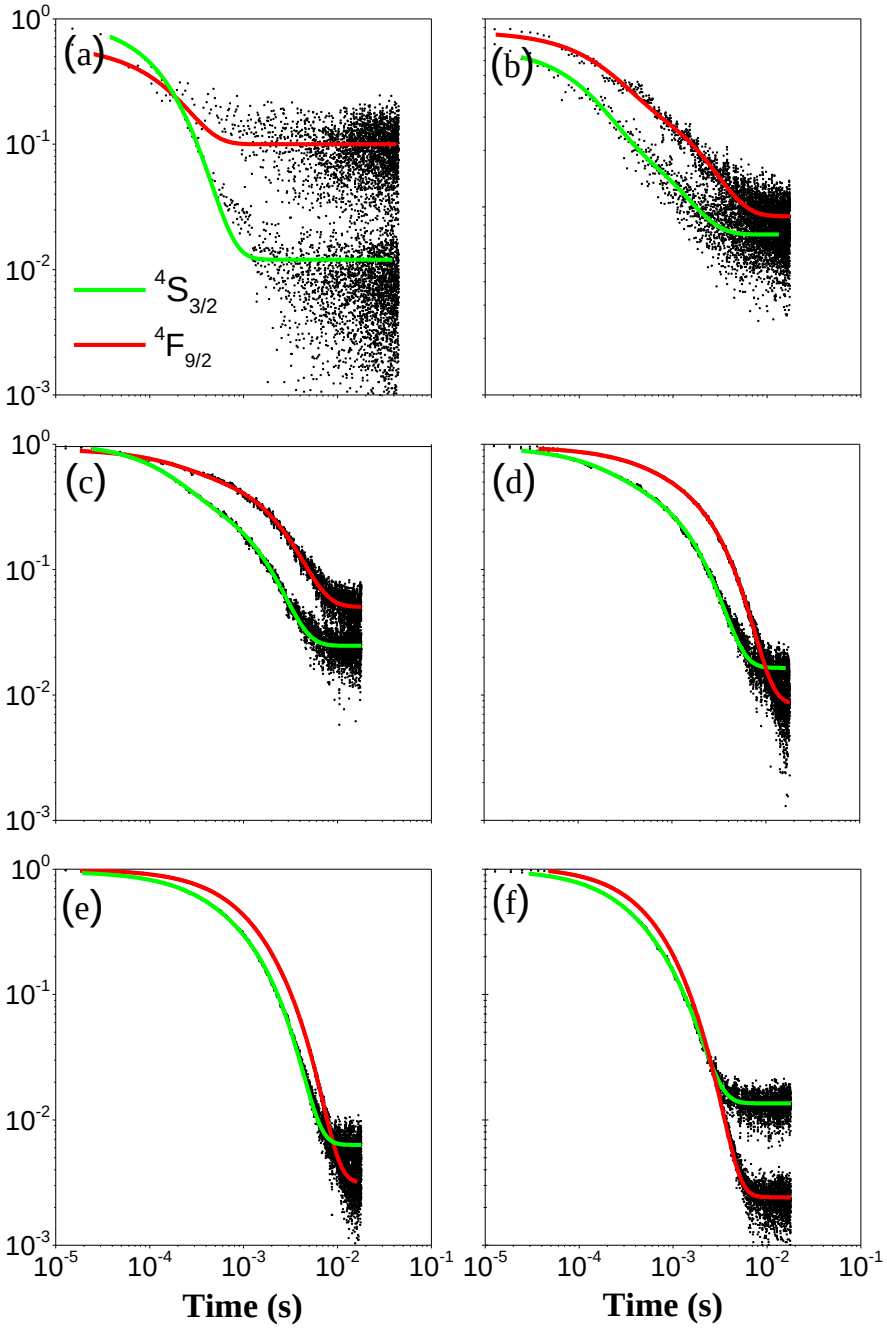

Figure 3.11 *Intensity decay curves of all emitting states of different concentration doped Er^{3+}-doped Y_2O_3 under modulated 980 nm CW laser:* ***(a).*** *0.2%,* ***(b).*** *0.5%,* ***(c).*** *1%,* ***(d).*** *2%,* ***(e).*** *5%,* ***(f).*** *10% (power density is 50 Wcm^{-2}).*

Table 3.1. *Average decay times of the emitting states of the studied Er^{3+}-doped Y_2O_3 samples under 488 nm OPO (power density is 3×10^6 Wcm^{-2}) and 980 nm (power density is 50 Wcm^{-2}) UC excitation conditions. Numbers (in seconds) correspond to solid symbols in figure 3.9. The numbers in the bracket are the fitting parameters.*

Emission Wavelength (nm)	0.2% Er^{3+}-doping		0.5% Er^{3+}-doping	
	488 nm OPO	980 nm UC	488 nm OPO	980 nm UC
1535	10.1×10^{-3} (A_1: 0.579 τ_1:10.1×10^{-3} A_2: 0.579 τ_2:10.1×10^{-3})		9.32×10^{-3} (A_1: 0.575 τ_1: 9.32×10^{-3} A_2: 0.575 τ_2: 9.32×10^{-3})	
980	2.09×10^{-3} (A_1: 0.69 τ_1: 2.42×10^{-3} A_2: 0.509 τ_2: 0.96×10^{-3})		1.95×10^{-3} (A_1: 0.555 τ_1: 2.39×10^{-3} A_2: 0.625 τ_2: 0.85×10^{-3})	
660	118×10^{-6} (A_1: 0.471 τ_1: 118×10^{-6} A_2: 0.471 τ_2: 118×10^{-6})	148×10^{-6} (A_1: 0.235 τ_1: 139×10^{-6} A_2: 0.014 τ_2: 270×10^{-6})	103×10^{-6} (A_1: 0.083 τ_1:182×10^{-6} A_2: 0.527 τ_2: 71.9×10^{-6})	1.59×10^{-3} (A_1: 0.302 τ_1: 1.82×10^{-3} A_2: 0.466 τ_2: 0.19×10^{-3})
560	118×10^{-6} (A_1: 0.716 τ_1: 121×10^{-6} A_2: 0.14 τ_2: 23.7×10^{-6})	140×10^{-6} (A_1: 0.536 τ_1: 134×10^{-6} A_2: 0.023 τ_2: 240×10^{-6})	98.4×10^{-6} (A_1: 0.275 τ_1: 28.8×10^{-6} A_2: 0.6067 τ_2, 107×10^{-6})	0.75×10^{-3} (A_1: 0.459 τ_1: 0.13×10^{-3} A_2: 0.177 τ_2: 0.96×10^{-3})

Emission Wavelength (nm)	1% Er^{3+}-doping		2% Er^{3+}-doping	
	488 nm OPO	980 nm UC	488 nm OPO	980 nm UC
1535	9.52×10^{-3} (A_1: 0.58 τ_1: 9.52×10^{-3} A_2: 0.58 τ_2: 9.52×10^{-3})		7.42×10^{-3} (A_1: 0.557 τ_1: 7.42×10^{-3} A_2: 0.557 τ_2: 7.42×10^{-3})	
980	2.12×10^{-3} (A_1: 0.644 τ_1: 2.45×10^{-3} A_2: 0.496 τ_2: 0.76×10^{-3})		2.01×10^{-3} A_1: 0.454 τ_1: 0.52×10^{-3} A_2: 0.585 τ_2: 2.27×10^{-3}	
660	79.4×10^{-6} (A_1: 0.738 τ_1: 60.2×10^{-6} A_2: 0.061 τ_2: 165×10^{-6})	1.91×10^{-3} (A_1: 0.585 τ_1: 1.97×10^{-3} A_2: 0.281 τ_2: 0.17×10^{-3})	51.6×10^{-6} (A_1: 0.74 τ_1: 38.8×10^{-6} A_2: 0.045 τ_2: 120×10^{-6})	2.12×10^{-3} (A_1: 0.204 τ_1: 0.38×10^{-3} A_2: 0.739 τ_2: 2.2×10^{-3})
560	79×10^{-6} (A_1: 0.598 τ_1: 86.7×10^{-6} A_2: 0.3519 τ_2: 18.6×10^{-6})	1.01×10^{-3} (A_1: 0.396 τ_1: 1.17×10^{-3} A_2: 0.603 τ_2: 0.14×10^{-3})	44.6×10^{-6} (A_1: 0.47 τ_1, 52.8×10^{-6} A_2: 0.51 τ_2:12.9×10^{-6})	1.17×10^{-3} (A_1: 0.362 τ_1: 0.17×10^{-3} A_2: 0.571 τ_2: 1.2×10^{-3})

Emission Wavelength (nm)	5% Er^{3+}-doping		10% Er^{3+}-doping	
	488 nm OPO	980 nm UC	488 nm OPO	980 nm UC
1535	4.4×10^{-3} (A_1: 0.51 τ_1: 4.4×10^{-3} A_2: 0.51 τ_2: 4.4×10^{-3})		1.42×10^{-3} (A_1: 0.487 τ_1: 1.73×10^{-3} A_2: 0.516 τ_2: 0.73×10^{-3})	
980	1.9×10^{-3} (A_1: 0.419 τ_1: 0.60×10^{-3} A_2: 0.54 τ_2: 2.13×10^{-3})		0.98×10^{-3} (A_1: 0.581 τ_1: 1.13×10^{-3} A_2: 0.468 τ_2: 0.32×10^{-3})	
660	41.6×10^{-6} (A_1: 1.616 τ_1: 27.8×10^{-6} A_2: 0.016 τ_2: 220×10^{-6})	1.52×10^{-3} (A_1: 0.41 τ_1: 0.69×10^{-3} A_2: 0.58 τ_2: 1.75×10^{-3})	75.1×10^{-6} (A_1: 1.604 τ_1: 23.1×10^{-6} A_2: 0.011 τ_2: 410×10^{-6})	0.69×10^{-3} (A_1: 0.41 τ_1: 0.24×10^{-3} A_2: 0.568 τ_2: 0.77×10^{-3})
560	11.4×10^{-6} (A_1: 0.272 τ_1: 14.5×10^{-6} A_2: 0.513 τ_2: 4.12×10^{-6})	1.13×10^{-3} (A_1: 0.31 τ_1: 0.31×10^{-3} A_2: 0.643 τ_2: 1.2×10^{-3})	3.07×10^{-6} (A_1: 1.32 τ_1: 2.46×10^{-6} A_2: 0.011 τ_2: 15.1×10^{-6})	0.63×10^{-3} (A_1: 0.487 τ_1:0.85×10^{-3} A_2: 0.562 τ_2: 0.43×10^{-3})

3.3.3. Laser pulse length effect on lifetime

Before discussing in detail the average UC and DC lifetime dependence of the emissions with the Er^{3+} concentration, we must note here that the DC and UC time-resolved I(t) decay curves were measured with different excitation lasers: a 7 ns pulsed 488 nm laser allowing for the measurement of the intrinsic population and depopulation for DC and a 980 nm CW laser, needed to achieve detectable UC, respectively. The reason for using the 980 nm CW laser is that the 980 nm OPO pulse is too weak to achieve the detectable UC fluorescence. It is known that different absorbed powers can potentially cause a completely different distribution of the population of the excited states. Thus, it is a vital step in making sure that the lifetime difference between UC and DC processes is not due to the excitation pulse length or excitation power density.

In order to understand whether the effect of the excitation pulse length plays an important role between DC and UC dynamics, we measured the I(t) decay curves for the DC with different excitation pulse lengths by employing a digitally modulated 405 nm CW laser for the most diluted and concentrated samples. The average decay times measured with 50 μs and 50 ms, 405 nm excitation pulses of 0.2% and 10% Er^{3+}-doped Y_2O_3 and the numerical values are given in table 3.2. It should be noted, the I(t) decay curve of $^4F_{9/2}$ state (red) of the 0.2% Er^{3+}-doped Y_2O_3 was too weak to be measured.

Table 3.2. *Average decay times of the emitting states of the 0.2% and 10% Er^{3+}-doped Y_2O_3 samples under 405 nm excitation for the corresponding laser pulse durations (power density is 16 Wcm^{-2}). The numbers in the bracket are the fitting parameters.*

Emission Wavelength (nm)	0.2% Er^{3+}-doping		10% Er^{3+}-doping	
	50 μs	50 ms	50 μs	50 ms
1535	9.57×10^{-3} (A_1: 0.61 τ_1: 9.57×10^{-3} A_2: 0.61 τ_2: 9.57×10^{-3})	10.2×10^{-3} (A_1: 0.27 τ_1: 6.5×10^{-3} A_2: 0.75 τ_2: 10.9×10^{-3})	1.44×10^{-3} (A_1: 0.59 τ_1: 1.6×10^{-3} A_2: 0.31 τ_2: 0.79×10^{-3})	1.57×10^{-3} (A_1: 0.43 τ_1: 1.91×10^{-3} A_2: 0.49 τ_2: 1.02×10^{-3})
980	2.12×10^{-3} (A_1: 0.49 τ_1: 2.87×10^{-3} A_2: 0.97 τ_2: 1.22×10^{-3})	2.35×10^{-3} (A_1: 0.34 τ_1: 0.92×10^{-3} A_2: 0.67 τ_2: 2.61×10^{-3})	0.91×10^{-3} (A_1: 0.51 τ_1: 1.08×10^{-3} A_2: 0.50 τ_2: 0.33×10^{-3})	1.14×10^{-3} (A_1: 0.61 τ_1: 1.27×10^{-3} A_2: 0.31 τ_2: 0.49×10^{-3})
660			26.2×10^{-6} (A_1: 0.38 τ_1: 26.2×10^{-6} A_2: 0.38 τ_2: 26.2×10^{-6})	448×10^{-6} (A_1: 0.25 τ_1: 502×10^{-6} A_2: 0.61 τ_2: 27.7×10^{-6})
560	124×10^{-6} (A_1: 0.034 τ_1: 241×10^{-6} A_2: 1.75 τ_2: 119×10^{-6})	132×10^{-6} (A_1: 0.011 τ_1: 575×10^{-6} A_2: 1.09 τ_2: 112×10^{-6})	14.9×10^{-6} (A_1: 0.83 τ_1: 2.81×10^{-6} A_2: 0.035 τ_2: 36.9×10^{-6})	180×10^{-6} (A_1: 0.79 τ_1: 3.17×10^{-6} A_2: 0.09 τ_2: 203×10^{-6})

Figures 3.12 and 3.13 below show the corresponding decay curves and emission spectra of the most diluted and concentrated samples excited with the modulated 405 nm CW laser. In figure 3.12 it can be seen that, for all DC emission energy states, the average lifetimes of the 0.2% Er^{3+}-doped Y_2O_3 are independent of the laser pulse length. This is also evidence of the absence of energy transfer between Er^{3+} ions, as will be discussed later. The lifetimes of the longer-lived IR emissions also show no dependence with the excitation pulse length in the case of the 10% Er^{3+}-doped Y_2O_3, as shown in figure 3.13. The $^4S_{3/2}$ state (green), however, shows an increased average lifetime for the 405 nm, 50 μs excitation pulses (13 μs), which is almost an order of magnitude higher with respect to the 488 nm, 7 ns excitation (3 μs), and reaches up to two orders of magnitude higher value (176 μs) for the 405 nm, 50 ms pulse excitation. The $^4F_{9/2}$ state (red) shows a decrease in the lifetime of the 50 μs long pulse excitation (27 μs), approximating the green emission lifetime, but experiences an increase for the 50 ms pulse excitation (449 μs), taking almost the same value as for UC (692 μs). Interestingly, the lifetime of the $^4F_{9/2}$ (red) state under 405 nm, 100 μs excitation pulse increases to 40 μs and it reaches 76 μs under 405 nm, 500 μs excitation pulse, which is almost the same as under 488 nm OPO excitation. The corresponding decay curves and fittings are shown in figure 3.14.

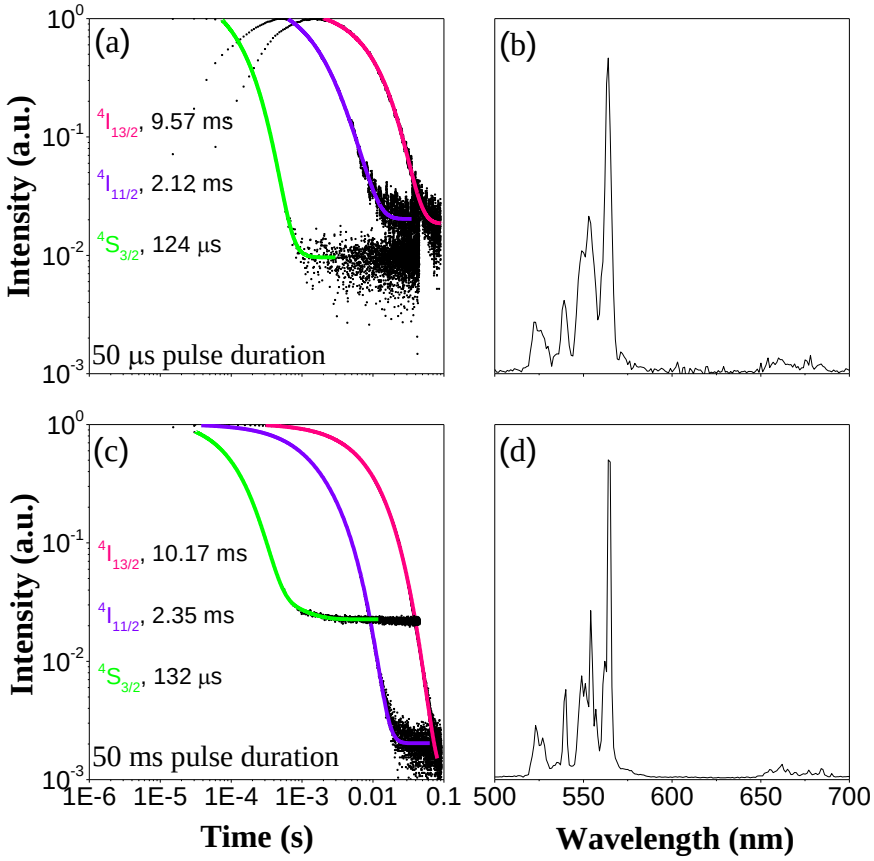

Figure 3.12 (a). *Intensity decay curves of $^4I_{13/2}$, $^4I_{11/2}$, $^4F_{9/2}$ and $^4S_{3/2}$ states of 0.2% Er^{3+}-doped Y_2O_3 with 405 nm CW laser modulated at 50 us pulse length;* ***(b).*** *Emission spectrum of 0.2% Er^{3+}-doped Y_2O_3 with 405 CW laser modulated at 50us pulse length;* ***(c).*** *Intensity decay curves of $^4I_{13/2}$, $^4I_{11/2}$, $^4F_{9/2}$ and $^4S_{3/2}$ states of 0.2% Er^{3+}-doped Y_2O_3 with 405 CW laser modulated at 50 ms pulse length;* ***(d).*** *Emission spectrum of 0.2% Er^{3+}-doped Y_2O_3 with 405 CW laser modulated at 50 ms pulse length (power density is 16 Wcm^{-2}).*

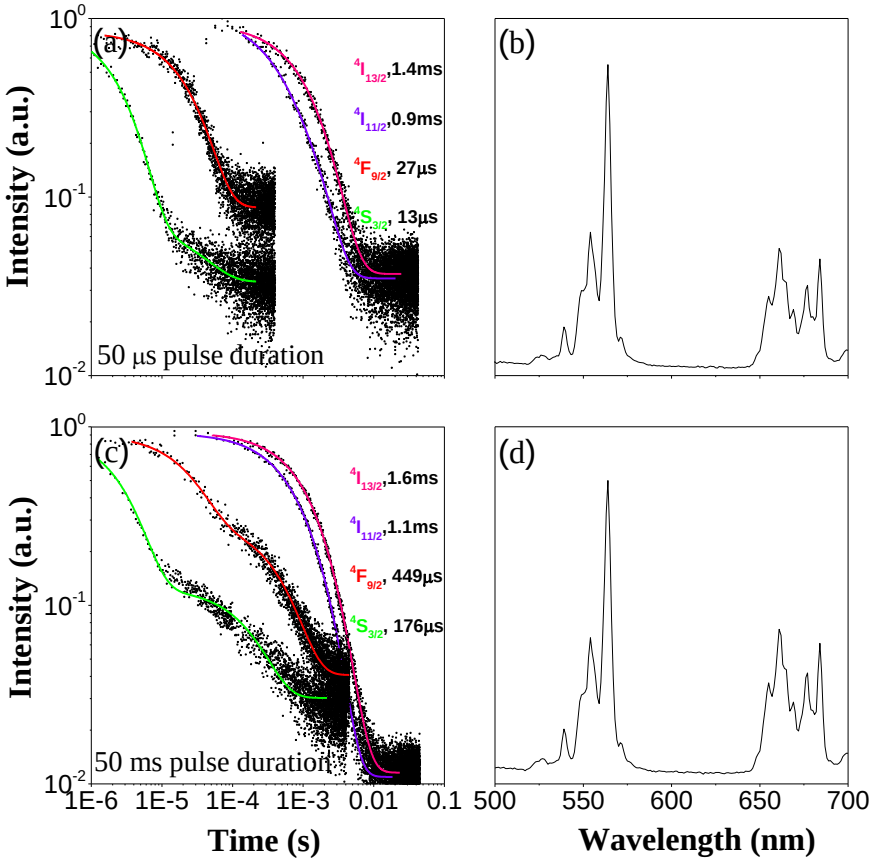

Figure 3.13 (a). *Intensity decay curves of $^4I_{13/2}$, $^4I_{11/2}$, $^4F_{9/2}$ and $^4S_{3/2}$ states of 10% Er^{3+}-doped Y_2O_3 with 405 CW laser modulated at 50us pulse length;* ***(b).*** *Emission spectrum of 10% Er^{3+}-doped Y_2O_3 with 405 CW laser modulated at 50 us pulse length;* ***(c).*** *Intensity decay curves of $^4I_{13/2}$, $^4I_{11/2}$, $^4F_{9/2}$ and $^4S_{3/2}$ states of 10% Er^{3+}-doped Y_2O_3 with 405 CW laser modulated at 50 ms pulse length;* ***(d).*** *Emission spectrum of 10% Er^{3+}-doped Y_2O_3 with 405 CW laser modulated at 50 ms pulse length; It is worth noting here the long lifetime of $^4F_{9/2}$ and $^4S_{3/2}$ states in Figure 3.13.(C) is due to the CR process (power density is 16 Wcm^{-2}).*

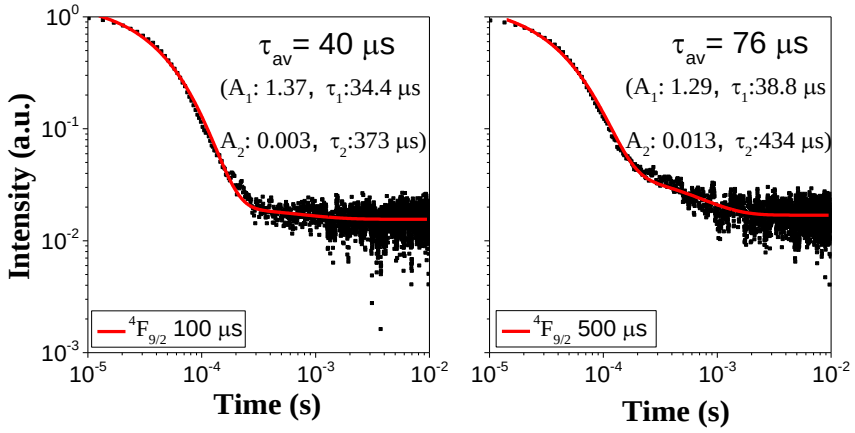

Figure 3.14. *The lifetime of $^4F_{9/2}$ state of 10% Er^{3+}-doped Y_2O_3 under different 405 nm CW laser pulse lengths (power density is 16 Wcm^{-2}). The numbers in the bracket are the fitting parameters.*

Therefore, it can be concluded that only the $^4S_{3/2}$ state (green) and $^4F_{9/2}$ state (red) DC lifetimes of the high Er^{3+} doping concentration samples depend on the excitation pulse length. In detail, the lifetime of the $^4S_{3/2}$ state (green) and $^4F_{9/2}$ state (red) increases with increasing the excitation pulse length. The $^4F_{9/2}$ state (red) DC lifetime of the 10% Er^{3+}-doped Y_2O_3 under 405 nm, 50 ms excitation pulse is approximately the same as the UC lifetime. It suggests that the CR or ET mechanisms could happen in high Er^{3+} doping concentration samples if the excitation pulse time is long enough. And the longer DC lifetime further proves that the longer-lived IR states such as $^4I_{11/2}$ and $^4I_{13/2}$ are involved during this mechanism. However, the intensity decay shape shown in figure 3.13 (c) is completely different from the UC decay curves shown in figure 3.11 (f). The long average lifetime under a long excitation pulse length is actually determined by the long lifetime component (the long tail). Thus, it can concluded that the long UC lifetime is not solely due to the different excitation pulse lengths, especially for the lower Er^{3+} doping concentration samples, such as the 2% Er^{3+} doping concentration (there is an

obvious difference between UC and DC lifetimes, while the CR process should be less likely to happen at low doping concentrations).

3.3.4. Laser power density effect on lifetime

As discussed above, another possible important effect on lifetime is the excitation power density. So, we measured the DC I(t) decay curves by using the 488 nm OPO laser with different excitation power density for the most diluted and most concentrated samples as well.

Interestingly, a similar lifetime dependence with the laser power density has been observed upon varying the energy density of the 488 nm OPO laser pulse. The typical decay curves of the $^4F_{9/2}$ state (red) of the 10% Er^{3+}-doped Y_2O_3 under different excitation power densities are given in figure 3.15, and a summary of the numerical values is given in table 3.3 below. The lifetime increases from 23 μs to 52 μs when the excitation power density increases from 1.5×10^5 Wcm^{-2} to 3×10^6 Wcm^{-2}.

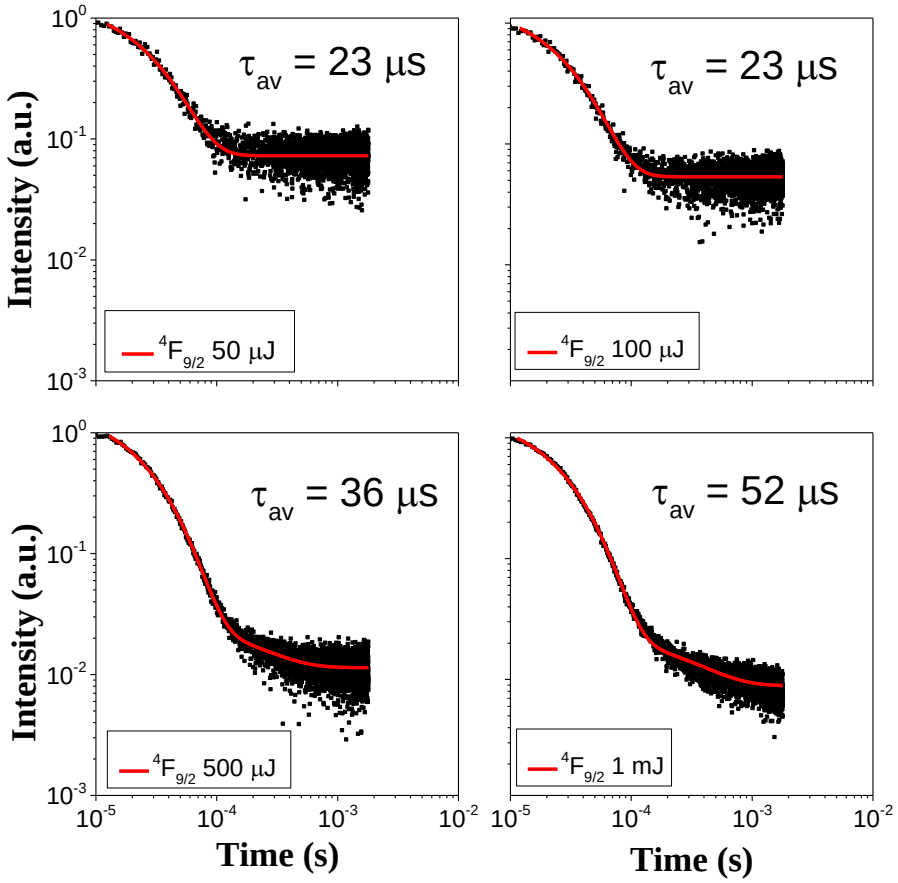

***Figure 3.15**. The lifetime of $^4F_{9/2}$ state (red) of the 10% Er^{3+}-doped Y_2O_3 under different laser power.*

Table 3.3. *Average decay time (in seconds) of the 10% Er^{3+}-doped Y_2O_3 $^4F_{9/2}$ state (red) emission under variable excitation powers (OPO excitation at 488 nm). The numbers in the bracket are the fitting parameters.*

488 nm OPO laser excitation power/ μJ (approx. power density/ Wcm^{-2})	Average decay time at 660 nm of 10% Er^{3+}-doped Y_2O_3/ s
50 (1.5×10^5)	23.2×10^{-6} (A_1: 0.69 τ_1: 23.2×10^{-6} A_2: 0.69 τ_2: 23.2×10^{-6})
100 (3×10^5)	23.0×10^{-6} (A_1: 0.72 τ_1: 23.1×10^{-6} A_2: 0.72 τ_2: 23.1×10^{-6})
500 (1.5×10^6)	35.6×10^{-6} (A_1: 1.65 τ_1: 21.5×10^{-6} A_2: 0.016 τ_2: 196×10^{-6})
1000 (3×10^6)	51.6×10^{-6} (A_1: 1.61 τ_1: 22.5×10^{-6} A_2: 0.015 τ_2: 293×10^{-6})
1200 (3.6×10^6)	65.0×10^{-6} (A_1: 1.604 τ_1: 23.1×10^{-6} A_2: 0.011 τ_2: 410×10^{-6})

Obviously, the average lifetime is longer under higher excitation power density. But, again it should be noted that the time decay shape in figure 3.15 is completely different from that in figure 3.11 (f). And the DC lifetime under high power density is still much shorter than the UC lifetime even for the highest doping concentration sample.

In conclusion, the lifetime of the $^4F_{9/2}$ state (red) of the 10% Er^{3+}-doped Y_2O_3 increases with increasing the excitation power density, which actually explains the reason why the $^4F_{9/2}$ lifetime under 405 nm CW laser is shorter than that under 488 nm OPO excitations: the power density of 488 nm OPO excitation is much higher than that of the 405 nm CW laser. Also, it explains the DC red lifetime increase from 5% to 10% Er^{3+}-doped Y_2O_3 samples: the CR and ET processes are more likely to happen with high Er^{3+} doping concentrations.

3.3.5. Lifetime discussion regarding different Er^{3+} concentrations

The effect of laser pulse length and power density for both the lowest and highest doping concentration samples has been discussed in detail in sections 3.3.3 and 3.3.4. Both factors have an effect on the lifetime, especially for the high Er^{3+} doping concentration samples (10%). However, neither is actually the main reason for the difference between the DC and UC lifetimes or spectra difference (see figure 3.12). In the meantime, it does suggest the long-lived energy states are involved during the long pulse and high energy density excitations during the DC process. The systematic explanation based on the long-lived energy states is discussed below.

Figure 3.9 above shows that the average DC lifetimes of the $^4I_{13/2} \rightarrow {}^4I_{15/2}$ and $^4I_{11/2} \rightarrow {}^4I_{15/2}$ transitions experience a monotonous lifetime decrease with increased Er^{3+} concentration, which can be explained in terms of concentration dependent non-radiative theory. Concentration dependent non-radiative decays occur due to the enhancement of energy transfer processes, which include excitation hopping (and may lead the excitation to non-radiative traps) and CR mechanisms involving the emitting levels, both becoming more likely as the average distance between Er^{3+} ions is reduced. The long lifetime component of $^4S_{3/2}$ (green) and $^4F_{9/2}$ (red) states of the high doping concentration sample (10%) shown in figure 3.13 (c) actually proves the concentration dependent non-radiative mechanism which involves the long lived $^4I_{13/2} \rightarrow {}^4I_{15/2}$ and $^4I_{11/2} \rightarrow {}^4I_{15/2}$ transitions. Some of the CR mechanisms (which may be resonant or vibrationally assisted) include the cooperative non-radiative decays $[^4I_{11/2}, {}^4I_{11/2}] \rightarrow [^4F_{7/2}, {}^4I_{15/2}]$, $[^4I_{13/2}, {}^4I_{11/2}] \rightarrow [^4F_{9/2}, {}^4I_{15/2}]$, $[^4I_{11/2}, {}^4I_{13/2}] \rightarrow [^4F_{9/2}, {}^4I_{15/2}]$ and $[^4I_{13/2}, {}^4I_{13/2}] \rightarrow [^4I_{9/2}, {}^4I_{15/2}]$ (and maybe $[^4I_{9/2}, {}^4I_{11/2}] \rightarrow [^4I_{13/2}, {}^4F_{9/2}]$ [14,21] and $[^4F_{7/2}, {}^4I_{11/2}] \rightarrow [^4F_{9/2}, {}^4F_{9/2}]$ [31]) as represented in figure 3.16 (ETU1, ETU2, $CR7^{(L2)}$, $CR8^{(L3)}$, $CR6^{(L1)}$ and CR1, respectively). In fact, the first two of these processes contribute directly to the ETU and thus are labelled correspondingly.

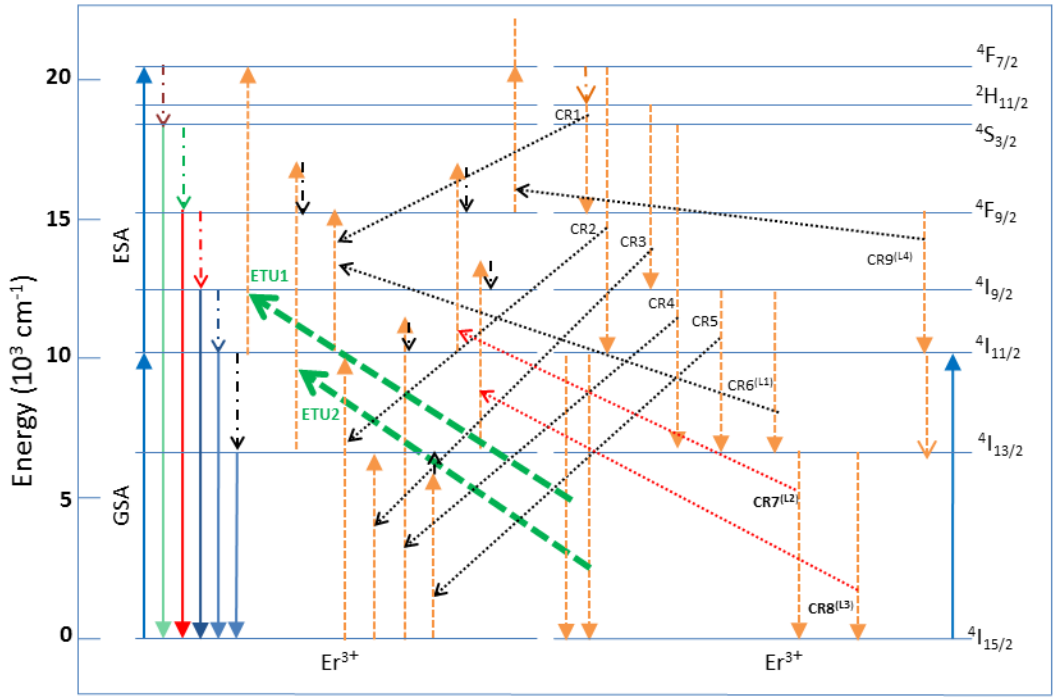

Figure 3.16. *Simplified energy level diagram and most relevant radiative and energy transfer mechanisms in Er^{3+}-doped Y_2O_3. Ground state absorption (GSA), excited state absorption (ESA), green, red and IR luminescence, and energy transfer UC (ETU) as well as cross relaxations (CR) are presented.*

Figure 3.9 also shows that under 980 nm excitation (UC regime), the lifetimes of the $^4S_{3/2}$ (green) and $^4F_{9/2}$ (red) emitting states show a similar trend. They both increase as the Er^{3+} doping concentration increases from 0.2% to 2%. At higher doping concentrations there is a subsequent decrease in the UC lifetime. This variation emphasises that the dynamics of the reservoir and transfer govern the decay of the UC emission [20, 26]. Interestingly, the UC lifetime of the $^4F_{9/2}$ (red) emitting state in the intermediate concentration regime 0.5-5% is considerably longer (approximately twice as long) than that of the $^4S_{3/2}$ (green) emitting state. However, the DC lifetime measured under 488 nm pulse excitation is almost the same in the case of erbium dilutions below 2%. Therefore, it can be concluded that there are different energy transfer processes populating the $^4S_{3/2}$ (green) and $^4F_{9/2}$

(red) emitting states respectively during the UC processes. According to established understanding the longer average lifetime for the red emission suggests that the states feeding $^4F_{9/2}$ are correspondingly longer-lived than those for the green emission [26], implying that the energy transfer, $[^4I_{13/2}, {}^4I_{11/2}] \rightarrow [^4F_{9/2}, {}^4I_{15/2}]$ (ETU2) or the reciprocal, $[^4I_{11/2}, {}^4I_{13/2}] \rightarrow [^4F_{9/2}, {}^4I_{15/2}]$ ($CR7^{(L2)}$) are relevant in ETU in the concentrated systems of the studied series [15, 18] (a detailed discussion regarding the dynamic equations is given in subsection 3.3.6).

Moreover, the concentration enhanced incidence of these CR routes in the re-population of the $^4F_{9/2}$ (red), even in the DC regime (together with the other looping CR mechanism $[^4I_{13/2}, {}^4I_{13/2}] \rightarrow [^4I_{9/2}, {}^4I_{15/2}]$ ($CR8^{(L3)}$ for $^4I_{9/2}$ as given in figure 3.16) [11, 16, 18, 37]), which repopulate the red emitting state and the $^4I_{9/2}$ reservoir, respectively, via long-lived $^4I_{13/2}$ state, explains the increase of the red DC emission lifetime observed in the high concentration Er^{3+}-doped Y_2O_3 when the population of the $^4I_{11/2}$ and $^4I_{13/2}$ states is large (figure 3.9). This model has implications in the changes of the red to green emission colour ratios as a function of power, concentration and excitation wavelength (DC or UC). Importantly, both the indistinguishable (in the excitation conditions) ETU2/$CR7^{(L2)}$ and $CR8^{(L3)}$ looping require a population of the lowest lying states via multiphonon, radiative or other CR decays.

The lifetime study can be summarised as follows: (1), the IR emitting states $^4I_{11/2}$ and $^4I_{13/2}$ experience a systematic lifetime decrease with increasing doping concentration, which we assign to conventional concentration quenching (i.e. hopping and CR). This quenching gets more severe as the concentration increases

and has important implications in the visible photoluminescence, as these levels act as excitation reservoirs due to their long lifetime, in the order of milliseconds. (2), under 980 nm excitation, the lifetime increases from 0.2% to 2% and then decreases from 2% to 10%. The first increase is due to the UC route change, from a situation in which ESA is the main mechanism, to a prevalence of ETU involving the well-known $[^4I_{11/2}, {}^4I_{11/2}] \rightarrow [^4F_{7/2}, {}^4I_{15/2}]$ (ETU1) and, since the lifetime of the red emission is approximately double that of the green emission, ETU2 ($[^4I_{13/2}, {}^4I_{11/2}] \rightarrow [^4F_{9/2}, {}^4I_{15/2}]$)/CR7$^{(L2)}$ $[^4I_{11/2}, {}^4I_{13/2}] \rightarrow [^4F_{9/2}, {}^4I_{15/2}]$ [15, 20]. The subsequent decrease with increasing erbium concentration is predominantly caused by the severe concentration quenching CRi (i = 1-8) which causes a decay in the intrinsic lifetime not only of the emitting levels, but also for the $^4I_{13/2}$, $^4I_{11/2}$ excitation reservoir states in the E < 11 000 cm^{-1} (~1.35 eV) region caused by CRi (i > 5), particularly for Er^{3+} higher than 1%. Interestingly, CRi (i < 5) cause a decrease in the green lifetime, and should be active for both DC and UC, but in the 1 to 8 range no CRi depopulates $^4F_{9/2}$. It is probable that these kind of mechanisms exist, as the DC lifetime tends to also decrease in the 0.2 - 5% concentration range; hence, it is likely that the opposite to CR1, which we label CR9^{L4}, plays a role, as well as maybe other less resonant CRs from $^4F_{9/2}$ to higher lying levels.

Importantly, the looping mechanisms ETU2, CR7$^{(L2)}$, CR8$^{(L3)}$ and CR6$^{(L1)}$ that re-populate the upper excited states for high concentrations and high powers for both the UC and DC regimes [11, 15, 16, 20, 37, 38] get enhanced when the Er^{3+} concentration is increased. The severe enhancement of these processes, which

(except $CR6^{(L1)}$) rely on long-lived lower lying reservoirs explains the increase of the red emission life when the laser energy increases.

3.3.6. Lifetime discussion with dynamic differential equations

In order to make a clear picture of which energy state and which process is involved during the UC process, we did systematic dynamic differential equations corresponding to the population of the coupled Er^{3+} states with the active energy transfers and decays as labelled in figure 3.16, as follows:

$$\dot{n}_6 = -\frac{n_6}{\tau_{r6}} - W_{65}\,n_6 + W_{76}n_7 + W_{ETU1}n_3^2 + W'_{CR9}n_5^2 - W_{CR3}n_6\,n_1 - W_{CR4}n_6n_1 \quad 3.4.1$$

$$\dot{n}_5 = -\frac{n_5}{\tau_{r5}} - W_{54}\,n_5 + W_{65}\,n_6 + W_{ETU2}n_3n_2 + W_{CR7}\,n_3n_2 - 2W_{CR9}n_5^2 \quad 3.4.2$$

$$\dot{n}_4 = -\frac{n_4}{\tau_{r4}} - W_{43}\,n_4 + W_{54}n_5 + -W_{CR3}n_6n_1 + W_{CR8}\,n_2^2 \quad 3.4.3$$

$$\dot{n}_3 = -\frac{n_3}{\tau_{r3}} - W_{32}\,n_4 + W_{43}\,n_4 + W_{CR4}n_6\,n_1 + W''_{CR9}\,n_5^2 - 2W_{ETU1}n_3^2 - W_{ETU2}n_3n_2 - W_{CR7}\,n_3n_2 \quad 3.4.4$$

$$\dot{n}_2 = -\frac{n_2}{\tau_{r2}} + W_{32}n_3 + W_{CR9}\,n_5^2 + W_{CR3}n_6\,n_1 - W_{ETU2}n_3n_2 - 2W_{CR8}\,n_2^2 - W_{CR7}\,n_3n_2 \quad 3.4.5$$

$$\dot{n}_1 = \frac{n_2}{\tau_{r2}} + \frac{n_3}{\tau_{r3}} + \frac{n_4}{\tau_{r4}} + \frac{n_5}{\tau_{r5}} - W_{ETU1}n_3^2 - W_{ETU2}n_3n_2 - W_{CR3}n_6n_1 - W_{CR4}n_6n_1 - W_{CR7}\,n_3n_2 - 2W_{CR8}\,n_2^2 \quad 3.4.6$$

The measured decay probability per unit time of a corresponding state i is given as $1/\tau_i$. And the radiative decay probability per unit time of a corresponding state i is given as $1/\tau_{ri}$. W_{ij} represents the radiative and non-radiative probability per unit

time of a state decaying to the immediately lower-lying one. And the relationship among them is given as $1/\tau_i = 1/\tau_{ri} + \sum_j W_{ij}$ [12]. τ_{ri} depends only on the host matrix and temperature, being irrespective of the Er^{3+} concentration (and can be derived from absorption and time-resolved spectroscopy). The approximation W_{ij} is negligible for $i > j+1$, $W_{ij} = W_{76}$ for $i > 6$ and W_{21} in neglected above (even in the cases of significant branching ratio parameters for a given couple of levels, etc.).

The probability per unit time of a CR process CRk is given by the corresponding rate W_{CRk} and, similarly, for ETU processes, W_{ETUk} is the corresponding rate.

Other approximations include W_{CRk} (negligible) for cross-relaxations labelled CRk, if involving the energy transfer from a level i and $1/\tau_i$, is considerably high. They will not significantly affect the dynamics, in comparison to other processes.

Further approximations can be made considering the reduced value of W_{CR9}, quantifying the concentration quenching CR processes depopulating the red emitting state, which is often neglected in the literature, and it can be observed that, for the given excitation conditions, it is not very significant for the 0.5 to approximately 2% Er^{3+} concentration range in the Er^{3+}-doped Y_2O_3 system. So for these concentrations, the grey terms in the rate equations can be neglected, but not necessarily all of them for higher concentrations.

Importantly, ETU2 and $CR7^{(L2)}$ processes are indistinguishable, as both involve equivalent Er^{3+} pairs, so a further simplification can be made $W_{ETU2} + W_{CR7} = W_{II}$, irrespective of the erbium concentration.

As discussed above, from the observed spectroscopic behaviour, we can determine that W_{CRi}, W_{ETUj} are very small for 0.2% Er^{3+}-doped Y_2O_3, although at least W_{ETU1} and W_{II} ($W_{II} = W_{ETU2} + W_{CR7(L2)}$) become important for Er^{3+} concentrations higher than 0.5% in the Er^{3+}-doped Y_2O_3 system for the studied excitation conditions. This implies these mechanisms are the driving processes for the UC for Er^{3+} concentrations higher than 6.71×10^{19} Er^{3+} ions per cm^3, in this matrix.

Also, over the studied Er^{3+}concentration range and excitation conditions, τ_4 is very small and $W_{43}n_4$ can be considered dominant. The term in $W_{65}n_6$ can also be considered small, as in the DC/ESA processes the red emission is very much negligible in comparison with the green one. This approximation is considered above when discussing the photoluminescence properties for Er^{3+} concentrations 0.5% and higher. It implies that $W_{ETU2} + W_{CR7} = W_{II}$ is the dominant term for populating the $^4F_{9/2}$ state (level 5, red emission) in UC and, together with other looping mechanisms, contributes to the distinct behaviour of the emission of this state.

The solution of the equations under the consideration that CR3, CR4 are not significant, and that energy transfer from $^4I_{11/2}$ (state 3) is much smaller than the decay constant, $1/\tau_3 >> 2W_{ETU1}n_3^2 + W_{II}n_3n_2 + \ldots$ [15], leads to an asymptotic temporal decay of $^4F_{9/2}$ (level 5, red emission) $1/\tau_{av5} = 1/\tau_2 + 1/\tau_3 \sim 1/\tau_3$, and a corresponding $\tau_{av6} = \tau_3/2$ for $^4S_{3/2}$ (level 6, green emission). This is exactly what we observe in the 0.5-2% concentration range (see figure 3.9 and table 3.1 above). Also note that the DC lifetimes are similar for the excitation conditions.

Importantly, as described in the previous sections, the above approximation is no longer valid for Er^{3+} concentrations higher than 5%, in the excitation conditions, so CR mechanisms become severe, and the average decay constant decreases. This causes differences in the DC lifetimes, which (for given excitation conditions) are observed to increase in the case of the $^4F_{9/2}$ (level 5, red emission). This is assigned, as described above, to the influence of looping mechanisms feeding the red-emitting state from longer-lived lower-lying reservoirs. These mechanisms also affect the DC lifetime in other excitation conditions (see tables 3.2 and 3.3).

The above analysis of the CR and ET mechanisms that describe the dynamic and spectral behaviour in the DC and UC processes have important consequences, not only in the general case concentrated Er^{3+} systems but, importantly, in the case of Er^{3+}/Yb^{3+} co-doped systems. Not only because in most practical systems the Er^{3+} concentration is typically higher than 6.71×10^{19} Er^{3+} ions per cm^3 ($NaYF_4$: 2% Er, 20% Yb, for instance, it is more than 4 times that, in the order of 10^{20} Er^{3+} ions per cm^3), but also because the analogous ET mechanisms from the much more absorbing Yb^{3+} ions, whose excited energy is similar to our excitation energies, will be considerable.

3.4. UC and DC spectra

3.4.1. Difference between UC and DC spectra

In the case of 0.2% Er^{3+}-doped Y_2O_3, it is noteworthy that the green to red emission ratio is also very similar in the case of both UC and DC spectra (see figures 3.5 and

3.6). This difference is much more significant for the higher concentrations (see figure 3.17).

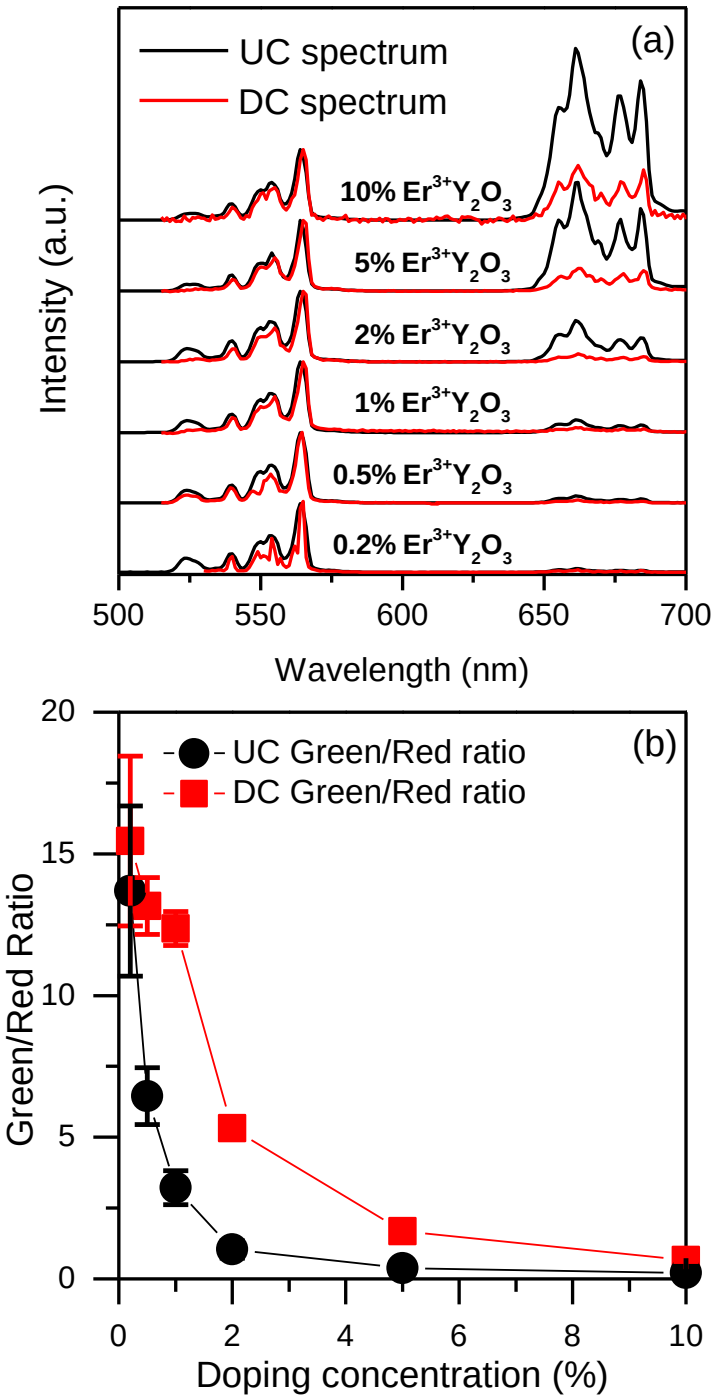

Figure 3.17 (a). *Spectra under both 980 nm (UC) and 488 nm (DC) excitations;* ***(b).*** *Green to red ratio change with doping concentration for UC and DC processes.*

The emission spectra under 488 nm and 980 nm excitations are shown in figure 3.17 (a) above. The green to red ratio decreases with increasing erbium concentration under both 488 nm and 980 nm excitations, but follows a different trend as showed in figure 3.17 (b). Under 488 nm OPO excitation (DC), the green to red ratio change is small during 0.2% to 1% erbium doping concentration, while it decreases by a factor of 10 from 1% to 10% erbium doping concentration. On the contrary, for the 980 nm excitation, it decreases considerably more over the 0.2% to 1% concentration range, with comparatively little subsequent change during the 1% to 10% concentration range. It was estimated that temperature differences caused by different excitation conditions may affect the emission properties. However, in sections 3.3.3 and 3.3.4, it was shown that there is no significant difference in DC spectra (figure 3.13 (b) and 3.13 (d)) under long pulse length even for the 10% Er^{3+}-doping concentration sample (long excitation pulse length may heat the sample up). Similarly, a series of UC measurements of the 10% Er^{3+}-doped Y_2O_3 sample were done under different 980 nm excitation power densities, as high power density could heat the sample up. As shown in figure 3.18 below, there is no obvious ratio change between the green to red emission (integrated number over the whole green or red emission band). Thus, the temperature effect on the spectra can be excluded, while the concentration effects are dominant and must be taken into account to explain this evolution.

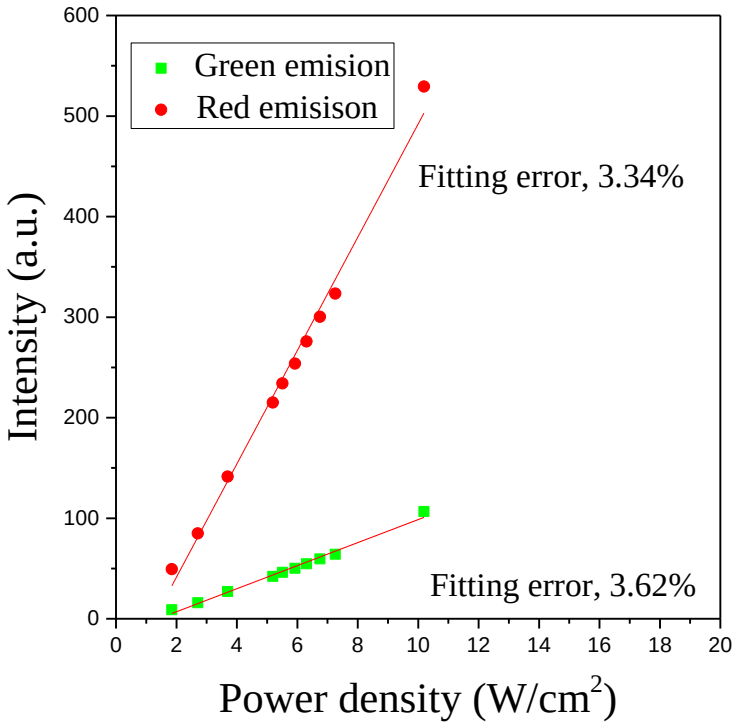

Figure 3.18. *Excitation power dependence of the green ($^4S_{3/2}$) and red ($^4F_{9/2}$) emission intensity of the 10% Er^{3+}-doped Y_2O_3 sample.*

Concentration-induced processes, which affect the population (and decay) of $^4S_{3/2}$ *and* $^4F_{9/2}$ states differently, explain the change in the DC and UC spectra in the explored power regime. Upon direct excitation of the $^4F_{7/2}$ state, the CR-induced changes in the population are not significant from 0.2 % to 1% and, as observed in figure 3.17, nor are the decay processes, as the lifetime is similar for both the red and the green emissions (figure 3.10 (a) to 3.10 (c)). From 2 % to 10 %, as concentration quenching becomes significant, and a severe CR including the processes CRi ($i < 5$) and the looping mechanisms CRi^L ($9 > i > 6$) for high populations of the IR states start to occur, this causes the red emission to become comparatively more intense than the green one, and the lifetime is increased for a

given power or excitation length condition. Thus, the corresponding green to red ratio changes more in this region compared with the 0.2% to 1% regime.

The change in the UC routes explains the change in the emission spectra for the 980 nm excitation UC regime. At 0.2% doping concentration, ESA is the significant UC route, the spectrum being very similar to that observed under 488 nm excitation. With increasing erbium concentration, ETU gets more preponderant. The ETU1 process $[^4I_{11/2}, {}^4I_{11/2}] \rightarrow [^4F_{7/2}, {}^4I_{15/2}]$ contributes to populating the upper states in the same way as ESA or in the DC regime, but ETU2 $[^4I_{11/2}, {}^4I_{13/2}] \rightarrow [^4F_{9/2}, {}^4I_{15/2}]$ / CR7$^{(L2)}$ $[^4I_{11/2}, {}^4I_{13/2}] \rightarrow [^4F_{9/2}, {}^4I_{15/2}]$ and the other CR and looping mechanisms described above result in a higher nominal population of $^4F_{9/2}$. Thus, there is a steady increase of red emission with increasing concentration from 0.2% to 10%. The considerable increase in the population of the long-lived lower-lying $E < 11000$ cm^{-1} (~ 1.35 eV) states means that this decrease is comparatively higher than in DC in the 0.5- 2% range.

3.4.2. Power dependence of the UC luminescence

As mentioned in the introduction, there is a recently published paper [7] that explains the colour change with a three photon processes involving the upper-lying levels. In this paper, the sample is the co-doped $NaYF_4$: 2%Er^{3+}, 18%Yb^{3+} and thus, is populating the Er^{3+} through the Yb^{3+}. One must bear in mind that the oscillator strength of the Er^{3+} $^4I_{11/2}$ is considerably smaller than that of the Yb^{3+} $^2F_{5/2}$. In our excitation and doping conditions, the red to green ratio is comparable for relatively low and high 980 nm excitation powers. These, together with the consistency of the

observations in the blue excitations, shows that it is the different population of the lower-lying levels in the Er^{3+}-doped Y_2O_3, caused by the ET (CR) mechanisms that occur within the interacting Er^{3+} ions, that is the main mechanism for explaining the UC/DC colour difference and the increase of the DC lifetime with the Er^{3+} concentration experienced by the red emission of the Er^{3+}-doped Y_2O_3.

In order to back up our model of the UC processes, we did a power dependence of the UC luminescence. For the simple sensitised UC, the emission from a state which requires ETU will have a slope of 2 when the luminescence intensity is plotted in a double-logarithmic versus absorbed pump intensity [33]. In figure 3.19 below, the unconverted $^4F_{9/2}$ and $^4S_{3/2}$ states luminescence of the 1% Er^{3+}-doped Y_2O_3 versus the power density is linear and the fitted slope is approximately 2, which means the UC involves a two photon process. The reason for choosing the 1% Er^{3+} doping sample is that there is much less ET or CR process and the UC efficiency is quite high at this doping concentration.

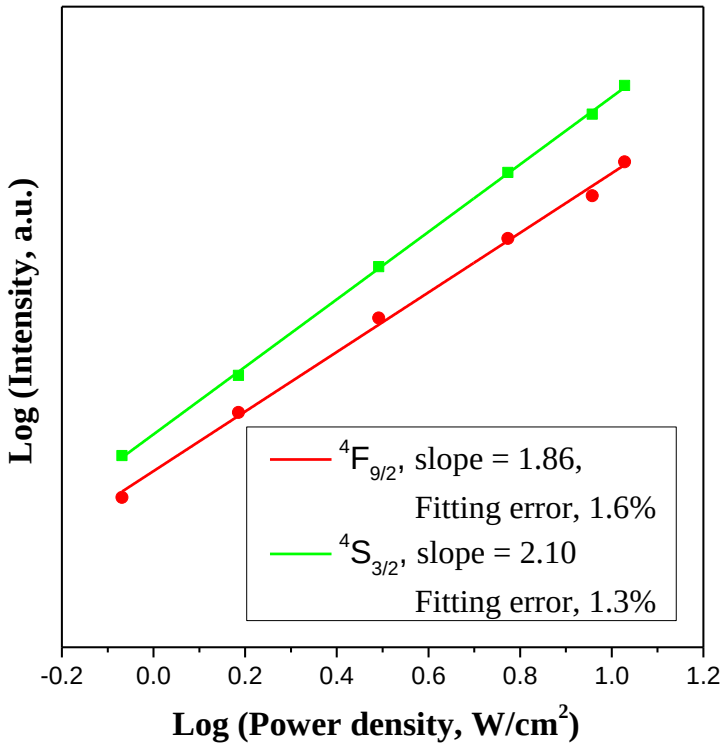

Figure 3.19. *Excitation power dependence at 980 nm of the* $^4F_{9/2} \rightarrow {}^4I_{15/2}$ *(red)* and $^4S_{3/2} \rightarrow {}^4I_{15/2}$ *(green) transitions of the 1%* Er^{3+}*-doped* Y_2O_3.

3.4.3. Luminescence under high energy level ($^2H_{9/2}$) excitation

As for the other assumption [7] that the high energy level ($^2H_{9/2}$) is involved for the long red ($^4F_{9/2}$) lifetime and strong red ($^4F_{9/2}$) emission, the emission spectra were measured with the 375 nm CW laser for both the 5% and 10% Er^{3+}-doped Y_2O_3 samples. If the $^2H_{9/2}$ state was really involved, a long red ($^4F_{9/2}$) lifetime and strong red ($^4F_{9/2}$) emission should be easier to produce with high Er^{3+} doping concentrations, as the cross-relaxation process favours high doping concentrations. But, there is no spectra difference under 375 nm CW laser excitations compared with the previous DC spectra. Figure 3.20 shows the corresponding spectra.

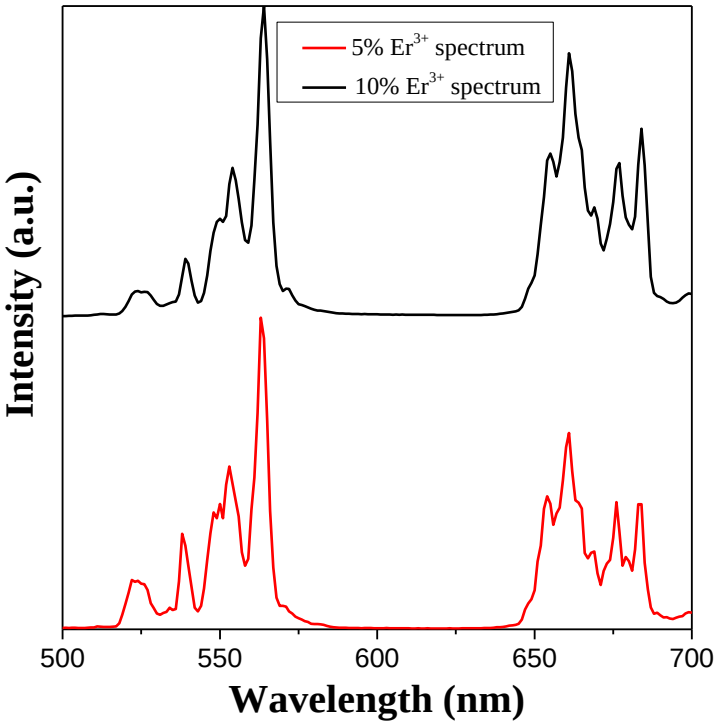

Figure 3.20. *The emission spectra of 5% and 10% Er^{3+}-doped Y_2O_3 under 375 nm CW laser.*

Thus, it is clear that the two photon process assumed in our UC model is real and the high energy level ($^2H_{9/2}$) does not play much of a role in the red emission. The discussions of the power dependence UC luminescence and high energy level excitations back up our detailed discussion above.

3.5. Conclusion

We have studied the UC and DC mechanisms with the simple Er^{3+}-doped Y_2O_3 system as a function of the Er^{3+} concentrations through the change in the dynamics of the emitting states, including the $^4I_{11/2}$ and $^4I_{13/2}$ states. We have done this by employing different excitation power densities, pulse length and wavelengths. We

have described the progressive importance of the ET and CR as the Er^{3+} content increases from the 0.2% to 10%, and its implication on the spectral properties and the decay times of both UC and DC. These properties, including the looping mechanisms, result in an increase in DC decay times for high Er^{3+} concentrations at the given excitation power densities. Moreover, ETU/CR from the $^4I_{11/2}$ to $^4I_{11/2}$ and $^4I_{13/2}$ causes a dominance of the population of the red emitting state for the UC at the high Er^{3+} concentrations, thus severely affecting the green to red emission ratio, and also has an influence on the UC lifetimes of the green and red emissions. Importantly, these processes start being significant at concentrations as low as 6.71×10^{19} Er^{3+} ions per cm^3.

The consideration of these ET and CR routes must be taken into account for understanding the doping concentration dependent UC and DC properties of this material (and maybe others), and the subsequent implementation of the tailored emitting colour properties for phosphors, display and biological applications. These results could also provide deeper insight into a more complex, but more practical Er^{3+}/Yb^{3+} co-doped system.

3.6. Reference

[1] F. Auzel, Upconversion and anti-Stokes processes with f and d ions in solids, *Chemical Reviews*, **104** (2004) 139-174.

[2] X. Liu, H. Qian, Y. Ji, Z. Li, Y. Shao, Y. Hu, G. Tong, L. Li, W. Guo, H. Guo, Mesoporous silica-coated $NaYF_4$ nanocrystals: facile synthesis, in vitro bioimaging and photodynamic therapy of cancer cells, *RSC Advances*, **2** (2012) 12263-12268.

[3] E. Downing, L. Hesselink, J. Ralston, R. Macfarlane, A three-color, solid-state, three-dimensional display, *Science*, **273** (1996) 1185-1189.

[4] J. Zhao, D. Jin, E. P. Schartner, Y. Lu, Y. Liu, A. V. Zvyagin, L. Zhang, J. M. Dawes, P. Xi, J. A. Piper, E. M. Goldys, T. M. Monro, Single-nanocrystal sensitivity achieved by enhanced upconversion luminescence, *Nature Nanotechnology*, **8** (2013) 729-734.

[5] M. Kong, W. Hu, F. Cheng, Z. Huang, J. Zhang, Z. Han, N. Shi, Q. Fan, S. Chen, W. Huang, Efficiency enhancement in P3HT-based polymer solar cells with a $NaYF_4$:2% Er^{3+}, 18% Yb^{3+} up-converter, *Journal of Materials Chemistry C*, **1** (2013) 5872-5878.

[6] R. Martín-Rodríguez, S. Fischer, A. Ivaturi, B. Froehlich, K. W. Krämer, J. C. Goldschmidt, B. S. Richards, A. Meijerink, Highly efficient IR to NIR upconversion in Gd_2O_2S: Er^{3+} for photovoltaic applications, *Chemistry of Materials*, **25** (2013) 1912-1921.

[7] R. B. Anderson, S. J. Smith, P. S. May, M. T. Berry, Revisiting the NIR-to-visible upconversion mechanism in β-$NaYF_4$:Yb^{3+}, Er^{3+}, *The Journal of Physical Chemistry Letters*, **5** (2013) 36-42.

[8] S. Heer, K. Kömpe, H. U. Güdel, M. Haase, Highly efficient multicolour upconversion emission in transparent colloids of lanthanide-doped $NaYF_4$ nanocrystals, *Advanced Materials*, **16** (2004) 2102-2105.

[9] K. W. Krämer, D. Biner, G. Frei, H. U. Güdel, M. P. Hehlen, S. R. Lüthi, Hexagonal sodium yttrium fluoride based green and blue emitting upconversion phosphors, *Chemistry of Materials*, **16** (2004) 1244-1251.

[10] H. -X. Mai, Y. -W. Zhang, L. -D. Sun, C. -H. Yan, Highly efficient multicolor up-conversion emissions and their mechanisms of monodisperse $NaYF_4$:Yb, Er core and core/shell-structured nanocrystals, *The Journal of Physical Chemistry C*, **111** (2007) 13721-13729.

[11] C. Renero-Lecuna, R. Martín-Rodríguez, R. Valiente, J. González, F. Rodríguez, K. W. Krämer, H. U. Güdel, Origin of the high upconversion green luminescence efficiency in β-$NaYF_4$:2% Er^{3+}, 20% Yb^{3+}, Chemistry of Materials, **23** (2011) 3442-3448.

[12] M. C. Tan, G. Kumar, R. E. Riman, M. G. Brik, E. Brown, U. Hommerich, Synthesis and optical properties of infrared-emitting YF_3:Nd nanoparticles, *Journal of Applied Physics*, **106** (2009) 063118.

[13] J. Wang, H. Song, W. Xu, B. Dong, S. Xu, B. Chen, W. Yu, S. Zhang, Phase transition, size control and color tuning of $NaREF_4:Yb^{3+}$, Er^{3+} (RE = Y, Lu) nanocrystals, *Nanoscale*, **5** (2013) 3412-3420.

[14] J. Zhao, Z. Lu, Y. Yin, C. McRae, J. A. Piper, J. M. Dawes, D. Jin, E. M. Goldys, Upconversion luminescence with tunable lifetime in $NaYF_4$:Yb, Er nanocrystals: role of nanocrystal size, *Nanoscale*, **5** (2013) 944-952.

[15] R. Balda, A. J. Garcia-Adeva, J. Fernández, J. M. Fdez-Navarro, Infrared-to-visible upconversion of Er^{3+} ions in GeO_2-PbO-Nb_2O_5 glasses, *Journal of Optical Society of America B*, **21** (2004) 744-752.

[16] P. S. Golding, S. D. Jackson, T. A. King, M. Pollnau, Energy transfer processes in Er^{3+}-doped and Er^{3+}, Pr^{3+}-codoped ZBLAN glasses, *Physical Review B*, **62** (2000) 856-864.

[17] J. Qiu, P. G. Kazanski, J. Si, K. Miura, T. Mitsuyu, K. Hirao, A. L. Gaeta, Memorized polarization-dependent light scattering in rare-earth-ion-doped glass, *Applied Physics Letters*, **77** (2000) 1940-1942.

[18] L. Agazzi, K. Wörhoff, M. Pollnau, Energy-transfer-upconversion models, their applicability and breakdown in the presence of spectroscopically distinct ion classes: A case study in amorphous Al_2O_3: Er^{3+}, *The Journal of Physical Chemistry C*, **117** (2013) 6759-6776.

[19] J. A. Capobianco, F. Vetrone, T. D'Alesio, G. Tessari, A. Speghini, M. Bettinelli, Optical spectroscopy of nanocrystalline cubic $Y_2O_3:Er^{3+}$ obtained by combustion synthesis, *Physical Chemistry Chemical Physics*, **2** (2000) 3203-3207.

[20] J. A. Capobianco, F. Vetrone, J. C. Boyer, A. Speghini, M. Bettinelli, Enhancement of red emission ($^4F_{9/2} \rightarrow {}^4I_{15/2}$) via upconversion in bulk and nanocrystalline cubic Y_2O_3: Er^{3+}, *The Journal of Physical Chemistry B*, **106** (2002) 1181-1187.

[21] G. Y. Chen, H. C. Liu, G. Somesfalean, Y. Q. Sheng, H. J. Liang, Z. G. Zhang, Q. Sun, F. P. Wang, Enhancement of the upconversion radiation in $Y_2O_3:Er^{3+}$ nanocrystals by codoping with Li^+ ions, *Applied Physics Letters*, **92** (2008) 113114.

[22] E. De la Rosa-Cruz, L. A. Díaz-Torres, R. A. Rodríguez-Rojas, M. A. Meneses-Nava, O. Barbosa-García, P. Salas, Luminescence and visible upconversion in nanocrystalline ZrO_2:Er3+, *Applied Physics Letters*, **83** (2003) 4903-4905.

[23] I. Etchart, M. Bérard, M. Laroche, A. Huignard, I. Hernández, W. P. Gillin, R. J. Curry, A. K. Cheetham, Efficient white light emission by upconversion in Yb^{3+}-, Er^{3+}- and Tm^{3+}-doped Y_2BaZnO_5, *Chemical Communications*, **47** (2011) 6263-6265.

[24] I. Etchart, I. Hernández, A. Huignard, M. Bérard, W. P. Gillin, R. J. Curry, A. K. Cheetham, Efficient oxide phosphors for light upconversion; green emission from Yb^{3+} and Ho^{3+} co-doped Ln_2BaZnO_5 (Ln = Y, Gd), *Journal of Materials Chemistry*, **21** (2011) 1387-1394.

[25] I. Etchart, I. Hernández, A. Huignard, M. Bérard, M. Laroche, W. P. Gillin, R. J. Curry, A. K. Cheetham, Oxide phosphors for light upconversion; Yb^{3+} and Tm^{3+} co-doped Y_2BaZnO_5, *Journal of Applied Physics*, **109** (2011) 063104.

[26] I. Etchart, A. Huignard, M. Bérard, M. N. Nordin, I. Hernández, R. J. Curry, W. P. Gillin, A. K. Cheetham, Oxide phosphors for efficient light upconversion: Yb^{3+} and Er^{3+} co-doped Ln_2BaZnO_5 (Ln = Y, Gd), *Journal of Materials Chemistry*, **20** (2010) 3989-3994.

[27] H. Guo, Y. M. Qiao, Preparation, characterization, and strong upconversion of monodisperse Y_2O_3:Er^{3+}, Yb^{3+} microspheres, *Optical Materials*, **31** (2009) 583-589.

[28] H. Guo, W. Zhang, L. Lou, A. Brioude, J. Mugnier, Structure and optical properties of rare earth doped Y_2O_3 waveguide films derived by sol–gel process, *Thin Solid Films*, **458** (2004) 274-280.

[29] F. Hanic, M. Hartmanová, G. G. Knab, A. A. Urusovskaya, K. S. Bagdasarov, Real structure of undoped Y_2O_3 single crystals, *Acta Crystallographica Section B: Structural Science*, **B40** (1984) 76-82.

[30] Y. Mao, T. Tran, X. Guo, J. Y. Huang, C. K. Shih, K. L. Wang, J. P. Chang, Luminescence of nanocrystalline erbium-doped yttria, *Advanced Functional Materials*, **19** (2009) 748-754.

[31] F. Vetrone, J. -C. Boyer, J. A. Capobianco, A. Speghini, M. Bettinelli, Concentration-dependent near-infrared to visible upconversion in nanocrystalline and bulk Y_2O_3:Er^{3+}, *Chemistry of Materials*, **15** (2003) 2737-2743.

[32] J. Zhang, S. Wang, T. Rong, L. Chen, Upconversion luminescence in Er^{3+} doped and Yb^{3+}/Er^{3+} codoped yttria nanocrystalline powders, *Journal of the American Ceramic Society*, **87** (2004) 1072-1075.

[33] J. F. Suyver, A. Aebischer, S. García-Revilla, P. Gerner, H. U. Güdel, Anomalous power dependence of sensitized upconversion luminescence, *Physical Review B*, **71** (2005) 125123.

[34] H. Eilers, Synthesis and characterization of nanophase yttria co-doped with erbium and ytterbium, *Materials Letters*, **60** (2006) 214-217.

[35] J. R. Lakowicz, Principles of fluorescence of spectroscopy, (2006).

[36] J. W. Stouwdam, F. C. J. M. van Veggel, Near-infrared emission of redispersible Er^{3+}, Nd^{3+}, and Ho^{3+} doped LaF_3 nanoparticles, *Nano Letters*, **2** (2002) 733-737.

[37] I. Hernández, R. H. C. Tan, J. M. Pearson, P. B. Wyatt, W. P. Gillin, Nonradiative de-excitation mechanisms in long-lived erbium (III) organic compounds $Er_xY_{1-x}[(p\text{-}CF_3\text{-}C_6F_4)_2PO_2]_3$, *The Journal of Physical Chemistry B*, **113** (2009) 7474-7481.

[38] S. Sivakumar, F. C. M. van Veggel, P. S. May, Near-infrared (NIR) to red and green up-conversion emission from silica sol-gel thin films made with $La_{0.45}Yb_{0.5}Er_{0.05}F_3$ nanoparticles, hetero-looping-enhanced energy transfer (Hetero-LEET): a new up-conversion process, *Journal of the American Chemical Society*, **129** (2007) 620-625.

Chapter 4: NIR emission of sub 10 nm Yb^{3+}-doped $NaYF_4$ nanoparticles with visible light excitation through 2-hydroxy-perfluoroanthraquinone chromophore

4.1. Background and introduction

Trivalent lanthanide-doped nanoparticles have attracted considerable attentions in recent years due to the potential in optical and biological applications as a consequence of unique lanthanide-based f-f transitions, as well as small particle size. These systems incorporate the lanthanides' high emission monochromaticity, high efficiency and long lifetime together with the nanoparticles possibilities for dispersion in aqueous, hydrophobic and polymeric environments. $NaYF_4$ is the most studied matrix due to its non-toxicity and unique chemical and physical structure properties [1-6]. $NaYF_4$ can be formed in α (cubic) and β (hexagonal) polymorphs. Engineered lanthanide doping has shown itself to be very promising for up-converting (near-infrared to visible) biological and solar cell applications, the β structure showing the highest measured up-converting quantum efficiency [7]. More importantly, amplifying devices for telecommunications have been produced based on Er^{3+}-doped $NaYF_4$ nanoparticles in polymer matrices [8, 9].

Both for biological and other optical applications, including bio-probes, image analysis, lasers and telecommunications, the presence of near-infrared (NIR) absorption and emission is particularly appealing and desirable. This is primarily due to the low absorbance and scattering of NIR light (700-1100 nm) in silica fibre

and biological tissues [10-14]. Moreover, the usual long lifetime (in the order of milliseconds or hundreds of microseconds) of NIR luminescence states of Er^{3+}, Tm^{3+}, Yb^{3+} and Nd^{3+} allows for 1) population inversion for lasing and amplification [8, 9] and 2) gated detection imaging and probing [10-14], which favours an increase of the signal to noise ratio, detection threshold and resolution (an advantage that adds up with the long absorbing/emitting wavelength, away from many natural absorptions and emissions to strongly reduce backgrounds).

It is well known that due to the Laporte selection rule, the oscillator strength of the f-f transitions of the lanthanide is limited, and thus, the overall absorption (and consequently emission intensity) is decreased in comparison to optical transitions in other systems, such as fluorescent molecules or semiconductors. Among solutions to increase the lanthanide excitation and emission, co-doping of the host nanoparticle matrix with other ions has been employed [8, 15]. When the aim is to increase the absorption cross-section by means of indirect excitation in another centre (sensitiser) and subsequent energy transfer to the emitting lanthanide (activator), this is termed sensitisation. For NIR-based excitation and/or emissions, sensitisation with Yb^{3+} ions is typically employed and allows for a considerable enhancement in the intensity, although still limited by the oscillator strength of the $^2F_{7/2} \rightarrow {}^2F_{5/2}$ f-f transition.

Another interesting sensitisation strategy includes the incorporation of organic chromophores in chelating ligands, which can transfer the absorbed energy to the excited energy states of lanthanides (this is sometimes called the ‘antenna effect’). However, exposure of the NIR-emitting lanthanides to an environment rich in C-H,

O-H or N-H groups [16] (as is usual in organic compounds) results in strong vibrational quenching of the emission, due to the comparable energy gaps of lanthanides and the 3^{rd}-5^{th} overtones of hydrogenated groups' vibrational quanta [17, 18] (see chapter 1 for more details). A number of alternatives, including fluorination [19] and chlorination [11] of the organic groups have been proposed, some of them resulting in considerable increases of the emission with relatively high emission efficiencies and correlated long lifetimes.

The possibility of attaining organic chromophore-mediated sensitisation of NIR-emitting lanthanides in inorganic matrixes, including nanoparticles, has been recently demonstrated [6, 20], including Yb^{3+}-based NIR-to-visible UC [21]. Visible lanthanide emitters [20, 22] can also be sensitised similarly, upon higher energy excitation within the ultra-violet wavelength range. Functionalisation of the nanoparticle surface with organic chromophores allows coupling of the enhanced absorption of the chromophores, similar to the organic complexes described above, while retaining the relatively long lifetime/low quenching rates for NIR-states, as well as nanoparticles dispersion and processability properties. The lanthanides inside the inorganic nanoparticles are relatively isolated from the surroundings, and thus less quenched in aqueous or other hydrogenated solvents, which may favour a longer lifetime for 'wet' applications [22]. Importantly, the use of red-shifted chromophores in sensitised lanthanide systems is desirable over UV sensitisation. This is not only due to the advantage of employing low cost excitation sources, but also to the more favourable coupling between the organic and lanthanide levels, as

well as increased penetration in tissues and reduction of background or degradation of polymer hosts [12].

In this chapter, we show that monodisperse, sub 10 nm Yb^{3+}-doped α-$NaYF_4$ nanoparticles can be sensitised by the corresponding 2-hydroxy-perfluoroanthraquinone (1,2,3,4,5,6,7-heptafluro-8-hydroxyanthracene-9,10-dione) chromophore with visible excitation wavelength in the red shifted 400-600 nm range. This 2-hydroxy-perfluoroanthraquinone compound has been employed for the sensitisation of Er^{3+} ions in tetrakis complexes, in which it acts as a chelating ligand [23] and in particular in the telecommunication application range (1.5 μm) [8, 9, 24]. The complexes of this fluorinated ligand showed a relatively long lifetime due to the lack of hydrogen, but still only in the range of tens of microseconds. In this chapter we employ this combination of fully fluorinated chromophore, nanoparticle host and Yb^{3+} lanthanide ions to explore the possibility of a visible light sensitised NIR emitter with long lifetime, and to investigate the energy transfer pathways within the hybrid inorganic/organic composite material. We performed a time-resolved spectroscopic study including dynamic measurements as a function of the excitation wavelength and pulse length, paying particular attention to the quenching and sensitisation mechanisms. We observed a strong dependence with the excitation power/pulse length which relates to the surface-to-core of the nanoparticle energy migration and can be employed to modulate the Yb^{3+} lifetime. Moreover, the sensitisation increases with the ratio between chromophore to nanoparticles, which further confirms the assumption of energy transfer from the organic chromophore to the nanoparticles. The demonstration of this energy

migration and manipulation of the lifetime are important problems in relation to understanding and using these systems in biological applications [25].

4.2. Experimental

4.2.1. Ligand capped sub 10 nm Yb^{3+}-doped $NaYF_4$ nanoparticle synthesis

The general procedure of preparing sub 10 nm Yb^{3+}-doped $NaYF_4$ nanoparticles, as well as binding the 2-hydroxy-perfluoroanthraquinone ligand with nanoparticles, is described in detail in chapter 2. However, in order to understand the energy transfer process between the organic chromophore ligand and nanoparticles and find out the best sensitisation, different ligand capped nanoparticle concentrations, as well as differing ratios of ligand to nanoparticles, were characterised. In detail, the original sample 1 was diluted from concentration 3.46 mg/ml to 0.19 mg/ml (sample 6). Then, the concentration of nanoparticle in sample 6 remained constant, while a different concentration of organic chromophore was used. Table 4.1 and 4.2 below are the detailed experimental recipes for the different ligand capped nanoparticle concentrations and different ratios of ligand to nanoparticles.

Table 4.1. *Nanoparticle and organic chromophore ligand concentrations for samples with fixed ratio of nanoparticle to ligand.*

Sample	Sample 1	Sample 2	Sample 3	Sample 4	Sample 5	Sample 6
Nanoparticle concentration (mg/ml)	3.33	2.19	1.45	0.725	0.363	0.182
Organic ligand concentration (mg/ml)	0.13	0.086	0.057	0.029	0.015	0.008

Table 4.2. *Nanoparticle and organic chromophore ligand concentrations for samples with fixed nanoparticle concentration.*

Sample	Sample 7	Sample 8	Sample 9	Sample 10	Sample 11
Nanoparticle concentration (mg/ml)	0.182	0.182	0.182	0.182	0.182
Organic ligand concentration (mg/ml)	0.023	0.037	0.052	0.067	0.191

4.2.2. Optical instrumentation

For the lifetime measurement of the ~1030 nm luminescence of Yb^{3+} ions, a Continuum Panther optical parametric oscillator (OPO) laser and a 405 nm

continuous wavelength (CW) laser (VL01132A02) were used. The NIR luminescence was dispersed by a Triax 550 spectrometer (gratings: 600 lines/mm) and detected by a Hamamatsu R5509-072 photomultiplier.

For the excitation measurements, a xenon lamp together with a Jobin-Yvon Horiba Triax 180 spectrometer (gratings: 1200 lines/mm) were used as the monochromatic excitation light source. The intensity of the monochromatic light after the spectrometer was recalibrated by a Newport 918D-UV-OD3R silicon photon detector. The NIR luminescence spectrum was measured with the same detector using a 7265 DSP Perkin Elmer lock in amplifier.

4.2.3. Material characterisation

Powder X-ray diffraction (XRD) patterns of the dried Yb^{3+}-doped $NaYF_4$ nanoparticles were recorded using Cu Kα radiation ($\lambda = 1.5418$ Å). The measured XRD patterns are presented in figure 4.1 below and matches the corresponding alpha phase (cubic, $Fm\bar{3}m$) $NaYF_4$. Note that the broadening of the peaks is due to the small particle size. Figure 4.2 below is the cubic $NaYF_4$ structure.

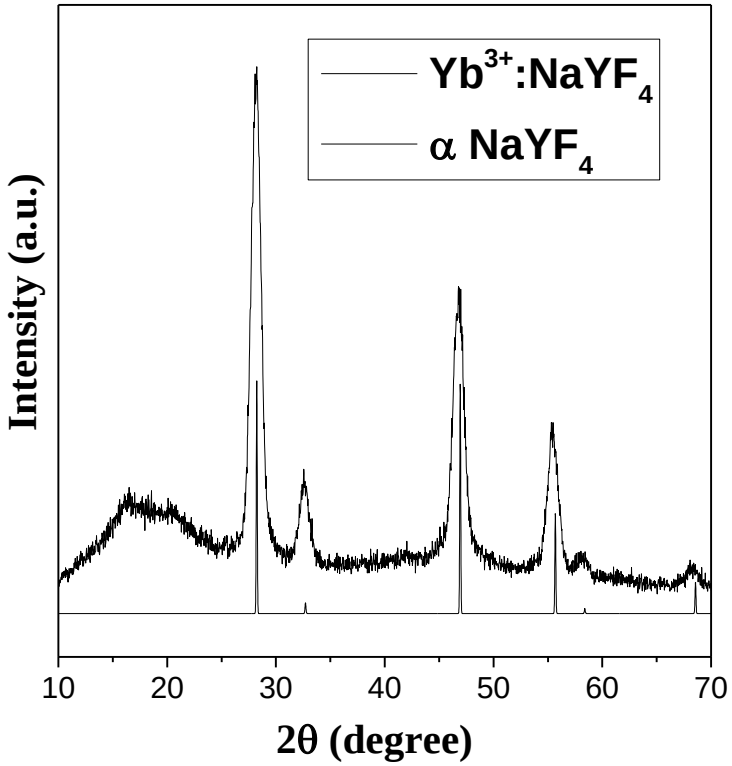

Figure 4.1. *Measured XRD patterns of α phase Yb^{3+}-doped $NaYF_4$ nanoparticles and the calculated line pattern for α phase $NaYF_4$ structure.*

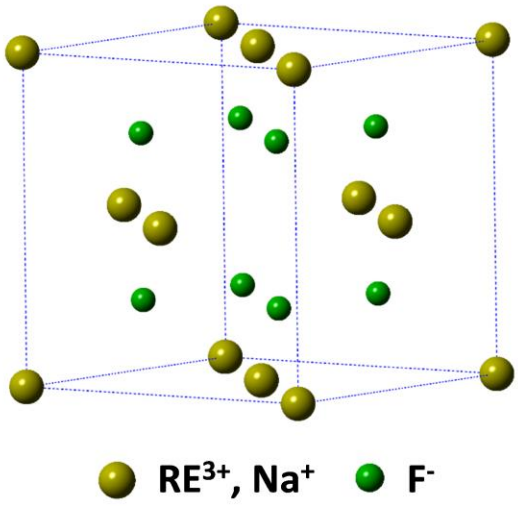

Figure 4.2. *Cubic $NaYF_4$ Structure.*

Transmission electron microscopy (TEM) images were taken on a Tecnai FEI T20 microscopy operated at 200 KV. The TEM image of the Yb^{3+}-doped $NaYF_4$ nanoparticle is given in figure 4.3 below. The sample consists of monodisperse near-spherical nanoparticles of the Yb^{3+}-doped $NaYF_4$ with an average size of 6.28 nm ± 1.87 nm.

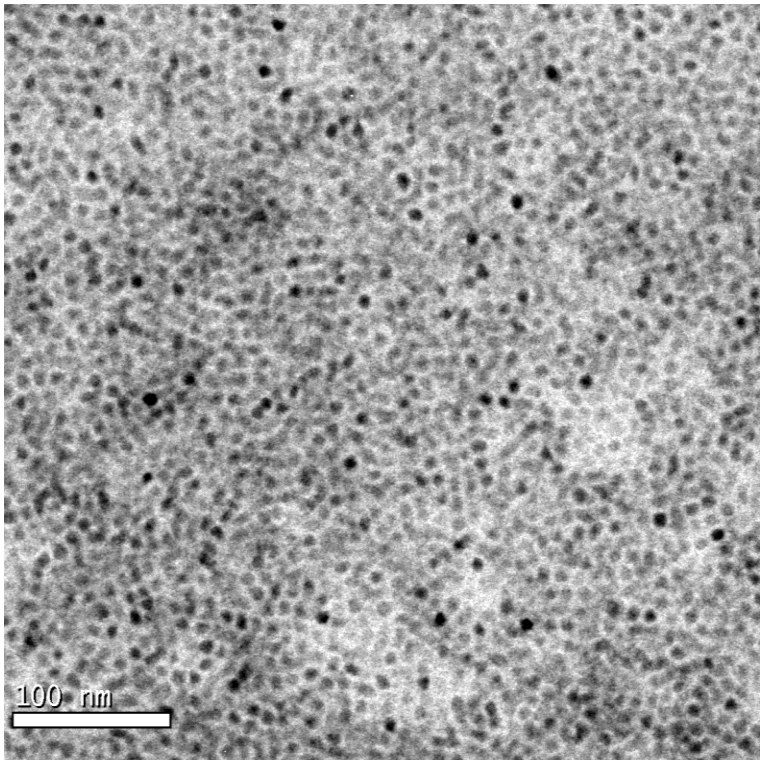

Figure 4.3. *TEM image of the 10% Yb^{3+}-doped $NaYF_4$ nanoparticles.*

4.3. Results and discussions

4.3.1. Emission and excitation spectra of sample 1

Yb^{3+} has only one excited energy state $^2F_{5/2}$, which corresponds to a ~1.26 eV energy gap compared to the ground state $^2F_{7/2}$. Figure 4.4 below is the NIR luminescence spectra of the 2-hydroxy-perfluoroanthraquinone functionalised 10% Yb^{3+}-doped $NaYF_4$ nanoparticles, which was dispersed in chloroform solvent at a concentration of 3.46 mg/ml (sample 1), and excited at 460 nm with OPO. As seen in figure 4.4, the spectrum is peaking at ~976 nm, which arises from the Yb^{3+} $^2F_{5/2} \rightarrow {}^2F_{7/2}$ transition.

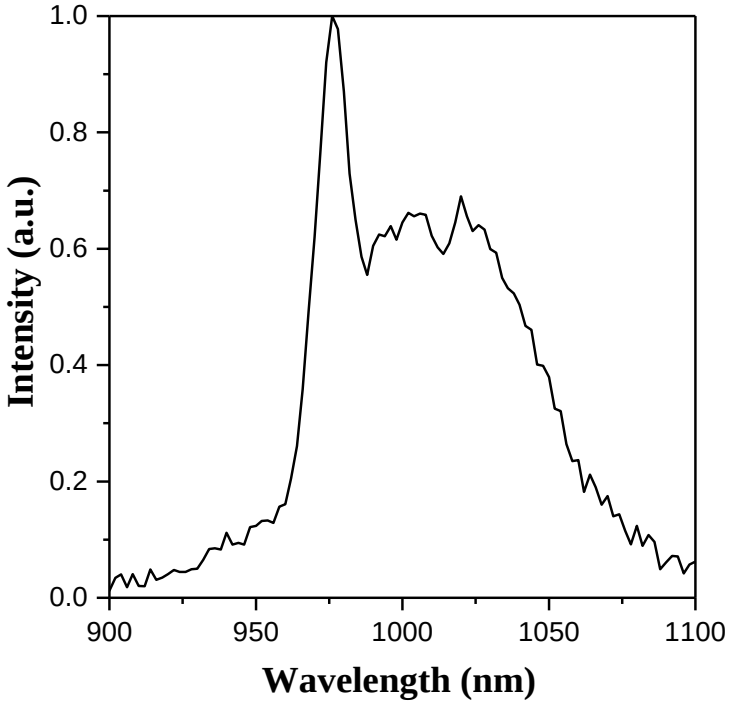

Figure 4.4. *NIR luminescence spectrum of 2-hydroxy-perfluoroanthraquinone functionalized 10% Yb^{3+}-doped $NaYF_4$ nanoparticle excited at 460 nm with OPO.*

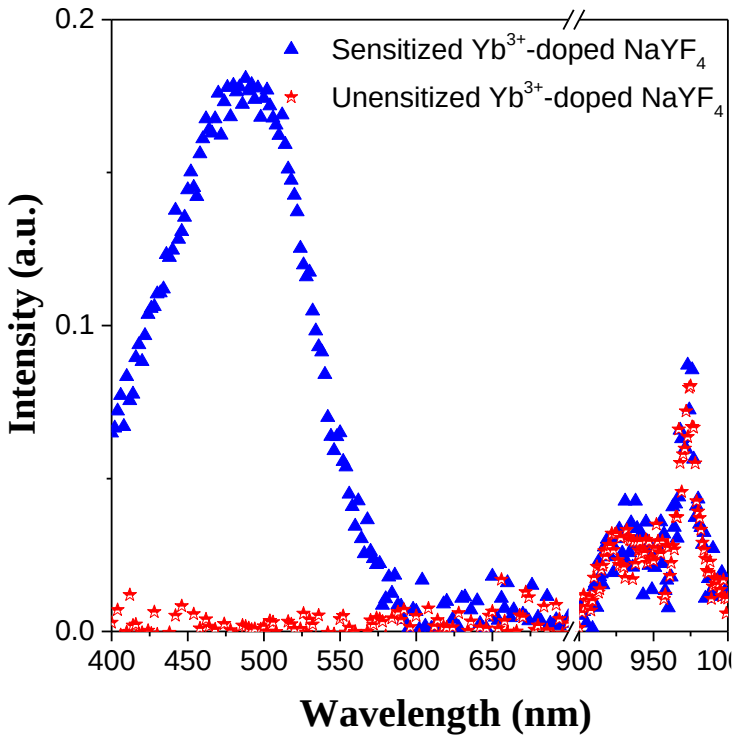

Figure 4.5. *Excitation spectra of functionalized and pristine oleic acid/oleylamine capped 10% Yb^{3+}-doped $NaYF_4$ nanoparticle for the 1030 nm luminescence.*

It should be noted that the Yb^{3+} ion itself has no absorption at the 460 nm wavelength. No visible excitation spectrum was observed for the unsensitised Yb^{3+}-doped $NaYF_4$ nanoparticles (red curve in figure 4.5), however, a visible excitation spectrum was observed for the functionalised one (blue curve in figure 4.5), which suggests there is an energy transfer from the anthraquinone derivative chromophore to the Yb^{3+} ions encapsulated inside the $NaYF_4$ nanoparticle matrix. Figure 4.5 below is the excitation spectra at λ_{em} = 1030 nm measured for the anthraquinone derivative chromophore capped Yb^{3+}-doped $NaYF_4$ nanoparticles, as well as pristine oleic acid/oleylamine capped Yb^{3+}-doped $NaYF_4$ nanoparticles, with a monochromatic xenon lamp light from 400 nm to 700 nm and 900 nm to 1000nm wavelength. Figure 4.5 shows that for the pristine oleic acid/oleylamine capped

Yb^{3+}-doped $NaYF_4$ nanoparticles, there is only the corresponding Yb^{3+} based excitation in the NIR range, which corresponds to the $^2F_{7/2} \rightarrow {}^2F_{5/2}$ transition; while for the functionalised nanoparticles, the excitation spectrum shows an additional broad band in the 400- 600 nm range. Importantly, the band is comparable to the absorption band of the deprotonated 2-hydroxy-perfluoroanthaquinone (see figure 4.6 below) or, equivalently, to the excitation band of the corresponding Er^{3+} or Yb^{3+} complexes of the same ligand [23, 26]. This proves that in the ligand capped $NaYF_4$ nanoparticle system, the organic chromophore is capable of acting as a sensitiser for the Yb^{3+}, which would show, otherwise, no excitation in the visible range. The quotient of the area of the ligand- and Yb^{3+}-based excitation presents an estimation of the sensitisation efficiency. In this case it is roughly an order of magnitude (7.5) more intense upon the chromophore.

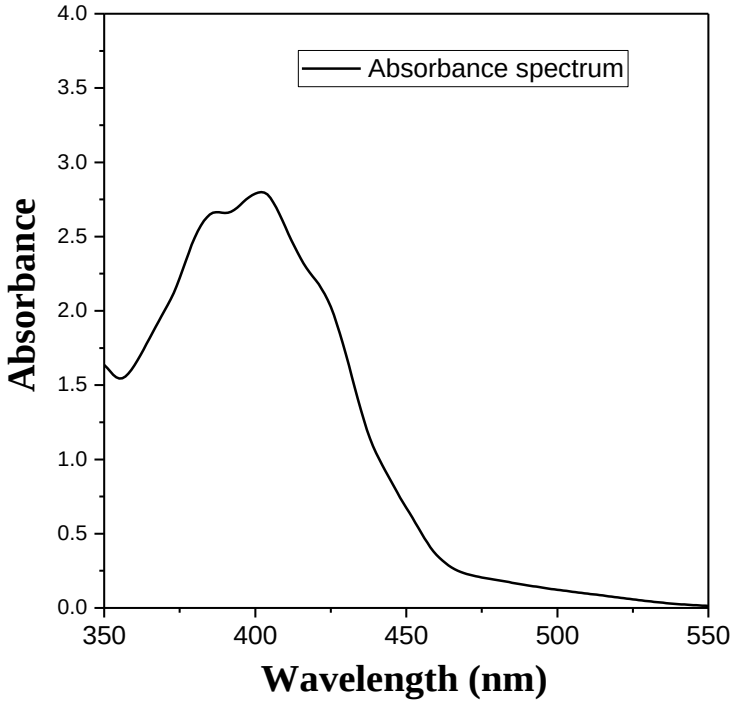

Figure 4.6. *Absorption spectrum of 2-hydroxy-perfluoroanthraquinone chromophore dissolved in chloroform solvent at a concentration of 0.1mg/ml.*

4.3.2. Energy transfer process from organic chromophore to nanoparticle

The energy transfer process is illustrated in figure 4.7 below (known as the Jablonski diagram). The mechanism typically involves absorption of the chromophore's singlet state (allowed optical transition) plus direct singlet to lanthanide energy transfer or triplet-based energy transfer involving a previous inter-system-crossing step. Inter-system crossing causes the creation of a long-lived triplet (typically hundreds of microseconds or milliseconds) in the organic chromophore at the expense of the short-lived singlets (typically nanoseconds or tens of nanoseconds) via a given mixing interaction (such as spin-orbit, for instance). The mechanism for sensitisation of the Yb^{3+}-doped in the $NaYF_4$ matrix

from the organic chromophore may involve energy transfer via Dexter or Förster electron exchange energy transfer interactions [27, 28]. In the case of soft donor ligands, it may occur via organic-Yb^{3+} charge transfer [29], which requires corresponding intermediate metal-ligand steps involving the Yb^{2+} transition state.

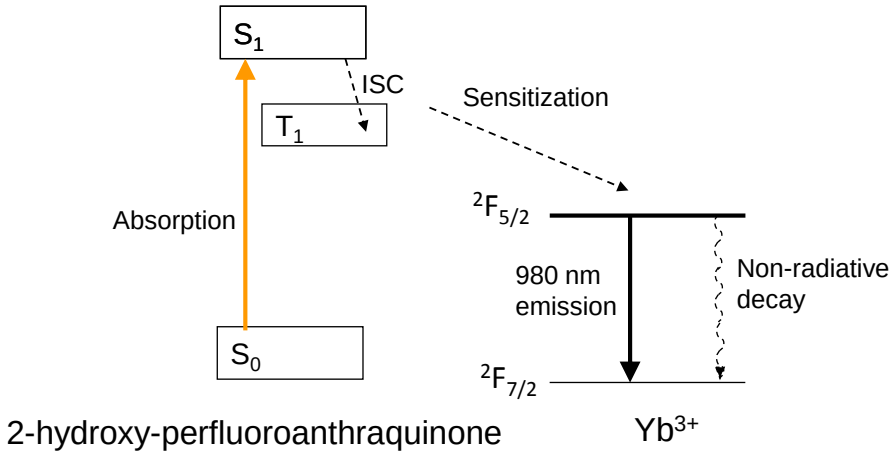

Figure 4.7. *Schematic presentation of organic chromophore mediated Yb^{3+} sensitization process (Jablonski diagram): S_0: ground state of chromophore, S_1: excited singlet state, T_1: excited triplet state, ISC: inter-system crossing.*

4.3.3. Dilution experiments for sample 1

As shown in figure 4.6, the anthraquinone derivative chromophore has a strong absorption during the visible range. Thus, there is a possibility that the visible excited light cannot excite all the chromophores (it means some ligand capped nanoparticles cannot be excited), therefore the measured sensitisation efficiency is low given the fact that the NIR excited light can excite/penetrate all nanoparticles. In order to exclude the effect of organic chromophore concentration, a dilution experiment was done based on sample 1, as shows in table 4.1. For all samples,

sample 1 to sample 6, the ratio between organic chromophore and nanoparticle remained constant while the total concentration (nanoparticle plus organic chromophore ligand) was decreased from 3.46 mg/ml to 0.19 mg/ml. It is assumed that the visible light can penetrate more ligand capped nanoparticles for the lower concentration sample, therefore, a higher sensitisation efficiency would be expected for this sample. Figure 4.8 illustrates the NIR luminescence spectra of sample 1 to sample 6 with the identical 500 nm and 970 nm excitation wavelength provided by the xenon lamp after excitation power density normalisation. The excitation power density of the 500 nm and 970 nm excitation light was calibrated with the silicon diode detector as 36 mW/cm^2 and 15.2 mW/cm^2 separately. It should be noted that figure 4.8. (a) to 4.8. (c) shows the NIR luminescence spectra under both 500 nm and 970 nm excitations for sample 1 to sample 3. From figure 4.8 (a) to 4.8 (c), the NIR luminescence under 970 nm excitation decreases by more than 50%, which is proportional to the concentration change, while the NIR luminescence under 500 nm excitation remains almost constant. This result further confirms the assumption that some ligand capped nanoparticles cannot be excited at high concentration samples. Figure 4.8 (d) shows the NIR luminescence spectra under 500 nm excitation for sample 4 to sample 6. NIR luminescence spectra under 970 nm excitation is not given for sample 4 to sample 6 as the intensity was too weak to be measured. For the sensitisation calculation of sample 4 to sample 6, the NIR luminescence intensity is assumed proportional to the concentration based on the results of sample 1 to sample 3. Table 4.3 is a summary of 1030 nm intensity of sample 1 to sample 6 under both 500 nm and 970 nm excitations.

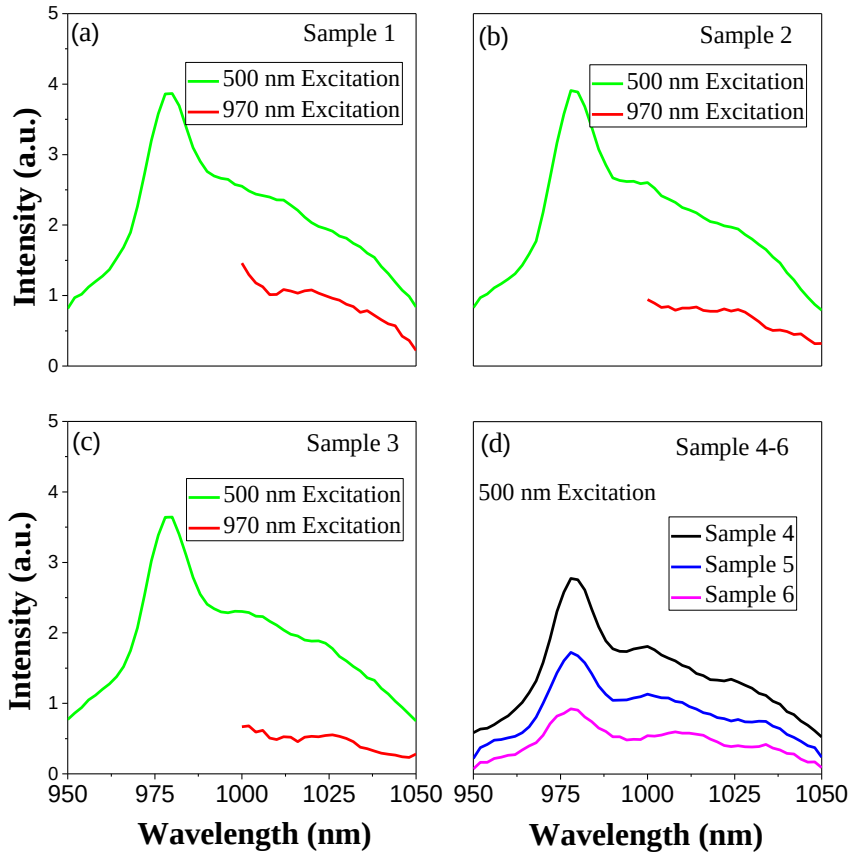

Figure 4.8 *NIR luminescence spectrum of 2-hydroxy-perfluoroanthraquinone chromophore functionalised 10% Yb^{3+}-doped $NaYF_4$ nanoparticle dispersed in chloroform at a concentration of 3.46 mg/ml (sample 1)* ***(a).*** *2.276 mg/ml (sample 2)* ***(b).*** *1.507 mg/ml (sample 3)* ***(c).*** *Under both 500 nm and 970 nm excitations;* ***(d).*** *NIR luminescence spectra under 500 nm excitation of samples at a concentration of 0.754 mg/ml (sample 4), 0.378 mg/ml (sample 5) and 0.12 mg/ml (sample 6) separately.*

Table 4.3. *Summary of 1030 nm intensity ratio of sample 1 to sample 6 under 500 nm and 970 nm excitations.*

Sample	1030 nm intensity ratio (λ_{ex}= 500 nm/ λ_{ex} = 970 nm)
Sample 1	1.96
Sample 2	2.7
Sample 3	3.23
Sample 4	4.97
Sample 5	5.91
Sample 6	5.56

As seen in table 4.3, the sensitisation efficiency increases with decreasing the organic chromophore capped nanoparticle concentration, which is consistent with the assumption made above.

4.3.4. Ligand to nanoparticle ratio effect for sample 6 to sample 11

In addition to the concentration effect, the issue of organic chromophore to nanoparticle ratio needs to be considered. When the nanoparticle concentration is low enough (consider one layer of ligand capped nanoparticle), the higher the ratio of ligand to nanoparticle, there may be better sensitisation from ligand to nanoparticle. In order to investigate the effect of the ligand to nanoparticle ratio, a

series of samples were produced (sample 6 to sample 11), in which the concentration of nanoparticles is the same (0.182 mg/ml) while the concentration of organic chromophore is different (0.008 mg/ml, 0.023 mg/ml, 0.037 mg/ml, 0.052 mg/ml, 0.067 mg/ml and 0.191 mg/ml for sample 6, sample 7, sample 8, sample 9, sample 10 and sample 11 separately), as shown in table 4.2 above.

For the 1.5 ml sample 6 solution, the nanoparticle concentration is 0.182 mg/ml and the organic chromophore concentration is 0.008 mg/ml. Given that the density of $NaYF_4$ is 3980 mg/cm^3, and the average diameter of a nanoparticle is 6.28 nm, the number of nanoparticles can be calculated:

$$N_{nano} = \frac{0.182 \times 1.5}{\frac{4}{3}\pi(6.28 \times 10^{-7})^3 \times 3980} \tag{4.1}$$

And given the fact that the molar weight of the 2-hydroxy-perfluoroanthraquinone ligand is 3.49×10^5 mg, the number of ligand chromophore is calculated by

$$N_{ligand} = \frac{0.008 \times 1.5}{3.49 \times 10^5} \times 6.02 \times 10^{23} \tag{4.2}$$

The calculated ratio between organic chromophore ligand and a nanoparticle for sample 6 is 35. Similarly, the ratio for all the other samples are calculated and summarised in table 4.4 below.

Table 4.4. *Summary of the ratio between organic chromophore and nanoparticles for sample 6 to sample 11.*

Sample	Ratio of ligand to nanoparticle	1030 nm intensity ratio (λ_{ex}= 500 nm/ λ_{ex} = 970 nm)
Sample 6	35:1	5.56
Sample 7	107:1	11.05
Sample 8	173:1	21.22
Sample 9	243:1	29.34
Sample 10	313:1	38.92
Sample 11	891:1	92.26

NIR luminescence spectra were measured under 500 nm excitation for all samples from sample 6 to sample 11. As shown in figure 4.9 below, the NIR luminescence intensity increased with increasing the ratio of ligand to nanoparticle (the organic chromophore ligand concentration). As the concentration of the nanoparticles is constant, the NIR luminescence intensity under 970 nm excitation is assumed to be constant, thus the 1030 nm intensity ratio under both 500 nm and 970 nm excitations can be summarised, as shown in table 4.4.

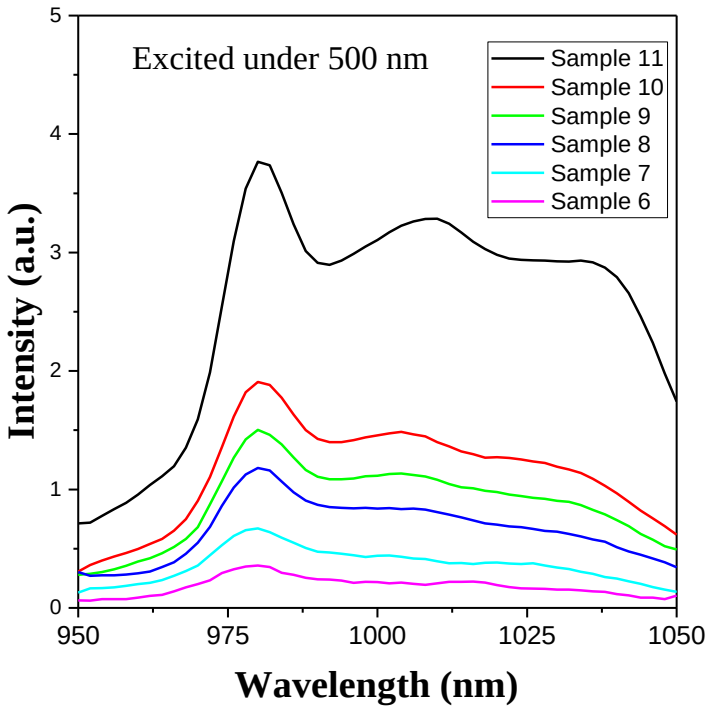

Figure 4.9. *NIR luminescence spectrum of the 2-hydroxy-perfluoroanthraquinone chromophore functionalised 10% Yb^{3+}-doped $NaYF_4$ nanoparticle dispersed in chloroform at a concentration of 0.19 mg/ml (sample 6), 0.205 mg/ml (sample 7), 0.219 mg/ml (sample 8), 0.234 mg/ml (sample 9), 0.249 mg/ml (sample 10) and 0.373 mg/ml (sample 11) under 500 nm excitation.*

As shown in table 4.4 and figure 4.9 above, sensitisation increases with increasing the ratio of organic chromophore to nanoparticles when the nanoparticle concentration is as low as 0.182 mg/ml. The biggest sensitisation measured with single 500 nm and 970 nm wavelengths is 92.26 for sample 11. So, the sensitisation can be more than 300 when integration over the whole visible excitation band is considered, which is the highest among the values reported in the literature.

4.3.5. Lifetime measurements

As stated in chapters 1 and 3, lifetime measurement is an important method for understanding population and depopulation dynamics. In this case, lifetime can provide information on energy transfer between the organic chromophore and Yb^{3+} ions encapsulated inside the $NaYF_4$ nanoparticles.

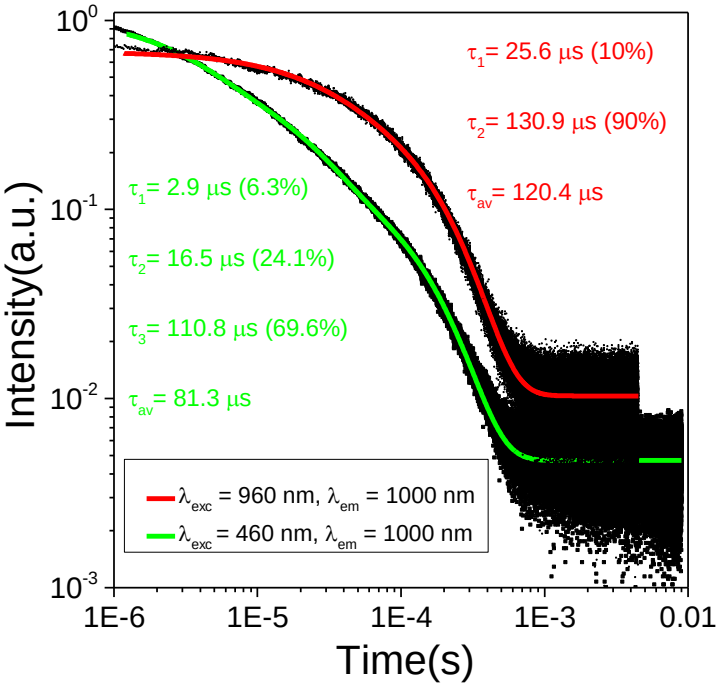

Figure 4.10. *Decay curves of 2-hydroxyperfluoroanthraquinone-capped 10% Yb^{3+}-doped $NaYF_4$ nanoparticles (sample 1) with 460 nm and 960 nm OPO excitations. The numbers in the brackets are the percentage contribution to the average lifetime.*

Figure 4.10 above is the I(t) decay curve for the 1030 nm luminescence, at 460 nm and 960 nm OPO excitations respectively, for the organic chromophore functionalised 10% Yb^{3+}-doped $NaYF_4$ nanoparticles dissolved in a chloroform solution at a concentration of 3.46 mg/ml (sample 1). The decay of the NIR-excited

Yb^{3+} emission is fitted with a double exponential curve, yielding an average lifetime of 120 µs. However, the Yb^{3+} emission decay curve at the visible excitation showed a considerably shorter lifetime (81 µs) and tri-exponential behaviour, with two of the components being ~3 µs and ~17 µs, considerably shorter than any of those obtained for the NIR excitation-based emission.

It is understood that a system that cannot be described by single exponential decay involves different emitting centres, each showing different environments in terms of geometry or neighbouring transferring sites, which results in different population and/or emission routes [30]. In systems showing high surface to volume ratio (and especially in solutions), it is usually inferred that short lifetimes correspond to emitting centres near the surface, and thus show a more distorted geometry, or are more exposed to quenching effects of the environment, while more protected, inner emitters show longer lifetimes [25].

In view of the above, we assign the short lifetime of the chromophore-excited emission to emitting Yb^{3+} ions near the surface. This includes the very short component of 3 µs (representing 6% of the total emission) and the 17 µs (representing 24% of the total emission) emission. They correspond to given populations of Yb^{3+} ions which (1) are excited via energy transfer from the organic chromophore and (2) are exposed to organic or hydrogenated molecules (oleylamine, the ligand itself, etc.).

Evidently, the same population of surface-based Yb^{3+} ions exist in the organic chromophore functionalised nanoparticles with 960 nm OPO excitations. In

principle, similar lifetimes could be expected. However, a different situation must be considered due to the fact that a different population mechanism of Yb^{3+} ions is probed when the 10% Yb^{3+}-doped $NaYF_4$ emitting ions are excited in the corresponding Yb^{3+} NIR absorption bands (960 nm) with respect to the ligand-based excitations (460 nm). This population includes a considerably smaller ratio of Yb^{3+} ions at the surface compared to the core of the nanoparticle, than in the case of ligand-based excitation. A typical schematic diagram of a chromophore capped Yb^{3+}-doped $NaYF_4$ nanoparticle is shown in figure 4.11 below. The proportion of Yb^{3+} ions within a lattice near the surface of the particle, compared to those more than a unit cell inside the volume of the particles, is higher than 50%.

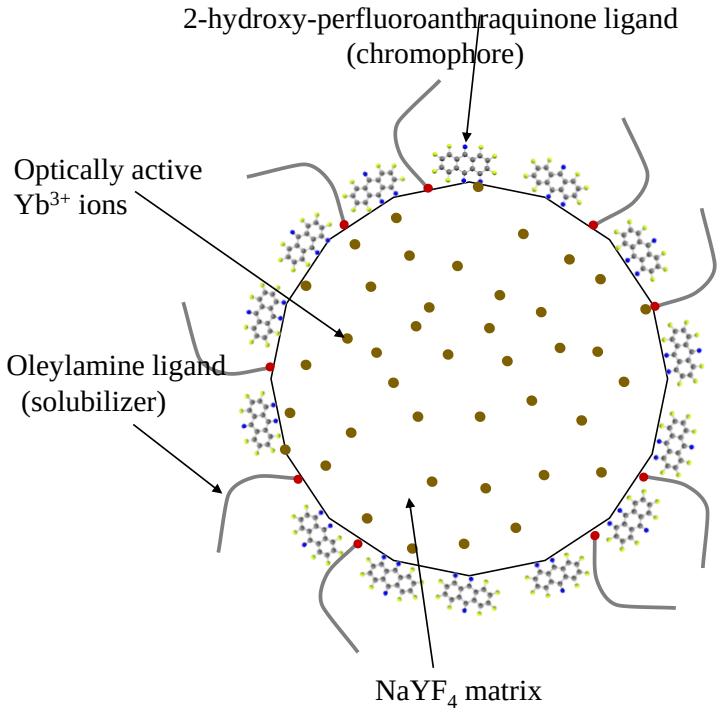

Figure 4.11. *Organic chromophore capped Yb^{3+}-doped $NaYF_4$ nanoparticle (proportions of the components' sizes are approximately represented).*

When excited at the ligand absorption, the primarily excited population of Yb^{3+} ions is at the surface (roughly 100% at the surface). Therefore, shorter lifetimes dominate at the ligand-based excitations while longer lifetimes do this under direct Yb^{3+} absorption band (960 nm) excitation. These considerations are confirmed in view of the measured lifetime of the pristine (oleylamine and oleic acid capped) 10% Yb^{3+}-doped $NaYF_4$ with 960 nm OPO excitation. At this excitation (direct excitation into the Yb^{3+} $^2F_{5/2}$ state), the decay time of oleylamine/oleic acid capped and organic chromophore capped nanoparticles is the same, as they are exposed to similar organic and hydrogenated impurities (except, obviously, the anthraquinone derivative ligand). It is also important to remark that the $^2F_{7/5} \rightarrow {}^2F_{7/2}$ Yb^{3+} emission at 10% doping is strongly affected by energy transfer processes between the Yb^{3+} ions themselves (hopping). The above results suggest that in the organic chromophore ligand-based excitation experiments, excitation diffuses from the surface towards the inside of the nanoparticles and quickly reaches the relatively protected Yb^{3+} ions inside the particle. The opposite occurs for the Yb^{3+} direct excitation experiment, when the excited population changes (statistically) from an initially (more protected) population diffusing to a more exposed Yb^{3+} with a shorter lifetime.

The decay curve of the organic chromophore ligand-capped Yb^{3+}-doped $NaYF_4$ nanoparticles at chromophore-based excitation significantly depends on the shape of the excitation pulse. While the OPO pulse excitation at 460 nm (with an average energy of ~ 600 μJ/pulse, 7 ns pulse width) causes a tri-exponential decay, the decay curve with a 405 nm diode excitation (80 mW) with pulse widths higher than 1 μs

can be described with two lifetimes, the components and its relative contribution changing with the pulse widths (see table 4.5 below).

Table 4.5. *Lifetime summary with different excitation pulse length (modulated 405 nm excitation, 80 mW peak power).*

Pulse length (μs)	τ_1	τ_1%	τ_2	τ_2%	τ_{av}
1	10.7 μs	26%	64.5 μs	74%	50.5 μs
100	15.3 μs	16%	113.6 μs	84%	98.2 μs
1000	17.1 μs	11%	137 μs	89%	124 μs

Table 4.5 shows that a longer excitation pulse on the organic chromophore causes an increase of the individual lifetime components (which is considerably more dominant in a longer excitation pulse) and an increase of the contribution of longer components, resulting in an increase of the average lifetime. These results are interpreted as a confirmation of the model explained above, and a direct observation of the energy migration towards the interior of the nanoparticle after sensitisation. Indeed, longer excitation pulses, although initially causing an increased population of surface-based excitation, allow for enhanced diffusion lengths towards the inside of the nanoparticle. Moreover, it can be employed to modulate the $^2F_{5/2} \rightarrow {}^2F_{7/2}$ lifetime, which can be of interest in applications. Figure 4.12 illustrates the lifetime fittings of the intensity decay curves regarding different excitation pulse lengths.

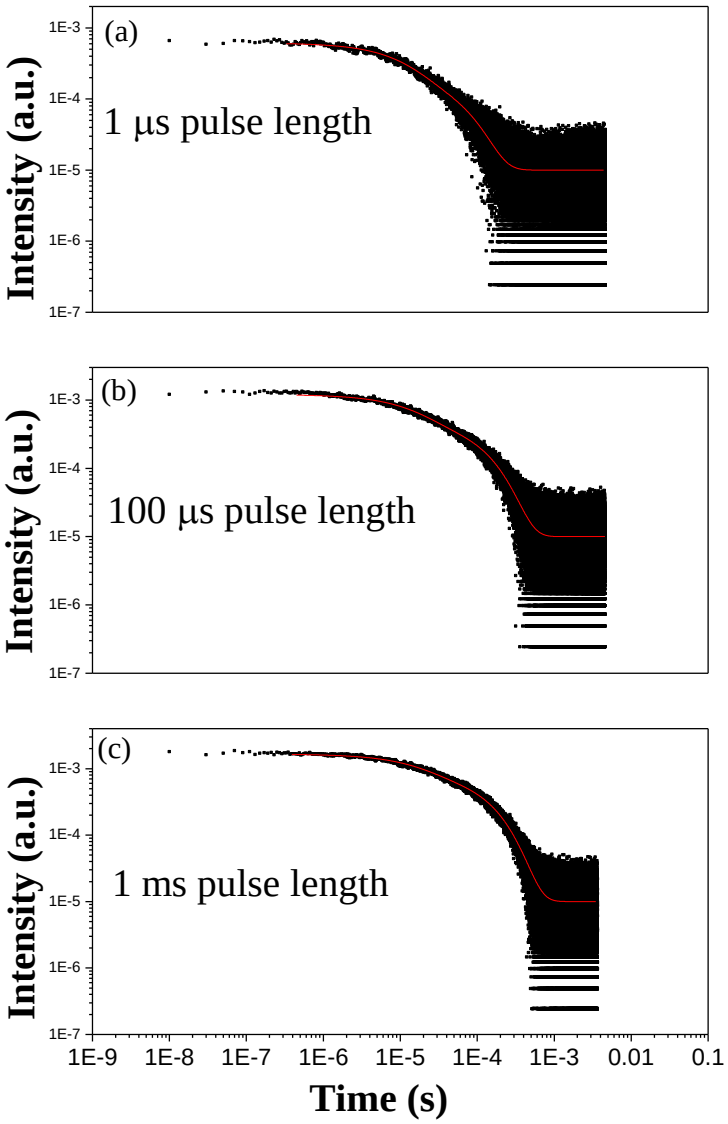

Figure 4.12 *Lifetime fittings of Yb^{3+} ions' intensity decay curve with 405 nm CW laser regarding different excitation pulse lengths* ***(a).*** *1 μs pulse length;* ***(b).*** *100 μs pulse length;* ***(c).****1 ms pulse length.*

4.4. Conclusions

Sub 10 nm 2-hydroxyperfluoroanthraquinone-sensitised Yb^{3+}-doped $NaYF_4$ nanoparticles in chloroform solution were prepared and investigated using a time-resolved spectroscopic method. Moderate sensitisation can be obtained with broad

visible light, ranging in wavelengths up to 600 nm. It has been observed that surface quenching-derived phenomena which causes a shorter average lifetime in the sensitised emission. It has been also observed that an energy migration phenomena leading to the excitation of Yb^{3+} inside the nanoparticle, is tuneable by varying the excitation pulse length.

4.5. References

[1] S. Sarkar, B. Meesaragandla, C. Hazra, V. Mahalingam, Sub-5 nm Ln^{3+}-doped $BaLuF_5$ nanocrystals: A platform to realize upconversion via interparticle energy transfer (IPET), *Advanced Materials*, **25** (2013) 856-860.

[2] G. Tian, Z. Gu, L. Zhou, W. Yin, X. Liu, L. Yan, S. Jin, W. Ren, G. Xing, S. Li, Y. Zhao, Mn^{2+} dopant-controlled synthesis of $NaYF_4$:Yb/Er upconversion nanoparticles for in vivo imaging and drug delivery, *Advanced Materials*, **24** (2012) 1226-1231.

[3] A. D. Ostrowski, E. M. Chan, D. J. Gargas, E. M. Katz, G. Han, P. J. Schuck, D. J. Milliron, B. E. Cohen, Controlled synthesis and single-particle imaging of bright, sub-10 nm lanthanide-doped upconverting nanocrystals, *ACS Nano*, **6** (2012) 2686-2692.

[4] F. Wang, R. Deng, J. Wang, Q. Wang, Y. Han, H. Zhu, X. Chen, X. Liu, Tuning upconversion through energy migration in core–shell nanoparticles, *Nature Materials*, **10** (2011) 968-973.

[5] Q. Liu, Y. Sun, T. Yang, W. Feng, C. Li, F. Li, Sub-10 nm hexagonal lanthanide-doped $NaLuF_4$ upconversion nanocrystals for sensitive bioimaging in vivo, *Journal of the American Chemical Society*, **133** (2011) 17122-17125.

[6] J. Zhang, C. M. Shade, D. A. Chengelis, S. Petoud, A strategy to protect and sensitize near-infrared luminescent Nd^{3+} and Yb^{3+}: organic tropolonate ligands for the sensitization of Ln^{3+}-doped $NaYF_4$ nanocrystals, *Journal of the American Chemical Society*, **129** (2007) 14834-14835.

[7] J. F. Suyver, A. Aebischer, S. García-Revilla, P. Gerner, H. U. Güdel, Anomalous power dependence of sensitized upconversion luminescence, *Physical Review B*, **71** (2005) 125123.

[8] X. Zhai, J. Li, S. Liu, X. Liu, D. Zhao, F. Wang, D. Zhang, G. Qin, W. Qin, Enhancement of 1.53 μm emission band in $NaYF_4$:Er^{3+}, Yb^{3+}, Ce^{3+} nanocrystals for polymer-based optical waveguide amplifiers, *Optical Materials Express*, **3** (2013) 270-277.

[9] X. Liu, Y. Chi, G. Dong, E. Wu, Y. Qiao, H. Zeng, J. Qiu, Optical gain at 1550 nm from colloidal solution of Er^{3+}-Yb^{3+} codoped $NaYF_4$ nanocubes, *Optics Express*, **17** (2009) 5885-5890.

[10] E. R. Trivedi, S. V. Eliseeva, J. Jankolovits, M. M. Olmstead, S. Petoud, V. L. Pecoraro, Highly emitting near-infrared lanthanide "encapsulated sandwich" metallacrown complexes with excitation shifted toward lower energy, *Journal of the American Chemical Society*, **136** (2014) 1526-1534.

[11] I. Hernández, Y. -X. Zheng, M. Motevalli, R. H. C. Tan, W. P. Gillin, P. B. Wyatt, Efficient sensitized emission in Yb (III) pentachlorotropolonate complexes, *Chemical Communications*, **49** (2013) 1933-1935.

[12] H. He, L. Si, Y. Zhong, M. Dubey, Iodized BODIPY as a long wavelength light sensitizer for the near-infrared emission of ytterbium (III) ion, *Chemical Communications*, **48** (2012) 1886-1888.

[13] X. -F. Yu, L. -D. Chen, M. Li, M. -Y. Xie, L. Zhou, Y. Li, Q. -Q. Wang, Highly efficient fluorescence of NdF_3/SiO_2 core/shell nanoparticles and the applications for in vivo NIR detection, *Advanced Materials*, **20** (2008) 4118-4123.

[14] J. Zhang, P. D. Badger, S. J. Geib, S. Petoud, Sensitization of near-infrared-emitting lanthanide cations in solution by tropolonate ligands, *Angewandte Chemie International Edition*, **44** (2005) 2508-2512.

[15] Q. Sun, X. Chen, Z. Liu, F. Wang, Z. Jiang, C. Wang, Enhancement of the upconversion luminescence intensity in Er^{3+} doped $BaTiO_3$ nanocrystals by codoping with Li^+ ions, *Journal of Alloys and Compounds*, **509** (2011) 5336-5340.

[16] I. Hernández, N. Pathumakanthar, P. B. Wyatt, W. P. Gillin, Cooperative infrared to visible up conversion in Tb^{3+}, Eu^{3+}, and Yb^{3+} containing polymers, *Advanced Materials*, **22** (2010) 5356-5360.

[17] S. W. Magennis, A. J. Ferguson, T. Bryden, T. S. Jones, A. Beeby, I. D. W. Samuel, Time-dependence of erbium (III) tris (8-hydroxyquinolate) near-infrared photoluminescence: implications for organic light-emitting diode efficiency, *Synthetic Metals*, **138** (2003) 463-469.

[18] G. E. Buono-Core, H. Li, B. Marciniak, Quenching of excited states by lanthanide ions and chelates in solution, *Coordination Chemistry Reviews*, **99** (1990) 55-87.

[19] G. Mancino, A. J. Ferguson, A. Beeby, N. J. Long, T. S. Jones, Dramatic increases in the lifetime of the Er^{3+} ion in a molecular complex using a perfluorinated imidodiphosphinate sensitizing ligand, *Journal of the American Chemical Society*, **127** (2005) 524-525.

[20] N. Gauthier, O. Raccurt, D. Imbert, M. Mazzanti, Efficient sensitization of Ln^{3+}-doped $NaYF_4$ nanocrystals with organic ligands, *Journal of Nanoparticle Research*, **15** (2013) 1-14.

[21] W. Zou, C. Visser, J. A. Maduro, M. S. Pshenichnikov, J. C. Hummelen, Broadband dye-sensitized upconversion of near-infrared light, *Nature Photonics*, **6** (2012) 560-564.

[22] S. Li, X. Zhang, Z. Hou, Z. Cheng, P. Ma, J. Lin, Enhanced emission of ultra-small-sized LaF_3:RE^{3+} (RE = Eu, Tb) nanoparticles through 1,2,4,5-benzenetetracarboxylic acid sensitization, *Nanoscale*, **4** (2012) 5619-5626.

[23] Y. Peng, H. Ye, Z. Li, M. Motevalli, I. Hernandez, W. P. Gillin, P. B. Wyatt, Visible-range sensitization of Er^{3+}-based infrared emission from perfluorinated 2-acylphenoxide complexes, *The Journal of Physical Chemistry Letters*, **5** (2014) 1560-1563.

[24] H. Ye, Z. Li, Y. Peng, C. Wang, T. Li, Y. Zheng, A. Sapelkin, G. Adamopoulos, I. Hernández, P. B. Wyatt, W. P. Gillin, Organo-erbium systems for optical amplification at telecommunications wavelengths, *Nature Materials*, **13** (2014) 382-386.

[25] F. Wang, J. Wang, X. Liu, Direct evidence of a surface quenching effect on size-dependent luminescence of upconversion nanoparticles, *Angewandte Chemie*, **122** (2010) 7618-7622.

[26] Y. Peng, Synthesis and characterization of highly fluorinated lanthanide complexes for near-infrared applications, School of Biological and Chemical

Science, School of Physics and Astronomy, Queen Mary University of London, London, 2014.

[27] C. Reinhard, H. U. Güdel, High-resolution optical spectroscopy of $Na_3[Ln(dpa)_3]\cdot 13H_2O$ with Ln = Er^{3+}, Tm^{3+}, Yb^{3+}, *Inorganic Chemistry*, **41** (2002) 1048-1055.

[28] F. R. Gonçalves e Silva, O. L. Malta, C. Reinhard, H. -U. Güdel, C. Piguet, J. E. Moser, J. -C. G. Bünzli, Visible and near-infrared luminescence of lanthanide-containing dimetallic triple-stranded helicates: energy transfer mechanisms in the Sm^{III} and Yb^{III} molecular edifices, *The Journal of Physical Chemistry A*, **106** (2002) 1670-1677.

[29] G. K. Liu, M. P. Jensen, P. M. Almond, Systematic behavior of charge-transfer transitions and energy level variation in soft donor complexes of the trivalent lanthanides, *The Journal of Physical Chemistry A*, **110** (2006) 2081-2088.

[30] H. Lu, W. P. Gillin, I. Hernández, Concentration dependence of the up- and down-conversion emission colours of Er^{3+}-doped Y_2O_3: a time-resolved spectroscopy analysis, *Physical Chemistry Chemical Physics*, **16** (2014) 20957-20963.

Chapter 5: Efficient sensitisation of $Yb(F\text{-}TPIP)_3$ with $Zn(F\text{-}BTZ)_2$ chromophore

5.1. Background and introduction

Lanthanide doped NIR emitting materials have been widely investigated due to the potential applications in the field of super resolution [1], biology [2] and waveguide amplifiers [3]. The advantages of the NIR light (especially in the ~1000 nm range) absorption and/or emission have been described in chapter 4: NIR light has less scattering effect and higher penetration inside the body tissue compared with UV or visible light [4, 5]. Previous research has mainly focused on the lanthanide doped glasses [6-8], oxides [9-12] and nanoparticles [13-16]. Many kinds of probes, biological tissues and waveguides have already been developed based on the previous systems [1, 2]. However, there are some drawbacks, such as concentration quench and the need for high excitation power density, which are difficult to overcome due to the crucial energy transfer distance and small cross section area of the lanthanide ions separately [17]. Recent research shows that the organic lanthanide complex has the possibility of increasing the lanthanide doping concentration without significantly decreasing the emission intensity or lifetime [18, 19], as the lanthanide ions are protected by the organic molecules. More importantly, the organic chromophore can act as a sensitiser, transferring energy from the organic chromophore to the corresponding energy states of the lanthanide ions [19, 20]. Therefore, the lanthanide emission intensity can be largely improved

due to the broad absorption wavelength range and large absorption cross section of the organic chromophore.

However, there are still some drawbacks for the reported lanthanide complexes, among which there are three main problems. Firstly, the reported lanthanide emitters have considerably short lifetimes (in the order of tens of μs) and/or low emission intensity, which is due to the quenchers such as O–H, C–H and N–H chemical bonds typically found in organic chromophore, solvents and moisture [21]. The excited energy states of lanthanides match the 3^{rd} to 5^{th} vibrational energy level of these chemical bonds, therefore, a non-radiative decay process would be more likely to happen than a radiative decay [19]. Secondly, the sensitisation is still not efficient, which may due to a number of reasons, such as the mismatch between excited energy states of chromophores and lanthanides and/or the insufficient intersystem crossing between the organic chromophore's singlet and triplet states, as it is understood that intersystem crossing favours the energy transfer processes [22]. Lastly, the majority of the reported organic lanthanide complexes are not thermally stable and cannot be physically evaporated under vacuum to make optical quality thin films [18], hence the processability of these materials is low for making a waveguide amplifier.

For the first main concern, fluorination has proved to be an effective way to reduce the organic chromophore quenching by lowering the energy level of vibrational modes of the chemical bonds. For example, the reported lifetimes of Er^{3+}/Yb^{3+} ions have been increased from tens of μs up to a few ms with fluorination of the Er^{3+}/Yb^{3+} containing organic complexes [23, 24]. Together with fluorination, the

other two problems mentioned above have been overcome recently by co-evaporating erbium(III) tetrakis(pentafluorophenyl) imidodiphosphinate, Er(F-TPIP)$_3$ and Zn(F-BTZ)$_2$ under vacuum using the organic vapour deposition technique, making optical quality thin films [18]. A great sensitisation of the Er^{3+} ion for the 1.5 μm telecommunication wavelength ($^4I_{13/2} \rightarrow {}^4I_{15/2}$) was demonstrated.

As noted above, the ~1000 nm NIR wavelength is an interesting telecommunication wavelength. It is desirable to demonstrate the efficient sensitisation of Yb^{3+} ions, which are doped into the thermally evaporated organic optical quality thin films. It should be mentioned that the ~1000 nm NIR emission, which is due to the $^4I_{11/2} \rightarrow {}^4I_{15/2}$ transition of the Er^{3+} ion, is very weak in the mentioned Er(F-TPIP)$_3$ co-doped with Zn(F-BTZ)$_2$ system. The reason is not clear, which may due to the rapid non-radiative transition through $^4I_{11/2} \rightarrow {}^4I_{13/2}$, or the excited $^4I_{11/2}$ state is more sensitive to the vibrational energy levels of the existing water molecules than the $^4I_{13/2}$ excited state.

In this chapter, a strong ~1000 nm NIR emission ($^2F_{5/2} \rightarrow {}^2F_{7/2}$) from Yb^{3+} ions is demonstrated by co-evaporating Yb(F-TPIP)$_3$ and Zn(F-BTZ)$_2$ onto a glass substrate under vacuum. Figure 5.1 below shows the emission spectrum of the co-evaporated Yb(F-TPIP)$_3$ and Zn(F-BTZ)$_2$ film measured under a 405 nm CW laser. Also, a physical model was built explaining the sensitisation of Yb^{3+} ions through the Zn(F-BTZ)$_2$ chromophore and a full characterisation of Yb(F-TPIP)$_3$ and Zn(F-BTZ)$_2$ co-evaporated film is applied, regarding different doping concentrations. The best sensitisation of Yb^{3+} ions with the Zn(F-BTZ)$_2$ chromophore is two orders higher compared with the intrinsic excitation region (900-1000 nm) of Yb^{3+} ions.

And the measured longest lifetime of 980 nm emission of the Yb^{3+} ion in the co-doped film is 1.04 ms, which reaches 79% quantum yield (1.31 ms is the recommended value of the intrinsic lifetime of Yb^{3+} in aqueous solutions of coordination compounds [25]).

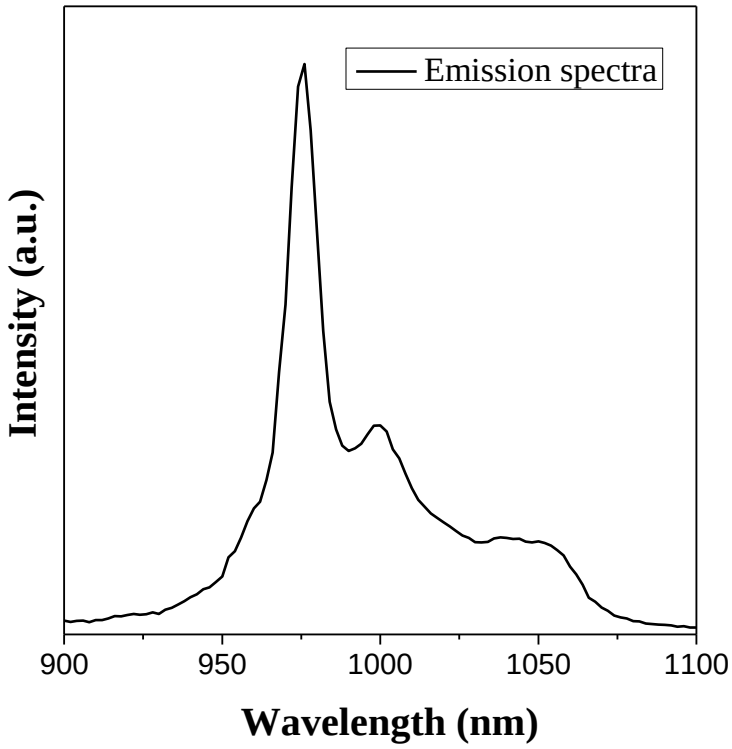

Figure 5.1. *Emission spectrum of co-evaporated $Yb(F\text{-}TPIP)_3$ and $Zn(F\text{-}BTZ)_2$ film measured with 405 nm CW laser.*

5.2. Instruments and experiments

5.2.1. Film deposition

$Yb(F\text{-}TPIP)_3$ was chemically synthesised, dried under vacuum (10^{-2} mbar) and then sublimated under vacuum (10^{-7} mbar). The detailed procedures of these three

processes are described in chapter 2. After purification (sublimation), $Yb(F\text{-}TPIP)_3$ was co-evaporated with $Zn(F\text{-}BTZ)_2$, which was also purified according to the same processes above. The $Yb(F\text{-}TPIP)_3$ and $Zn(F\text{-}BTZ)_2$ co-doped film was deposited using the conventional organic vapour deposition technique, which is desirable for achieving pure and optical quality material required for the waveguide amplifier. Details of the chemical vapour deposition technique and the film deposition procedures are all described in chapter 2. The detailed deposition parameters during the co-evaporation experiment for different Yb^{3+} ion concentration samples is given in table 5.1 below.

Table 5.1. *Parameters of organic chemical vapour deposition of $Yb(F\text{-}TPIP)_3$ and $Zn(F\text{-}BTZ)_2$ thin films.*

Sample	**Deposition rate**	**Thickness**	**Chamber pressure**
50 nm $Yb(F\text{-}TPIP)_3$ 200 nm $Zn(F\text{-}BTZ)_2$	0.3 Å/s 1.2 Å/s	489 Å 2000 Å	5.30×10^{-7} mbar
100 nm $Yb(F\text{-}TPIP)_3$ 200 nm $Zn(F\text{-}BTZ)_2$	0.5 Å/s 1.0 Å/s	1005 Å 2000 Å	6.05×10^{-7} mbar
200 nm $Yb(F\text{-}TPIP)_3$ 200 nm $Zn(F\text{-}BTZ)_2$	1.0 Å/s 1.0 Å/s	1994 Å 2000 Å	5.70×10^{-7} mbar
300 nm $Yb(F\text{-}TPIP)_3$ 200 nm $Zn(F\text{-}BTZ)_2$	1.5 Å/s 1.0 Å/s	2990 Å 2000 Å	5.50×10^{-7} mbar

5.2.2. Optical characterisation

405 nm and 975 nm CW lasers, electrically modulated by a square wave generator at a frequency of 123 Hz, were used to measure the lifetime as well as the power dependent sensitisation of $Yb(F\text{-}TPIP)_3$ powder and/or co-evaporated $Yb(F\text{-}TPIP)_3$ and $Zn(F\text{-}BTZ)_2$ film. For the lifetime measurements, the intensity decay curve is recorded by the Oscilloscope. For the power dependent sensitisation measurements, the emission intensity was recorded by the lock-in amplifier.

The xenon lamp, together with a monochromator was used as the light source to measure the excitation spectra of the co-doped $Yb(F\text{-}TPIP)_3$ and $Zn(F\text{-}BTZ)_2$ films within both visible and NIR regions. The monochromatic light was modulated by a chopper at a frequency of 173 Hz. The emission intensity was recorded by the lock-in amplifier. The specific experimental set up of lifetime measurements, power dependent sensitisation and excitation spectra measurements can be found in chapter 2.

5.3. Lifetime measurements

Lifetime is one of the key fundamental characters of lanthanides, especially for the design of high emitting organic materials and devices [25]. The reported lifetime of lanthanides (such as Er^{3+} and Yb^{3+}) containing an organic complex is much shorter than their intrinsic lifetime, even with fluorination or chlorination [23, 24]. Therefore, the emission intensity is considerably low. Furthermore, short lifetime means low energy transfer quantum efficiency. So, it has been practically

interesting to maximise the lifetime of lanthanide complexes and the overall quantum yield, Q. Importantly, for Er^{3+} and Yb^{3+} ions containing materials, longer lifetimes could increase the probability of population inversion, which is essential for obtaining optical gain for telecommunication applications.

In the literature, the reported lifetime of $Yb(F\text{-}TPIP)_3$ powder was 582 μs (measured under N_2 atmosphere) [23]. And the maximum 1111 μs lifetime was obtained in a $Yb(F\text{-}TPIP)_3$ dissolved CD_3CN solvent with N_2 atmosphere protection, in which the condition of the interaction between Yb^{3+}-Yb^{3+} ions is assumed to be very limited [23]. In our experiments, similar experimental results were demonstrated. The lifetime of $Yb(F\text{-}TPIP)_3$ powder/film was investigated systematically regarding different synthesise conditions, film growing environments and Yb^{3+} doping concentrations.

As $Yb(F\text{-}TPIP)_3$ powder was precipitated from the ethanol solvent after the chemical reaction (see chapter 2 for synthesis details), there will be some alcohol molecules remaining. The synthesised $Yb(F\text{-}TPIP)_3$ powder was heated under vacuum (10^{-2} mbar) at a temperature of 150 °C for one night in order to remove the alcohol and water molecules. The 1030 nm emission intensity decay curve (black one) measured with a 975 nm CW laser is given in figure 5.2 below. The fitted lifetime is 205 μs, which is shorter compared to the literature reported value (582 μs) [23]. It should be mentioned that both the measured and literature reported lifetimes are considerably shorter compared with the reported intrinsic lifetime of the Yb^{3+} ion (1.31 ms). There are several possible reasons for this: (1) there are still traces of alcohol and/or water molecules (the possible quenches), which are difficult

to be completely remove; (2) there are some impurities, such as the unreacted organic ligand; (3) the possible concentration quenching between Yb^{3+}-Yb^{3+} ions.

In order to make pure and impurity molecule free $Yb(F\text{-}TPIP)_3$, the dried $Yb(F\text{-}TPIP)_3$ powder was sublimated under vacuum (10^{-7} mbar). The detailed sublimation process is introduced in chapter 2. The lifetime of $Yb(F\text{-}TPIP)_3$ powder after sublimation is 522 μs, which is also shown in figure 5.2 (blue curve). It actually proves that sublimation is a necessary process in our lifetime measurement experiments. All lifetimes mentioned later in this chapter were measured with samples after sublimation.

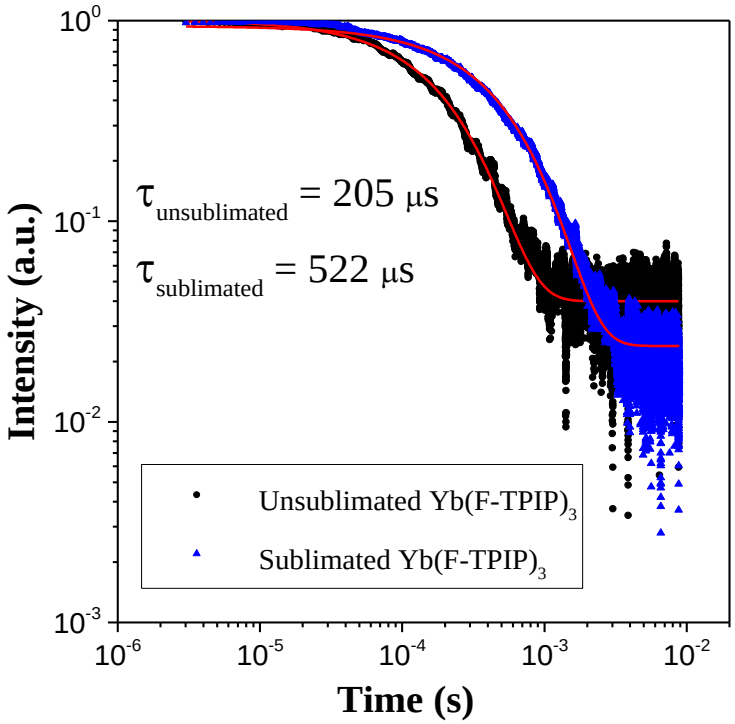

Figure 5.2. *1030 nm intensity decay curves of both unsublimated and sublimated $Yb(F\text{-}TPIP)_3$ powder measured with 980 nm CW laser.*

Sublimated $Yb(F\text{-}TPIP)_3$ and $Zn(F\text{-}BTZ)_2$ powder was used for the co-doped film deposition. In the co-doped film, $Zn(F\text{-}BTZ)_2$ acts as a sensitiser, which has a big cross-section and can transfer the excited energy to the neighbouring Yb^{3+} ions (the mechanism of energy transfer is discussed in subsection 5.4). Also, $Zn(F\text{-}BTZ)_2$ was used to dilute the total Yb^{3+} ions concentration. It should be noted that two different film deposition conditions were investigated for the 200 nm $Yb(F\text{-}TPIP)_3$ co-doped with 200 nm $Zn(F\text{-}BTZ)_2$ film. One was deposited just with normal 10^{-7} mbar vacuum. The other one was deposited under 10^{-7} mbar vacuum with a cold finger which was filled with liquid N_2. The difference is that the cold finger can 'freeze' the water molecules (quenching centres) during the deposition processes. The gas composition was analysed with the residual gas analyser (RGA). As shown in figure 5.2 (a), the amount of water molecules was reduced by an order of magnitude with the cold finger. Interestingly, the lifetime of the co-doped $Yb(F\text{-}TPIP)_3$ and $Zn(F\text{-}BTZ)_2$ film was extended from 753 μs to 1.044 ms after using the cold finger, which does suggest the water molecules play a crucial role as a quenching centre of lanthanide ions even under 10^{-7} mbar vacuum. The lifetime of the co-doped film was measured with the 405 nm CW laser and the fittings are shown in figure 5.3 (b) below.

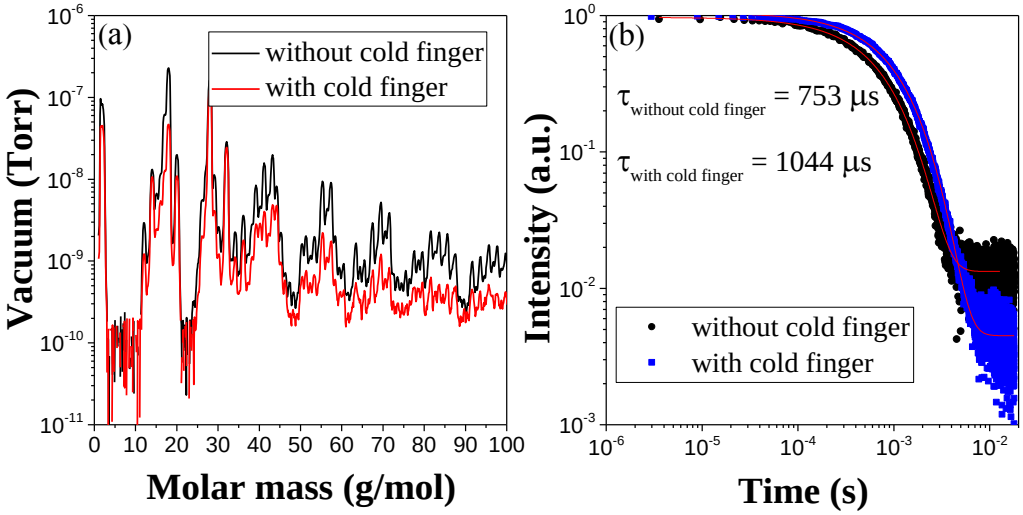

Figure 5.3 (a). *Impurity levels of deposition vacuum with and without cold finger;* ***(b).*** *1030 nm intensity decay curves and lifetime fittings of 200 nm Yb(F-TPIP)$_3$ and 200nm Zn(F-BTZ)$_2$ co-doped film deposited with and without cold finger excited with 405 nm CW laser.*

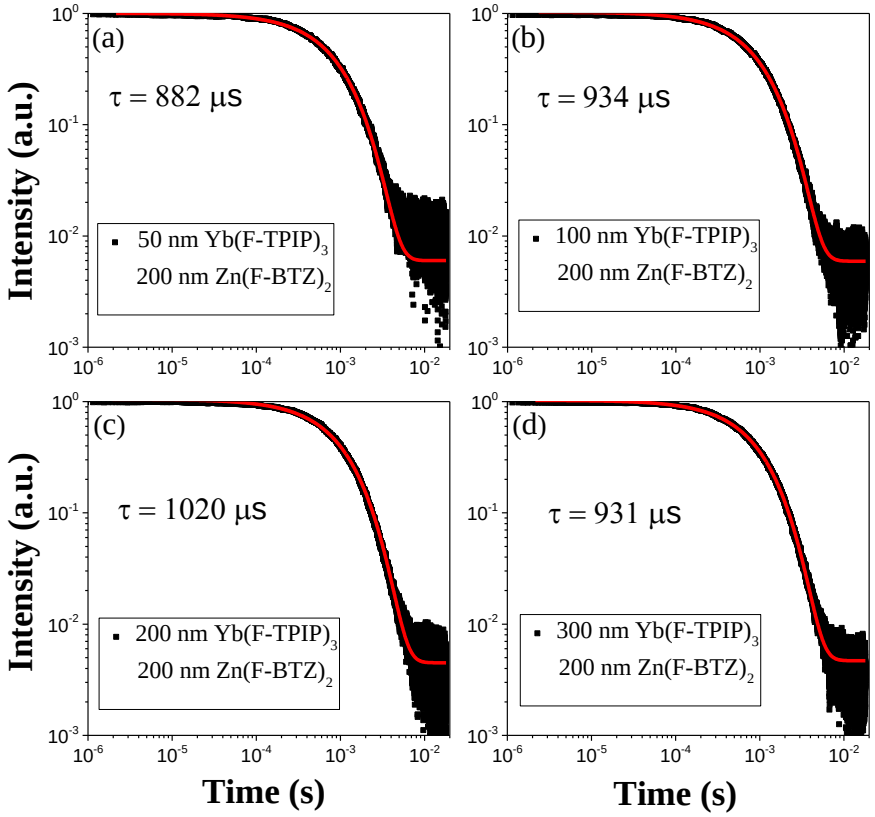

Figure 5.4 *1030 nm intensity decay curves of* ***(a).*** *50 nm Yb(F-TPIP)$_3$ co-doped with 200 nm Zn(F-BTZ)$_2$;* ***(b).*** *100 nm Yb(F-TPIP)$_3$ co-doped with 200 nm Zn(F-BTZ)$_2$;* ***(c).*** *200 nm Yb(F-TPIP)$_3$ co-doped with 200 nm Zn(F-BTZ)$_2$;* ***(d).*** *300 nm Yb(F-TPIP)$_3$ co-doped with 200 nm Zn(F-BTZ)$_2$, excited at 405 nm CW laser.*

In order to investigate the concentration quenching effect on the lifetime of Yb^{3+} ions, a series of film samples were prepared with different Yb^{3+} ion concentrations. The co-evaporated thickness of Yb(F-TPIP)$_3$/Zn(F-BTZ)$_2$ was 50 nm/200 nm, 100 nm/200 nm, 200 nm/200 nm and 300 nm/200 nm separately. The measured lifetimes were 882 µs, 934 µs, 1020 µs and 931 µs separately for the above samples as illustrated in figure 5.4 above. Lifetimes are consistent (~941 µs) and within the 10% system measurement error for different Yb^{3+} doping concentration samples. This is also consistent with the value (1111 µs) reported for the Yb(F-TPIP)$_3$

dissolved CD_3CN solvent. The averaged quantum yield of $Yb(F\text{-}TPIP)_3$ co-doped $Zn(F\text{-}BTZ)_2$ is

$$Q = \frac{\tau}{\tau_{rad}} = 71\% \quad (5.1)$$

where τ (941 μs) is the measured lifetime of the excited state and τ_{rad} (1.31 ms) is the lifetime in absence of any non-radiative process.

5.4. Sensitisation characterisation

5.4.1. Excitation spectra

It is well known that sensitisation is one of the key factors for judging the energy transfer efficiency. Better sensitisation means higher emission intensity as well as more chance to get the optical gain for the telecommunication applications. Thus, it is important to understand the sensitisation processes and investigate the best sensitisation conditions for the co-doped $Yb(F\text{-}TPIP)_3$ and $Zn(F\text{-}BTZ)_2$ system.

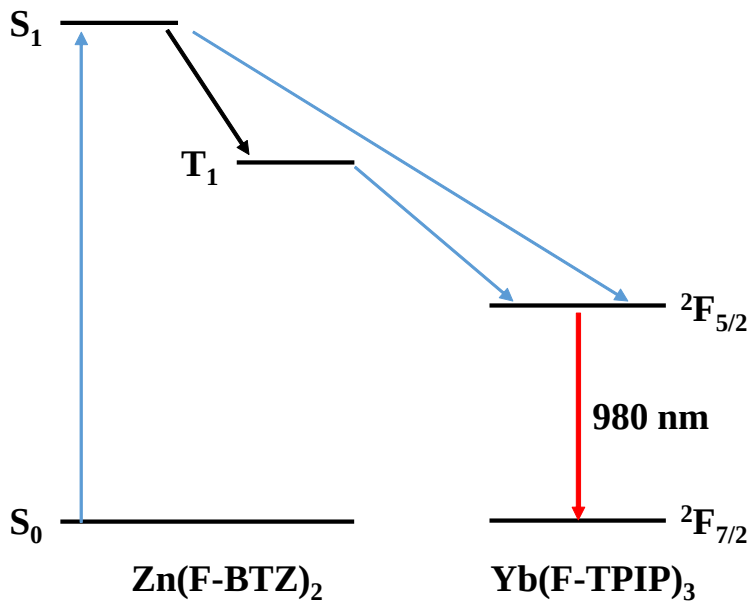

Figure 5.5. *Jablonski diagram for energy transfer from Zn(F-BTZ)$_2$ to the encapsulated Yb^{3+} ions.*

The energy transfer process from the excited states of the Zn(F-BTZ)$_2$ chromophore to the excited state of encapsulated Yb^{3+} ions (sensitisation) is illustrated in figure 5.5 above. In detail, the Zn(F-BTZ)$_2$ chromophore can be excited from the ground state S_0 to the singlet state S_1 under broad range light (350–500 nm) absorptions [26]. Part of the excitation of state S_1 will decay rapidly to the ground state, giving luminescence. And some excitations from singlet state S_1 can be transferred to the corresponding energy state of Yb^{3+} ions directly where a change of spin number is required [22]. More importantly, some excitations from state S_1 can decay to the lower-lying triplet state T_1 via inter-system crossing process. It is understood that triplet state T_1 is more efficient than singlet state S_1 for coupling with the multiplets of rare earth ions [22]. In this system, fluorination of benzothiazole ligands favours the inter-system crossing, which is due to the enhanced spin-orbit interaction caused

by the higher *Z* factor of fluorine compared with hydrogen [18]. So, fluorination enhances the energy transfer from intermediate triplet state T_1 to the excited states of Yb^{3+} ions. Therefore, an efficient sensitisation from the $Zn(F\text{-}BTZ)_2$ chromophore to $Yb(F\text{-}TPIP)_3$ could be expected.

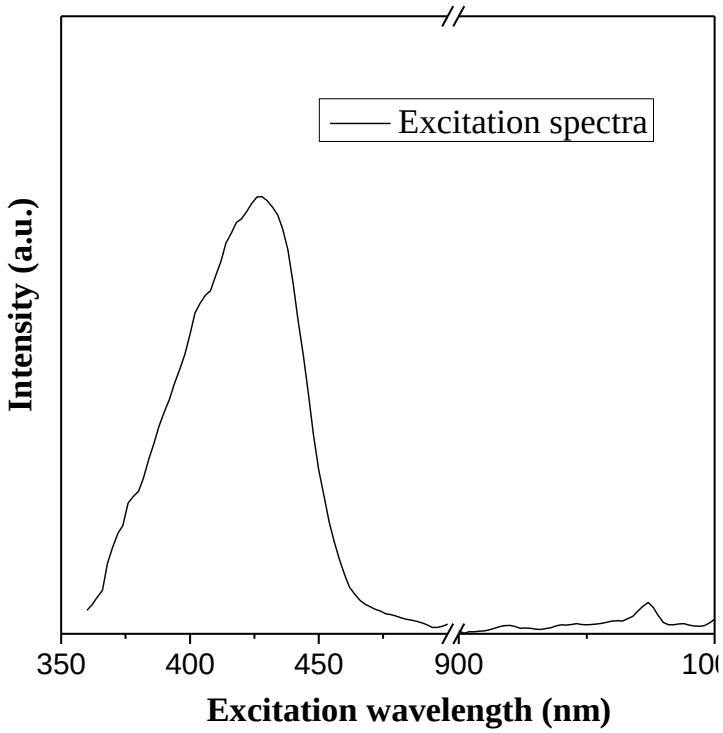

Figure 5.6. *Excitation spectrum of 200 nm $Yb(F\text{-}TPIP)_3$ co-doped 200 nm $Zn(F\text{-}BTZ)_2$ with xenon lamp.*

All four co-doped $Zn(F\text{-}BTZ)_2$ and $Yb(F\text{-}TPIP)_3$ film samples were made under identical deposition conditions, regarding different thickness of $Yb(F\text{-}TPIP)_3$. The detailed deposition conditions of these four film samples is given in the film deposition discussion above. Figure 5.6 is the excitation spectrum of 200 nm $Yb(F\text{-}TPIP)_3$ co-doped $Zn(F\text{-}BTZ)_2$ film under both visible and near infrared light excitation using the xenon lamp. As shown, the integrated excitation of Yb(F-

TPIP)$_3$ under the visible region is a hundred times bigger than the excitation under the 950-1000 nm region, which is the intrinsic excitation region of Yb^{3+} ions. Interestingly, the excitation spectra is similar to the absorption spectra of Zn(F-BTZ)$_2$ [26]. Thus, it can be confirmed that the sensitisation during the visible light range is due to the energy transfer from Zn(F-BTZ)$_2$ to Yb(F-TPIP)$_3$.

5.4.2. Power dependent excitation

In order to find the best sensitisation condition, the co-evaporated Yb(F-TPIP)$_3$ and Zn(F-BTZ)$_2$ films were characterised as a function of Yb(F-TPIP)$_3$ doping concentration. The amount of Zn(F-BTZ)$_2$ chromophore was kept constant to make sure the excited chromophore was the same under the same excitation power density, while different amounts of Yb(F-TPIP)$_3$ were used for estimating the best doping ratio. For the characterisation, two important issues need to be considered: (1) sensitisation may not change linearly with a 405 nm excitation power density, as the Zn(F-BTZ)$_2$ chromophore can get saturated at the high power density region; (2) the Zn(F-BTZ)$_2$ chromophore has a strong absorption at 405 nm wavelength range, thus there is a probability that the 405 nm light cannot penetrate the whole film. Based on these considerations, sensitisation needs to be characterised with regard to different power density. The power density range used in the experiment was from 12.88 to 234.19 mW/cm^2 and 117.10 to 749.41 mW/cm^2 for 405 nm and 975 nm CW lasers respectively.

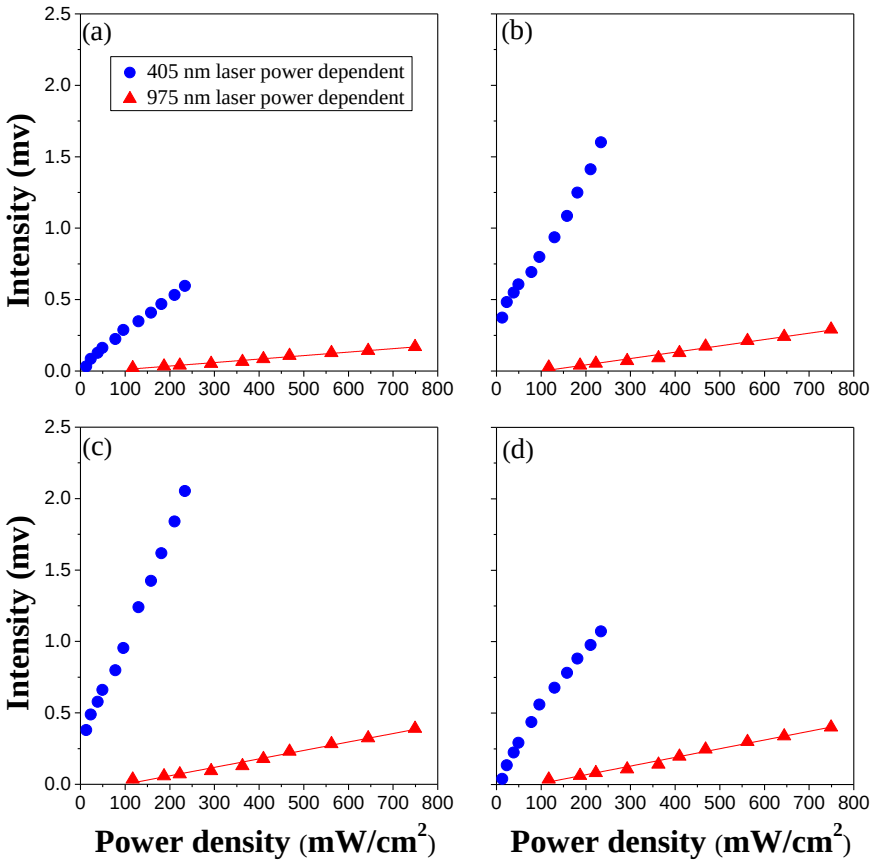

Figure 5.7 *405 nm and 975 nm power dependent sensitisation characterisation of Yb(F-TPIP)$_3$ and Zn(F-BTZ)$_2$ co-doped films with different Yb^{3+} concentrations* ***(a).*** *50 nm Yb(F-TPIP)$_3$ co-doped with 200 nm Zn(F-BTZ)$_2$;* ***(b).*** *100 nm Yb(F-TPIP)$_3$ co-doped with 200 nm Zn(F-BTZ)$_2$;* ***(c).*** *200 nm Yb(F-TPIP)$_3$ co-doped with 200 nm Zn(F-BTZ)$_2$;* ***(d).*** *300 nm Yb(F-TPIP)$_3$ co-doped with 200 nm Zn(F-BTZ)$_2$.*

Figure 5.7 above shows the 405 nm and 975 nm power dependent excitations for the 1030 nm emission intensity of the co-doped films with different Yb(F-TPIP)$_3$ and Zn(F-BTZ)$_2$ thickness ratios. As shown in figure 5.7 (a) to 5.7 (d), the 1030 nm emission intensity increases linearly with increasing the 975 nm power density (red symbol). And under the same 975 nm excitation power density, the higher the Yb^{3+} concentration, the larger the emission intensity. However, this is not the case with the 405 nm excitation. Under the same 405 nm excitation power density, the largest

1030 nm emission intensity happens with the 200 nm Yb(F-TPIP)$_3$ co-doped with 200 nm Zn(F-BTZ)$_2$ sample. That is to say, for the same amount of excited Zn(F-BTZ)$_2$ chromophore, there is a best Yb^{3+} concentration. When Yb^{3+} concentration is low (50 nm and 100 nm Yb(F-TPIP)$_3$ samples), some of the excited energy of the chromophore is wasted, and when Yb^{3+} concentration is high (300 nm Yb(F-TPIP)$_3$ sample), the average distance between the chromophore molecule and the Yb^{3+} is longer, therefore, the energy transfer efficiency is lower. Considering that the 1030 nm emission intensity changes linearly with the 975 nm excitation power and Yb^{3+} concentration only, the 1030 nm emission intensity excited at 975 nm wavelength is used as a reference to characterise the sensitisation efficiency.

In the power density region from 100 to 300 mw/cm^2, using 975 nm excitation as a reference, the sensitisation with 405 nm excitation has been improved 14, 25, 26 and 12 times for the 50 nm, 100 nm, 200 nm and 300 nm thick Yb(F-TPIP)$_3$ samples respectively. Thus, the 200 nm Yb(F-TPIP)$_3$ co-evaporated with 200 nm Zn(F-BTZ)$_2$ is recommended as the best doping ratio.

5.5. Conclusion

In this chapter, a systematic investigation of lifetime and sensitisation of Yb(F-TPIP)$_3$ co-doped Zn(F-BTZ)$_2$ films in relation to different Yb^{3+} ions concentrations is demonstrated. It is found that the lifetime of Yb^{3+} within the co-doped system remains constant regardless of the Yb^{3+} ion concentration, which opens the way for increasing the lanthanide doping concentration without decreasing the emission intensity or quantum yield. The best integrated sensitisation over the visible

wavelength range is found with the 200 nm $Yb(F\text{-}TPIP)_3$ co-doped with 200 nm $Zn(F\text{-}BTZ)_2$ film, which is more than two orders bigger than the intrinsic sensitisation. The sensitisation efficiency is relevant to the average distance between Yb^{3+} ions and organic sensitisers, which gives useful information for designing potential materials for the application of the 980 nm waveguide amplifier.

5.6. Reference

[1] S. V. Eliseeva, J. -C. G. Bünzli, Lanthanide luminescence for functional materials and bio-sciences, *Chemical Society Reviews*, **39** (2010) 189-227.

[2] J. -C. G. Bünzli, Lanthanide luminescence for biomedical analyses and imaging, *Chemical Reviews*, **110** (2010) 2729-2755.

[3] X. Zhai, J. Li, S. Liu, X. Liu, D. Zhao, F. Wang, D. Zhang, G. Qin, W. Qin, Enhancement of 1.53 μm emission band in $NaYF_4:Er^{3+}$, Yb^{3+}, Ce^{3+} nanocrystals for polymer-based optical waveguide amplifiers, *Optical Materials Express*, **3** (2013) 270-277.

[4] G. Tian, Z. Gu, L. Zhou, W. Yin, X. Liu, L. Yan, S. Jin, W. Ren, G. Xing, S. Li, Y. Zhao, Mn^{2+} dopant-controlled synthesis of $NaYF_4$:Yb/Er upconversion nanoparticles for in vivo imaging and drug delivery, *Advanced Materials*, **24** (2012) 1226-1231.

[5] X. -F. Yu, L. -D. Chen, M. Li, M. -Y. Xie, L. Zhou, Y. Li, Q. -Q. Wang, Highly efficient fluorescence of NdF_3/SiO_2 core/shell nanoparticles and the applications for in vivo NIR detection, *Advanced Materials*, **20** (2008) 4118-4123.

[6] R. Balda, A. J. Garcia-Adeva, J. Fernández, J. M. Fdez-Navarro, Infrared-to-visible upconversion of Er^{3+} ions in GeO_2-PbO-Nb_2O_5 glasses, *Journal of the Optical Society America B*, **21** (2004) 744-752.

[7] J. Qiu, P. G. Kazanski, J. Si, K. Miura, T. Mitsuyu, K. Hirao, A. L. Gaeta, Memorized polarization-dependent light scattering in rare-earth-ion-doped glass, *Applied Physics Letters*, **77** (2000) 1940-1942.

[8] P. S. Golding, S. D. Jackson, T. A. King, M. Pollnau, Energy transfer processes in Er^{3+}-doped and Er^{3+}, Pr^{3+}-codoped ZBLAN glasses, *Physical Review B*, **62** (2000) 856-864.

[9] I. Etchart, A. Huignard, M. Bérard, M. N. Nordin, I. Hernández, R. J. Curry, W. P. Gillin, A. K. Cheetham, Oxide phosphors for efficient light upconversion: Yb^{3+} and Er^{3+} co-doped Ln_2BaZnO_5 (Ln = Y, Gd), *Journal of Materials Chemistry*, **20** (2010) 3989-3994.

[10] F. Vetrone, J. -C. Boyer, J. A. Capobianco, A. Speghini, M. Bettinelli, Concentration-dependent near-infrared to visible upconversion in nanocrystalline and bulk Y_2O_3: Er^{3+}, *Chemistry of Materials*, **15** (2003) 2737-2743.

[11] J. A. Capobianco, F. Vetrone, J. C. Boyer, A. Speghini, M. Bettinelli, Enhancement of red emission ($^4F_{9/2} \rightarrow {}^4I_{15/2}$) via upconversion in bulk and nanocrystalline cubic Y_2O_3: Er^{3+}, *The Journal of Physical Chemistry B*, **106** (2002) 1181-1187.

[12] J. A. Capobianco, F. Vetrone, T. D'Alesio, G. Tessari, A. Speghini, M. Bettinelli, Optical spectroscopy of nanocrystalline cubic Y_2O_3:Er^{3+} obtained by combustion synthesis, *Physical Chemistry Chemical Physics*, **2** (2000) 3203-3207.

[13] J. Zhao, Z. Lu, Y. Yin, C. McRae, J. A. Piper, J. M. Dawes, D. Jin, E. M. Goldys, Upconversion luminescence with tunable lifetime in $NaYF_4$:Yb, Er nanocrystals: role of nanocrystal size, *Nanoscale*, **5** (2013) 944-952.

[14] J. Zhao, D. Jin, E. P. Schartner, Y. Lu, Y. Liu, A. V. Zvyagin, L. Zhang, J. M. Dawes, P. Xi, J. A. Piper, E. M. Goldys, T. M. Monro, Single-nanocrystal sensitivity achieved by enhanced upconversion luminescence, *Nature Nanotechnology*, **8** (2013) 729-734.

[15] J. Wang, H. Song, W. Xu, B. Dong, S. Xu, B. Chen, W. Yu, S. Zhang, Phase transition, size control and color tuning of $NaREF_4$:Yb^{3+}, Er^{3+} (RE = Y, Lu) nanocrystals, *Nanoscale*, **5** (2013) 3412-3420.

[16] F. Wang, Y. Han, C. S. Lim, Y. Lu, J. Wang, J. Xu, H. Chen, C. Zhang, M. Hong, X. Liu, Simultaneous phase and size control of upconversion nanocrystals through lanthanide doping, *Nature*, **463** (2010) 1061-1065.

[17] I. Hernández, N. Pathumakanthar, P. B. Wyatt, W. P. Gillin, Cooperative infrared to visible up conversion in Tb^{3+}, Eu^{3+}, and Yb^{3+} containing polymers, *Advanced Materials*, **22** (2010) 5356-5360.

[18] H. Ye, Z. Li, Y. Peng, C. Wang, T. Li, Y. Zheng, A. Sapelkin, G. Adamopoulos, I. Hernández, P. B. Wyatt, W. P. Gillin, Organo-erbium systems for optical amplification at telecommunications wavelengths, *Nature Materials*, **13** (2014) 382-386.

[19] I. Hernández, R. H. C. Tan, J. M. Pearson, P. B. Wyatt, W. P. Gillin, Nonradiative de-excitation mechanisms in long-lived erbium (III) organic compounds $Er_xY_{1-x}[(p\text{-}CF_3\text{-}C_6F_4)_2PO_2]_3$, *The Journal of Physical Chemistry B*, **113** (2009) 7474-7481.

[20] Y. Peng, H. Ye, Z. Li, M. Motevalli, I. Hernandez, W. P. Gillin, P. B. Wyatt, Visible-range sensitization of Er^{3+}-based infrared emission from perfluorinated 2-acylphenoxide complexes, *The Journal of Physical Chemistry Letters*, **5** (2014) 1560-1563.

[21] G. E. Buono-Core, H. Li, B. Marciniak, Quenching of excited states by lanthanide ions and chelates in solution, *Coordination Chemistry Reviews*, **99** (1990) 55-87.

[22] G. A. Crosby, R. E. Whan, R. M. Alire, Intramolecular energy transfer in rare earth chelates. Role of the triplet state, *The Journal of Chemical Physics*, **34** (1961) 743-748.

[23] P. B. Glover, A. P. Bassett, P. Nockemann, B. M. Kariuki, R. Van Deun, Z. Pikramenou, Fully fluorinated imidodiphosphinate shells for visible-and NIR-emitting lanthanides: hitherto unexpected effects of sensitizer fluorination on lanthanide emission properties, *Chemistry-A European Journal*, **13** (2007) 6308-6320.

[24] G. Mancino, A. J. Ferguson, A. Beeby, N. J. Long, T. S. Jones, Dramatic increases in the lifetime of the Er^{3+} ion in a molecular complex using a perfluorinated imidodiphosphinate sensitizing ligand, *Journal of the American Chemical Society*, **127** (2005) 524-525.

[25] A. Aebischer, F. Gumy, J. -C. G. Bünzli, Intrinsic quantum yields and radiative lifetimes of lanthanide tris (dipicolinates), *Physical Chemistry Chemical Physics*, **11** (2009) 1346-1353.

[26] Z. Li, A. Dellali, J. Malik, M. Motevalli, R. M. Nix, T. Olukoya, Y. Peng, H. Ye, W. P. Gillin, I. Hernández, P. B. Wyatt, Luminescent zinc (II) complexes of fluorinated benzothiazol-2-yl substituted phenoxide and enolate ligands, *Inorganic Chemistry*, **52** (2013) 1379-1387.

Chapter 6: Conclusion and future work

6.1. Conclusion of the work

This thesis has mainly focused on the optical properties of lanthanide doped inorganic, hybrid and organic systems using the time-resolved spectroscopy method for making a new kind of functional material. The thesis can be divided into two main parts: the first discusses the fundamental interactions between Er^{3+} ion pairs as well as optical properties during up- and down-conversion processes, which is for the inorganic Y_2O_3 system; the second part is about investigating potential NIR functional material, including Yb^{3+}-doped $NaYF_4$ nanoparticles and co-evaporated Yb^{3+}-based organic systems.

For the inorganic system, Y_2O_3 was chosen as our starting system, due to the easy synthesis method, low phonon energy of the matrix [1] and of course the potential applications from biomedicine to solar cell. Both the up- and down- conversion processes, including lifetime and spectra, are discussed in detail regarding different Er^{3+}-doping concentrations. The Er^{3+}-doped Y_2O_3 system has been investigated already [2-4] and there were reports about the spectra difference between the UC and DC processes, and of green to red emission band ratio changes with doping concentration during the UC process, but no proper explanations have been given yet. One reason is that the spectrum itself is just a partial picture, not enough for understanding the underlying physics completely, and the other possible reason is that it is difficult to get all the dynamic data and modulate all the excited states.

Given the fact that Er^{3+} has been widely used for telecommunication amplifiers, and Y_2O_3 is easy to synthesise, Er^{3+}-doped Y_2O_3 was investigated systematically using a time-resolved spectroscopy method, which can record the population and de-population dynamic data regarding time. It was found that the long-lived $^4I_{11/2}$, $^4I_{13/2}$ states are involved in the UC process, which is responsible for the long measured lifetime of $^4S_{3/2}$ (green) and $^4F_{9/2}$ (red) emitting states during this process. Interestingly, it was further found that $^4S_{3/2}$ (green) and $^4F_{9/2}$ (red) emitting states are populated under different UC routes: $^4S_{3/2}$ (green) is relevant to the $^4I_{11/2}$ state, while $^4F_{9/2}$ (red) is relevant to the $^4I_{13/2}$ state, which explains the difference in lifetimes between the $^4S_{3/2}$ (green) and $^4F_{9/2}$ (red) emitting states. And the most important thing is that it was proved there is a UC route change from ESA to ETU with increasing the Er^{3+}-doping concentration, which explains the difference of emission spectra between UC and DC processes. Last but not least, CR processes were clearly shown for the 10% Er^{3+}-doping sample by measuring the time decay profile.

For the hybrid system, the $NaYF_4$ nanoparticle system was chosen, not only because it is one of the most investigated matrices, but also that $NaYF_4$ nanoparticle size and shape can be well controlled with a proper synthesis procedure [5]. It is known that NIR light has low scattering and absorbance inside biological tissue [6]. Together with the long lifetime of the Yb^{3+} ion (a long lifetime is useful for reducing the natural background inside the biological tissue), the Yb^{3+}-doped $NaYF_4$ NIR emitter has particular applications such as bio-labelling. We chose the 2-hydroxy-perfluoroanthraquinone chromophore capped Yb^{3+}-doped $NaYF_4$ nanoparticle

hybrid system to study, for three main reasons. Firstly, the hybrid system is a combination of the long lifetime of the Yb^{3+}-doped nanoparticle and strong sensitisation of the organic chromophore, which is very interesting. Secondly, the energy transfer between the organic chromophore and lanthanide ion encapsulated inside the nanoparticle has never been understood with population dynamics. Lastly, although the hybrid system has been demonstrated before with the chromophore absorbing during the UV region [7], there has been no red shifted chromophore demonstrated for the hybrid system NIR emitter. The advantages of the red shifted chromophore over the UV chromophore are obvious: (1) the red shifted chromophore needs a relatively low cost excitation source; (2) it favours the energy coupling between the organic ligand and Yb^{3+} ion; (3) it can penetrate deeper inside body tissue due to long wavelength. In this thesis, the red shifted chromophore sensitised Yb^{3+}-doped $NaYF_4$ nanoparticles system is demonstrated. The best sensitisation is over 300 times compared to the integrated Yb^{3+} ion's intrinsic absorption range (~970 nm) for the best sample (proper concentration and ligand to nanoparticle ratio). To the best of our knowledge, this is believed to be the highest sensitisation ever reported. In addition, using the time-resolved spectroscopy method, it was understood that there are two steps for the energy being transferred from the organic chromophore to the Yb^{3+} ions encapsulated inside the nanoparticle. The excited energy of the chromophore is firstly transferred to the Yb^{3+} ions which are near the surface of the nanoparticle and then the energy is transferred to the Yb^{3+} ions which are inside the core of nanoparticle. Interestingly, two different lifetimes were measured for the Yb^{3+} ions within two different

environments (the surface and the core of the nanoparticle), which is very important for understanding the surface quenching of the nanoparticles [8].

For the organic system, the fully fluorinated $Yb(F\text{-}TPIP)_3$ and $Zn(F\text{-}BTZ)_2$ were co-evaporated under vacuum. Fluorination reduces the oscillation energy of the chemical bonds [9], therefore, reduces the quenching of the Yb^{3+} ions. The measured longest lifetime of the Yb^{3+} ion within the organic system is over 1 ms, which is nearly 80% quantum yield. Compared with the above Y_2O_3 and $NaYF_4$ nanoparticle systems, the physical vapour deposited organic system is more suitable for the optical quality required materials. In this case, $Zn(F\text{-}BTZ)_2$ acts as a sensitiser, which has a strong absorption during the 350 nm to 550 nm region, transferring the excited energy to the corresponding states of the Yb^{3+} ion. Sensitisation during visible wavelength (350 nm to 550 nm) of the Yb^{3+} ion is characterised compared to the intrinsic excitation wavelength (900 nm to 1000 nm). Two orders of magnitude higher sensitisation has been demonstrated for the best sample, making it potentially suitable for the 980 nm waveguide amplifier. It should be noted that, concentration quenching is not obvious for the $Yb(F\text{-}TPIP)_3$ and $Zn(F\text{-}BTZ)_2$ co-doped system, therefore, it is a possibility for producing high Yb^{3+} doping concentration functional material.

6.2. Future work

Based on the fundamental study, there are a few breakthroughs of the processed functional materials (long lifetime together with high sensitisation compared with the literature reported results). However, there is more work to be done before it

can be used for real industrial applications. Firstly, the chromophore absorption range for both the organic chromophore capped nanoparticle and co-evaporated systems needs to be further red-shifted for the reasons mentioned above: lower cost excitation source, less scattering and more efficient energy coupling. This requires a new design of the chromophore. It should be mentioned, it is particularly difficult to design a new chromophore for the co-evaporated organic system, as the lanthanide-based organic compounds are usually not thermally stable [10]. Secondly, some modifications of the $Zn(F\text{-}BTZ)_2$ chromophore can be tried, as it is known that heavy atoms favour the generation of the triplets [11], which is believed to be the key factor in sensitisation. So, a heavy atom like Br and I, can be tried to replace the F in the $Zn(F\text{-}BTZ)_2$ molecule. With proper modification, these new functional materials could be used as new generation bio-labelling material or new organic amplifiers.

6.3. Reference

[1] J. Zhang, S. Wang, T. Rong, L. Chen, Upconversion luminescence in Er^{3+} doped and Yb^{3+}/Er^{3+} codoped yttria nanocrystalline powders, *Journal of the American Ceramic Society*, **87** (2004) 1072-1075.

[2] F. Vetrone, J. -C. Boyer, J. A. Capobianco, A. Speghini, M. Bettinelli, Concentration-dependent near-infrared to visible upconversion in nanocrystalline and bulk Y_2O_3: Er^{3+}, *Chemistry of Materials*, **15** (2003) 2737-2743.

[3] J. A. Capobianco, F. Vetrone, J. C. Boyer, A. Speghini, M. Bettinelli, Enhancement of red emission ($^4F_{9/2} \rightarrow {}^4I_{15/2}$) via upconversion in bulk and nanocrystalline cubic Y_2O_3: Er^{3+}, *The Journal of Physical Chemistry B*, **106** (2002) 1181-1187.

[4] J. A. Capobianco, F. Vetrone, J. C. Boyer, A. Speghini, M. Bettinelli, Visible upconversion of Er^{3+} doped nanocrystalline and bulk Lu_2O_3, *Optical Materials*, **19** (2002) 259-268.

[5] X. Ye, J. E. Collins, Y. Kang, J. Chen, D. T. N. Chen, A. G. Yodh, C. B. Murray, Morphologically controlled synthesis of colloidal upconversion nanophosphors and their shape-directed self-assembly, *Proceedings of the National Academy of Sciences of the United States of America*, **107** (2010) 22430-22435.

[6] H. He, L. Si, Y. Zhong, M. Dubey, Iodized BODIPY as a long wavelength light sensitizer for the near-infrared emission of ytterbium (III) ion, *Chemical Communications*, **48** (2012) 1886-1888.

[7] S. Li, X. Zhang, Z. Hou, Z. Cheng, P. Ma, J. Lin, Enhanced emission of ultra-small-sized LaF_3:RE^{3+} (RE = Eu, Tb) nanoparticles through 1,2,4,5-benzenetetracarboxylic acid sensitization, *Nanoscale*, **4** (2012) 5619-5626.

[8] F. Wang, J. Wang, X. Liu, Direct evidence of a surface quenching effect on size-dependent luminescence of upconversion nanoparticles, *Angewandte Chemie*, **122** (2010) 7618-7622.

[9] G. Mancino, A. J. Ferguson, A. Beeby, N. J. Long, T. S. Jones, Dramatic increases in the lifetime of the Er^{3+} ion in a molecular complex using a perfluorinated imidodiphosphinate sensitizing ligand, Journal of the American *Chemical Society*, **127** (2005) 524-525.

[10] H. Ye, Z. Li, Y. Peng, C. Wang, T. Li, Y. Zheng, A. Sapelkin, G. Adamopoulos, I. Hernández, P. B. Wyatt, W. P. Gillin, Organo-erbium systems for optical amplification at telecommunications wavelengths, *Nature Materials*, **13** (2014) 382-386.

[11] I. Hernández, Y. -X. Zheng, M. Motevalli, R. H. C. Tan, W. P. Gillin, P. B. Wyatt, Efficient sensitized emission in Yb (III) pentachlorotropolonate complexes, *Chemical Communications*, **49** (2013) 1933-1935.